Exploratory modelling of Nature-Based Island development at the Abandoned Yellow River Delta

江苏省废弃黄河口自然岛屿发展探索性模型

Jiangsu Province, China
中国江苏省

Remy van Maanen
马睿名

TU Delft

河海大學 HOHAI UNIVERSITY

Exploratory modelling of Nature-Based Island development at the Abandoned Yellow River Delta

Feasability study of Nature-Based protective measures encountering erosion at the Abandoned Yellow River Delta, Jiangsu province, China

a Nature-based solution

by

Remy van Maanen

in partial fulfilment of the requirements for the degree of

Master of Science
in Civil Engineering

at Delft University of Technology
to be defended publicly on 09 June 2020

Graduation committee:

Prof. dr. ir. S.G.J. Aarninkhof	TU Delft
Prof. dr. ir. Z.B. Wang	TU Delft / Deltares
Dr. D.S. Van Maren	TU Delft / Deltares

Other supervisors:

Prof. dr. Y.P. Chen	Hohai University
Prof. dr. Z. Gong	Hohai University
Dr. A. Chu	Hohai University
Dr. J.F. Tao	Hohai University

an electronic version is available at `http://repository.tudelft.nl/`

TU Delft

河海大學 HOHAI UNIVERSITY

Abstract

The People's Republic of China experienced large socio-economic development over the last decades, which was mainly concentrated in coastal regions. Jiangsu Province is among these regions, which shows large socio-economic differences between north and south. The Chinese Central Government has allocated Binhai County as a new coastal development zone to lessen inequality. New infrastructure (e.g. Binhai Port) was constructed and industrialisation increased in order to boost local development. Binhai County is located at the Abandoned Yellow River Delta. In 1855, the Yellow River shifted its course which cut off sediment supply to the delta. Major land retreat was stopped by the construction of sea dikes from the 1930's. Ongoing erosion is undermining the present sea defence and endangers the hinterland. The erosion along the delta has engaged the disappearance of mudflat area. Furthermore, large development in southern Jiangsu has led to constraints in usable land for which large mudflat areas were reclaimed. Multiple research pointed the negative effects of reclamation activities on ecology (e.g. decline of shorebird populations). After recognition of the importance of mudflats by the Chinese Central Government, the national policy was set to protect and restore mudflats along the Chinese coast.

The erosive features of the Abandoned Yellow River Delta (AYRD) needs counteracting measures. Within this research it is aimed to integrate a multi-purpose design in which engineering and ecology are mutually enhanced. Following the Building with Nature guidelines multiple innovative solutions can be presented. Within this research it is aimed to protect the delta by implementation of islands in front of the coast. Furthermore, it is aimed to enhance mudflat growth which adds ecological value to the delta area. It is expected that by implementation of islands a reduced energetic environment is created in which fine sediment can settle.

The Jiangsu Regional Model (JRM) by Yao (2016) was made available for this research, which is based on Delft3D software. An outcrop has been made at the area of interest which was refined (3:1) and further referred to as the Abandoned Yellow River Delta Model (AYRDM). The hydrodynamical forcing was completed by the addition of waves. The AYRDM was set-up with three sediment fractions from which one added cohesive fraction.
The production simulation was set-up for ten morphological years by using a morphological factor of 50. The better obtained understanding of the governing processes optimised island configuration design. Fifteen configurations were designed and subdivided over two series: the Basic- and Exploratory series of eight- and seven configurations respectively. The Basic series was set-up with a systematic approach in order to represent the concept of barrier islands. The Exploratory series comprehend designs based on the entrapment of sediment by using sediment transport patterns. The definition of a mudflat was set from 0.88 m to -∞ relative to mean sea level (positive depths were considered) in order to measure mudflat growth.

The findings within the reference production simulation (without the implementation of islands) showed a flood dominant environment in which flood direction is south. Hence, south- and offshore directed residual sediment transport were observed along the AYRD. The outgoing sediment flux from the AYRDM increased by $2.2{\cdot}10^7$ ton/year when waves were included. The addition of waves increased the average grain size by 26 μm at siltation areas due to sediment stirring and cross-shore transport. The effect of island configurations showed most favourable sediment entrapment when elongated islands and small inlet widths were applied. The shallows induce larger friction on tidal movement for which current velocities and herewith sediment

transport capacity is reduced over distance. Hence, depositional areas were found to be radially deflected to the south. Secondary flow, due to eddy formation, showed significant streaming induced sediment transport behind the islands ends. Small bed slopes induce larger distances between islands and mainland China, which holds for relatively larger mudflat areas. Wave penetration was reduced significantly when islands were implemented, which created a less energetic environment. The largest increase of mudflat relative to the reference simulation is 59.8 km^2 after ten morphological years by implementing 16 km^2 of island area.
The findings within this study are representative for the Abandoned Yellow River Delta area and show the potential of islands in order to protect the delta and create additional ecological/recreational benefits alongside.

Acknowledgements

'Nanjing is home to about half of the Dutch population!'. It was the first thought when looking into Nanjing, the city where I was invited by Hohai University to partially execute my thesis. I had the unique opportunity to experience Chinese culture in an extraordinary position as exchange student. During my four month stay, I got acquainted with the beauty of China and its fast lifestyle based on smartphone technology. Unfortunately, time passed quickly and as soon as I knew, I had to adjust to 'normal' Dutch life again. I am sincerely grateful for the given experience in China, which I will never forget.

As of first, I would like to thank my supervisors from Delft University of Technology. Prof. dr. ir. Stefan Aarninkhof for his help in setting up my stay at Hohai University and his continuous support throughout the project. I would like to thank Prof. dr. ir. Zheng Bing Wang for his valued help and comments during the thesis. Last, I would like to thank Dr. Bas van Maren for his support during modelling difficulties and valuable feedback.

Then, I would like to thank my Chinese supervisors for the incredible stay at Hohai University. First, I would like to thank Prof. dr. Yong Ping Chen for his generous hospitality, valuable help and feedback during my stay. I would like to thank Prof. dr. Zheng Gong for the insightful discussions up on my research. I want to thank Dr. Ao Chu for his time during troubleshooting and the general discussions. Finally, I want to thank Dr. Jian Feng Tao for his aid and feedback.

After four months, Hohai University became my second home. I want to thank all coworkers for them making me feel at home and looking after my well being. Ding Hongwei, thank you for setting me up with all practicalities and smartphone applications to experience the Chinese lifestyle to its fullest. Special thanks to Alisher Khazratov, Timothee Kouonang, Jinshan Pu, Shaoxu Zheng, Zhou Tingzhang, Xindi Chen, Kaifeng Xiong, Amber Merina, Rohan Eccles and Richard Rees for all gym sessions and other sport activities, lunch and dinners, nightlife and small trips spent together.

I would like to thank my friends for the necessary distraction. In particular, I would like to thank Tim van Dam for his support during programming troubleshooting and the gym- and study sessions together. Further, I would like to thank Jaap Janssen for his attendance in many kitesurfing sessions during both our graduation.

Finally, I want to thank my family for their continuous support and distraction making this all possible.

Remy van Maanen
Delft, June 2020

Contents

List of Figures

List of Tables

Abbreviations

AYRD Abandoned Yellow River Delta. viii, 2, 5, 8–14, 17, 20–27, 34, 38, 42–44, 47, 50, 53, 57, 61, 62, 67, 68, 92, 94, 97, 103, 107, 114, 119

AYRDM Abandoned Yellow River Delta Model. vii, ix, 18–23, 25–27, 41, 67, 70, 89, 92, 96, 98, 100

BC Bohai Current. 11

BRI Belt and Road Initiative. 1

BS Bohai Sea. 19, 21

CYS Central Yellow Sea. 11

DD Domain-Decomposition. 19, 21

EAAF East Asian-Australasian Flyway. 15

ECS East China Sea. 9, 11, 19, 21

GDP Gross Domestic Product. 1

HB Haizhou Bay. 7, 10, 13

JRM Jiangsu Regional Model. vii, ix, 18–23, 25–27, 62, 70, 81, 87, 89, 92, 94, 96, 97, 100, 101

ME Nash Sutcliffe Model Efficiency. 27, 28, 36

MHW Mean High Water. 38

MLW Mean Low Water. 38, 48, 65

MORFAC Morphological Acceleration Factor. 23, 41

MZCC Min-Zhe Coastal Current. 11

NAYRD Northern Abandoned Yellow River Delta. 14, 21, 29, 34, 38, 41–44, 48–50, 53, 54, 57, 58, 68, 114, 119

NRSRF Northern Radial Sand Ridge Field. 7, 8, 13

NYS Northern Yellow Sea. 9

PB Percentage Bias. 27, 28

RSRF Radial Sand Ridge Field. vii, 7–10, 12, 13, 22–24, 38

SAYRD Southern Abandoned Yellow River Delta. 14, 38, 41–44, 48–50, 53, 54, 57, 58, 67, 68, 114, 119

SRSRF Southern Radial Sand Ridge Field. 8, 11–13

SSC Suspended Sediment Concentration. 10, 14, 22, 25–27, 31, 33, 36, 43, 92, 94–97, 100, 101, 103, 104, 107

SYS Southern Yellow Sea. 1, 4, 7, 9–12, 23

TS Taiwan Strait. 11

TWC Taiwan Warm Current. 11

WSYS Western South Yellow Sea. 14

YRE Yangtze River Estuary. 11, 19

YS Yellow Sea. 11, 19, 21

YSCC Yellow Sea Coastal Current. 11, 14

Nomenclature

ϕ	Krumbein phi scale	-
τ_{cs}	Critical bed shear stress for sedimentation	N/m^2
τ_{ce}	Critical bed shear stress for erosion	N/m^2
τ_c	Current induced bed shear stress	N/m^2
τ_{cw}	Wave - current induced bed shear stress	N/m^2
ρ_s	Specific density	kg/m^3
$\rho_{s,dry}$	Dry bed density	kg/m^3
$A_{mudflat}$	Total mudflat area	km^2
A_{island}	Total island area	km^2
C_0	Initial concentration	mg/l
C_b	Bed friction coefficient	m^2/s^3
D	Particle diameter	μm
D_0	Reference diameter	μm
d_0	Initial bed layer thickness	m
dir	Wave direction	$^\circ$
H_s	Significant wave height	m
n	Manning roughness coefficient	$s/m^{1/3}$
M	Erosion parameter	$kg/m^2/s$
MI	Mudflat-Island ratio	-
m	Measurement	-
$\bar{m}$	Mean value of measurements	-
Δm	Measurement error	-
ME	Nash-Sutcliffe Model efficiency	-
PB	Percentage Bias	-
P	Tidal prism	m
p	Model predictions	-
T_p	Peak wave period	s
W_s	Settling velocity	m/s

1 Introduction

1.1 Background

The People's Republic of China is a vast country in East Asia. It provides home to 1.4 billion people and is currently the most populated country in the world. Introduction of the Chinese Economic Reform programme in 1978 has led to major economic development. In 2018, China's economy had a net growth of 6.6% and reached world's second largest Gross Domestic Product (GDP) of 13,600,000 million USD (World Bank, 2019). The most economic development is concentrated within the coastal regions. Covering 13% of China's landmass and accommodating 40% of the total population; the coastal regions generate 10% of China's total GDP (Meng et al., 2017; Wang and Wall, 2010; National Bureau of Statistics, 2018; To and Lee, 2018).

Among these coastal regions is Jiangsu Province. It is the second most developed Province in China due to the early opening up and favourable geographical location (National Bureau of Statistics, 2018; Meng et al., 2017). Jiangsu is situated at the Southern Yellow Sea (SYS) and is enclosed by Shandong Province to the north and Yangtze estuary to the south. It covers about 1.1% of the total main land and is characterised by flat terrain and a dense network of waterways (Du et al., 2019). The Jiangsu coastline stretches over 954 km comprising three geographical features from which 137 km is stable, 571 km accretive and 246 km erosive (Bao et al., 2019b). Approximately 90% of its coast is characterised by mud, where large intertidal mudflats can extend up to tens of kilometres into the SYS (Wang et al., 2012b; Xu et al., 2016; Zhu et al., 1998).

Jiangsu Province has a rich history in sea-salt production which required extensive mudflat area. Late 19th century, salt production was associated with a low production efficiency of arable land. Followed by a shift in land-use from extensive to intensive industry, the salt production was relocated to Northern Jiangsu (Bao, 2016; Bao et al., 2019b).
The marine economy has developed rapidly after introduction of the reform policy. Due to the large demand for new land, it became a constraint in its own development (Meng et al., 2017). In coastal regions reclamations are an effective method to provide in this demand. Since the 1950's, mudflat reclamations have been carried out along the Chinese coastline at high pace. As a result, the total mudflat area has declined by over 50% mainly concentrated in Zhejiang, Jiangsu and Liaoning Provinces (Meng et al., 2017). Reclaimed areas are mainly used for aquaculture, agriculture, salt extraction, forestation, port (expansion), (coastal) industry and tourism (Wang et al., 2014).

Sustained economical growth is pursued with new initiatives as the Belt and Road Initiative (BRI). Along with the imposed development, an increased demand in land is expected together

with an increased port capacity (World Bank, 2018; To and Lee, 2018; Wang and Wall, 2010; Zhai, F., 2018). Jiangsu is host to several coastal- and riverine ports, which are dotted along the coastline at Lianyungang, Guanhe, Binhai, Sheyang, Dafeng, Yangkou and Lusi. As part of the national strategic policy to increase port cooperation, all main national- and important regional ports cooperate as the Jiangsu Port Group Co., Ltd. (Wang and Wall, 2010; Du et al., 2019; Huo et al., 2018; Xinhua Finance Agency, 2017). Port development however is difficult to accomplish due to the shallow coast (Zhu et al., 1998). The coastal zone of Jiangsu has been promoted by the Chinese Central Government to be part of the national development strategy. Large mudflat areas are designated herein to be reclaimed before 2020 for e.g. port expansion (Zhang and Chen, 2011; Du et al., 2019; Meng et al., 2017).

Evident spatial socio-economic differences occur in Jiangsu Province, where the relatively poorer and less 'open' north (Subei) is lagging behind on the south (Sunan) (Wei and Fan, 2000; Bao et al., 2019b,a; Huang et al., 2015; Meng et al., 2018) Since the reformation, interregional inequality developed strongly due to State Policy, local agents, foreign investment and proximity to Shanghai. Sunan attracted foreign investments to their designated open zones with attractive policy environments and good infrastructure. Subei is in a relatively disadvantage position through its location, local government and available resources by which foreign investment averted (Wei and Fan, 2000). The north has an immense salt production capacity in which Subei's potential, the marine chemical industry, can boost the local marine economy (Wang and Wall, 2010).

Binhai county, a subdivision of Subei, was allocated as a provincial development zone to lessen socio-economic inequality (figure 1.1). New infrastructural projects have been executed to increase accessibility with Shanghai and the Bohai Economic Rim. A new Coastal Industrial Park has been set-up in 2002, which is expected to expand from 20 km^2 to 50 km^2. Additionally, a new port has been built at the tip of the AYRD (Binhai Port). It consists of two 100.000 ton docks and serves currently as a chemical hub. Binhai Port is allocated as a favourite deep water port, due to its erosive coastline and natural deep waters (Binhai China Merchants Oganisation, 2013). It is expected that the implementation of improved infrastructure, industry development and increased tourist facilities will boost local economy (Zhu et al., 1998; Wang and Wall, 2010).

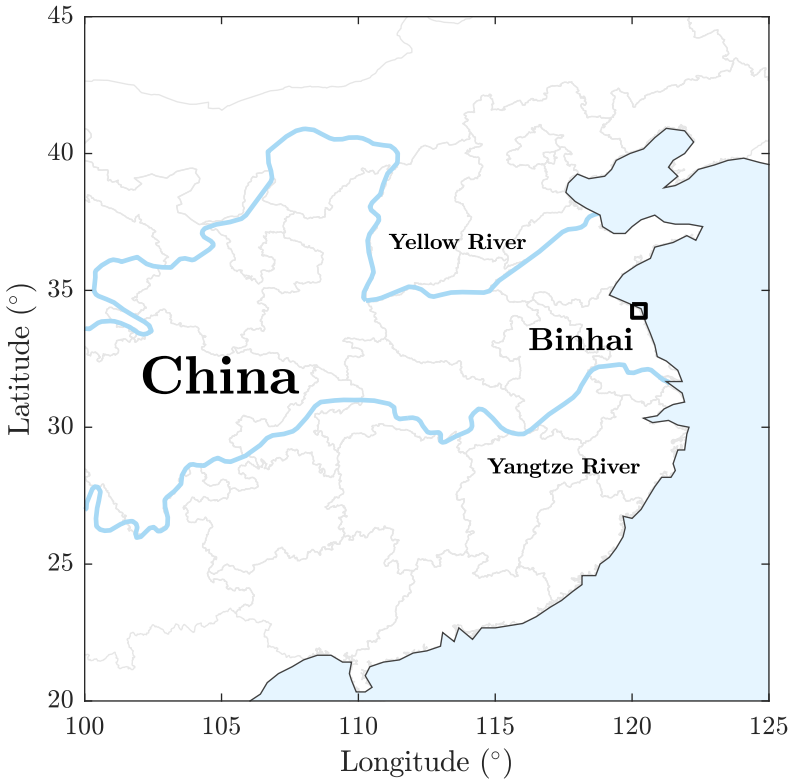

Figure 1.1: Jiangsu Province, Binhai county. New Coastal Development Zone along the Jiangsu coast

1.2 Problem statement

Jiangsu Province has an extensive history in large-scale land reclamation which is driven by socio-economic factors. The natural environment is disturbed by the disappearance of mudflats, since these provide in different ecosystem services contributing in different benefits like nutrient cycling and pollutant purification. Through wave attenuation and sediment accretion, mudflats offer natural protection against coastal erosion and floods. In addition, they provide for natural habitat and sustained biodiversity. As a consequence, mudflats provide in local livelihood, recreational- and other economical benefits (Cui et al., 2016; Li et al., 2018; Cui et al., 2016; Gu et al., 2018; Pritchard and Hogg, 2003).

In general, disturbance of local hydrodynamics will cause changes in morphological development. Muddy environments, such as the Jiangsu coastline, are profoundly complex in sediment dynamics and will react strongly to relatively small changing hydrodynamics (Janssen-Stelder, 2000; Roberts et al., 2000; Shi et al., 2017; Shi and Chen, 1996).
Recent research has shown that these large-scale reclamations have significant effect on local tidal dynamics and local wave conditions (Qingguang et al., 2016; Cong et al., 2017; Tao et al., 2011; Song et al., 2013; Zhu et al., 2016; Wang et al., 2008). It can be concluded that the anthropocentric activity affects the morphological driving forces and thus the overall coastal evolution. As a result, flood risk will be increased to local extend due to the changes in tidal dynamics (Cong et al., 2017; Song et al., 2013; Qingguang et al., 2016).

Additionally, large concerns have been raised regarding pollution and biodiversity. The mudflats

are an important staging site in the East Asian-Australasian Fly way. Over 36 migratory shorebird species, from which several are endangered, use these mudflats as their stop-over site during migration. The decline of mudflat area is directly linked to a loss in habitat area and hence a decline in shorebird population (Piersma et al., 2017; Barter, M.A., 2002; Studds et al., 2017).

The Chinese State Council acknowledges the importance of the mudflats along its coast. Emphasis is given to ecological development, restoration and protection (Bao et al., 2019a; Xinhua, 2018; Xinhua, 2018; BirdLife International, 2018). A better understanding of the present coastline is needed in order to asses the impact of future reclamations. Therefore, all planned business-orientated reclamation activity has been put on halt and local governmental authority repealed. New reclamations are allowed when serving in key infrastructure, national defence or public welfare (Bao et al., 2019a; Melville, 2018; BirdLife International, 2018; China Daily, 2018).

Socio-economic activity has increased in Binhai County after it was allocated as a provincial development zone. Binhai is located at the AYRD where the Yellow River emerged during 1128 - 1855. In 1855, the Yellow River shifted its course by which sediment supply was cut off. The AYRD has suffered from erosion since, which resulted in a land loss of 1400 km^2 (Zhang et al., 2015; Xingjian, 2011). The progradation of the delta has been intensively followed by human activity. Large areas have been reclaimed which serve mainly in rural uses (e.g. salt production, aquaculture). To prevent the coastline from further retreat, sea dikes have been built since the 1930's. Most of the coastline is protected due to these interventions and landward retreat has significantly been reduced. As a result, intensified shoreface erosion led to steep bed slopes and a decrease in mudflat area (Zhou et al., 2014; Zhang et al., 2002; Yu et al., 2002). Today, continuing erosion has partly undermined sea defence structures causing structural instability and hence endangering the hinterland. Additionally, storm events damage the dikes and lead to annual repairs (Du et al., 2019; Su et al., 2017b; Yu et al., 1994; Zhou et al., 2014).

These conventional coastal engineering projects have been argued for their unsustainable character. In recent years, an innovative approach called Building with Nature has been implemented successfully in several projects worldwide. By understanding the natural system and making use of local ecosystem services, an integrated design is endeavoured where socio-economic and ecological aspects are mutually enhanced (de Vriend et al., 2014, 2015). Flood protection is more sustainable and cost-effective when safeguarded by ecosystem creation and restoration (Temmerman et al., 2013). The solutions coming forth from this approach are considered Nature-Based.

1.3 Objective

The erosive trend at the AYRD shows the need for an integrated coastal development design in which both socio-economic and ecological aspects are concerned. Innovative measures are desirable which reinforce the natural system, increase recreational area and enhance socio-economic development along the AYRD. By applying the Building with Nature approach multiple options are conceivable. One of these is the implementation of islands at the AYRD, which offer coastal protection and induce a less energetic area behind. Subsequently, increased siltation rates are expected which will enhance mudflat development. On its turn, mudflats will add to socio-economic benefits (e.g. fisheries, eco-tourism).

Hence, the following objective is formulated:

The main objective of this research is to design an island configuration at the Abandoned Yellow River Delta, by optimising morphological/ecological and socio-economic benefits.

The main objective is divided into two sub-objectives, which are formulated here below:

- The first sub-objective is to better understand the governing hydrodynamic and morphological processes of the Jiangsu coast and in particular the Abandoned Yellow River Delta. This will be done with the help of numerical modelling.
- The second sub-objective is to optimize in island design configuration. The objective is realised by adopting the Building with Nature approach.

1.4 Research questions

In order to asses the objective, the following research question has been formulated:

> Could large-scale Islands enhance coastal protection and encourage the development of large-scale tidal mudflats along the Abandoned Yellow River Delta?

Several sub-questions have been set in order to help answer the main research question. The sub-question are presented below:

- What are the governing processes for flow and sediment transport at the Abandoned Yellow River Delta?
- What is the impact of large-scale islands on the hydrodynamic- and morphological processes?
- What configuration of islands is favourable?

1.5 Thesis outline

An extensive literature review has been done in order to obtain a good understanding of the future design area: the Abandoned Yellow River Delta. Chapter 2 will introduce the general outline of the Jiangsu coast and its hydrodynamical- and morphological processes. Furthermore, these aspects will be given detailed attention for the Abandoned Yellow River Delta region. Socio-economic aspects define the closure of Chapter 2. Chapter 3 treats the method used within this research. The Jiangsu Regional Model has been made available for this research. It encompasses the entire Jiangsu coast and is enclosed by the Shandong Peninsula and Yangtze River estuary. The model is well calibrated by (Yao, 2016). More details on the Jiangsu Regional Model and further model development are elaborated herein. Chapter 4 treats the calibration- and production results. The calibration simulations are set for a four consecutive spring-neap tidal cycle, as the production run is set for a morphological time of ten year. The production simulations are a first to wave simulations. Hence, results are shown for wave-current and current-only conditions in order to see the effect of waves. Chapter 5 treats the island configuration designs. Hence, the design process and model results are elaborated herein.
The discussion can be found in Chapter 6, followed by the conclusions presented in Chapter 7.

2 System description

2.1 Topography

The large coastal plain of Jiangsu was until 1855 fed by two major rivers, the Yellow- and Yangtze River. Huge sediment loads carried by both rivers have prograded the coastline 20 - 40 km seaward since the 12th century. The northern plain is formed by the Yellow River, whereas the central and southern plain by the Yangtze River (Zhu et al., 1998; Wang and Ke, 1997).
The SYS is a low-gradient and relatively shallow sea with in particular the western inner shelf along the Jiangsu coast (Wang et al., 1986; Zhou et al., 2014; Larsen et al., 1985). The abundant river sediment supply has characterised the shores of Jiangsu as a muddy coastline. Large intertidal mudflat exist which can reach out several kilometres into the SYS (Wang and Wall, 2010; Wang et al., 2012b). In general, the Jiangsu coastline consists of roughly three geographical features e.g. the south situated Radial Sand Ridge Field (RSRF) and both Haizhou Bay (HB) and the Abandoned Yellow River Delta (AYRD) situated in the north. These features are the result of interaction between two tidal systems governing in the SYS for over 7000 years BP (Yao et al., 2013; Zhu and Chen, 2005). An overview of the Jiangsu coast can be found in Figure 2.1.

Haizhou Bay is situated at the most northern part of Jiangsu. The coastline is characterised by sand, although grades into silt further south. The bay holds shallow water (up to 10 m in depth) and the presence of a small Island shadows the coast from waves. HB is a depositional and stable stretch of coast, which can be seen in Figure 2.1 (Zhu et al., 1998).

The Abandoned Yellow River Delta has been abandoned since 1855 when the Yellow River shifted its course to the Bohai Sea. Between 1128 - 1855 the Old Yellow River deposited abundant amount of sediment into the Yellow Sea from which a huge delta originated. In absence of river sediment supply the delta has been eroding since 1855. The current shape of the delta is mainly the result of tidal influence which determined the overall evolution. Sea defences are relatively important in maintaining the sub-aerial delta. Waves are less significant, however induce remarkable erosion on offshore shoals (Su et al., 2017b). The study area can be seen in Figure 2.1, which is denoted by the yellow outline. The transition from an erosional to stable and depositional coastline is at the southern study area boundary.

The Radial Sand Ridge Field is an unique geographical feature situated at southern central Jiangsu. It consists of 70 fan shaped sand ridges which are radiating 30 - 100 km into the SYS. A total area of 22,740 km^2 is comprised in which sand bodies can have lengths and widths of several tens of kilometres. The channels in between are ranging from 0 - 30 m in depth and can reach up to 50 m (Yao et al., 2013; Wang et al., 2012b).

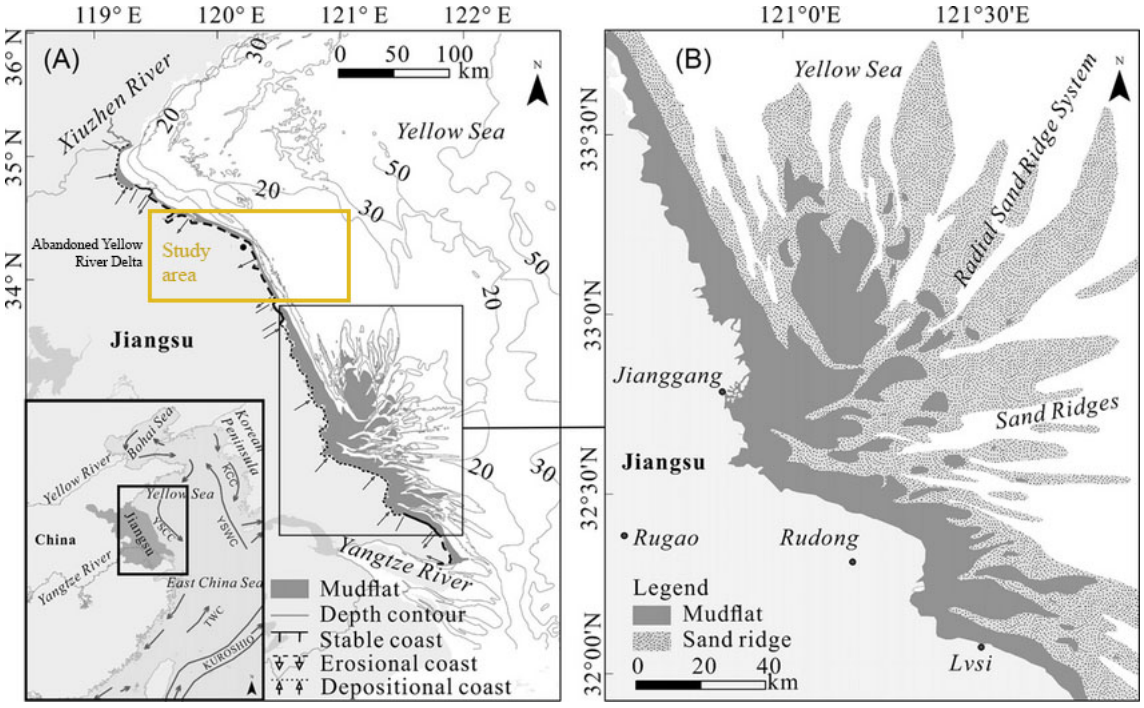

Figure 2.1: Overview of the Jiangsu coast. Sub-figure A depicts the overall coastal current pattern within the Yellow- and Bohai Sea. The Abandoned Yellow River Delta and the Radial Sand Ridge Field (RSRF) are shown and erosive-/accretive trends are illustrated. The yellow enclosed represents the study area within this research. Sub-figure B shows a detailed illustration of the RSRF, in which the mudflats are displayed (from Du et al., 2019)

Three main sand ridges (Dongsha, Tiaozini and Gaoni) are situated at the center of the RSRF which emerge at low tide. These ridges separate the RSRF into two geomorphological units between definite morphological differences exist, i.e. the Northern Radial Sand Ridge Field (NRSRF) and Southern Radial Sand Ridge Field (SRSRF) respectively. These difference are found in sediment sorting, tidal forcing and tidal flat topography. The northern ridges are elongated, straight and have the tendency to bend northward. Oppositely, the southern ridges are short and discontinuous. Differences are to be seen due to distinctive tidal characteristics (Wang and Ke, 1997; Xing et al., 2012; Xu et al., 2016). Much research has been done to the formation and provenance of the Radial Sand Ridge Field. Wang and Ke (1997) and Zhu et al. (1998) hypothesized that the sand ridges have mainly been supplied by older AYRD sediments and were reworked under the present hydrodynamic processes. From initial perspective Li et al. (2001) suggests that sediments were delivered mainly by the Yangtze River and later from the Yellow River. Sea bed erosion contributes slight. Wang et al. (2012b) points that the formation of the RSRF finds it origin in late Pleistocene. The Paleo-Yangtze River Estuary could be found near the apex of the RSRF. Large amounts of river sediment were deposited which were reworked by the tidal system into large sand ridges. The Yellow River affected the system during late Holocene. Mineralogical research by Li et al. (2001) has shown that the sediment source of the sub-aerial RSRF came initially from the Paleo-Yangtze River and later predominantly from the Yellow River The large offshore sand ridges induce a sheltering effect due to e.g. wave attenuation. Hence, a less energetic environment is created for which fines are able to settle. The large intertidal mudflats at the AYRD originate from this principle. Due to the shape of the ridges, the extensive mudflats are mainly seen at the NRSRF.

The RSRF originates from an unique tidal wave system which in turn controls the depositional processes and maintenance of the ridge pattern. The AYRD has a significant role in sediment supply to the RSRF. The erosion of the AYRD shifts the tidal system south, through which an overall southward migration of the RSRF has been initiated (Chen et al., 2017). Other sediment fluxes affecting the RSRF are sediment load from the Yangtze River and seabed erosion (Zhu and Chen, 2005; Tao et al., 2019; Wang et al., 2012b; Wang and Ke, 1997; Xu et al., 2016).

2.2 Hydrodynamics

2.2.1 Tide

The tidal wave system of the Yellow Sea is dominated by a semi-diurnal tide in which the M2 constituent is pre-dominant (Su et al., 2015; Yao et al., 2018). The AYRD can be divided in two regions, the Northern Yellow Sea (NYS) and Southern Yellow Sea (SYS) respectively, where two separate amphidromic points can be distinguished. These rotating tidal waves, also known as Kelvin waves, are both directed anti-clockwise. The rotary wave in the SYS travels south along the coastline and converges with a progressive wave entering from the East China Sea (ECS) at the central coast (i.e. Jianggang). Here, a radial current field exist which is fundamental for the formation and presence of the RSRF. An overview of the governing tidal wave system can be seen in figure 2.2 (Du et al., 2019; Larsen et al., 1985; Yao et al., 2013; Su et al., 2013; Xu et al., 2016; Zhang et al., 1999; Xing et al., 2012).

The Abandoned Yellow River Delta is characterised by a semi-diurnal tide which is predominantly found along the Jiangsu coast (Du et al., 2019; Liu, 2011; Yao et al., 2018). The tidal range differs significantly over the AYRD. The southern AYRD has a tidal range of 1.6 m which gradually increases to 1.8 m at the tip of the delta. Hereafter, the tidal range increases in the northern AYRD to 2.7 m (Liu, 2011). Generally the tidal range differs along Jiangsu due to its unique morphological features and tidal system. In HB the tide ranges between 3 - 4 m (Zhu et al., 1998; Zhang, 1992), while in the RSRF the tidal range increases extremely due to the converging tidal waves. Local maximum values can exceed 9 m, yet an average tidal range of 6 - 7 m is observed. (Yao, 2016; Zhu et al., 1998; Liu et al., 2013; Wang and Ke, 1997; Xing et al., 2012; Xu et al., 2016). The RSRF is characterized by a semi-diurnal tide in which the horizontal- and vertical tide have a 90° phase difference (Xu et al., 2016; Wang and Ke, 1997; Du et al., 2019).

The distinctive tidal system of the SYS induces an exclusive current pattern, which is in particular strongly influenced by the rapid changes in bathymetry at the RSRF (Xing et al., 2012). Just of the AYRD the rotary tidal wave circulates around its amphidromic point. The tidal current runs parallel along the AYRD and dominates at both sides. The mean current velocity ranges between 0.6 - 1.0 m/s and strengthens from north to south (Zhou et al., 2014; Zhang et al., 2002, 2015; Yao et al., 2018). Due to the shallow SYS the tidal wave deforms leading to an increased tidal range and asymmetrical tide. The asymmetric tide induces a shorter flood-tidal phase leading to higher flood current velocities in comparison with the ebb phase. Flood tide is directed south-west and ebb tide is north to north-east (Zhang et al., 2014). Northward currents are less strong compared to the ones south-west (Ren, 1986; Zhang et al., 2002). Flood dominance has effect on the residual sediment transport, which is southward directed (Zhang, 1992; Xing et al., 2012).

In HB the mean current velocities are weak and range between 0.3 - 0.5 m/s. Within the RSRF tidal currents can exceed 1.5 - 2.5 m/s due to its unique morphology (Liu et al., 2013; Xu et al.,

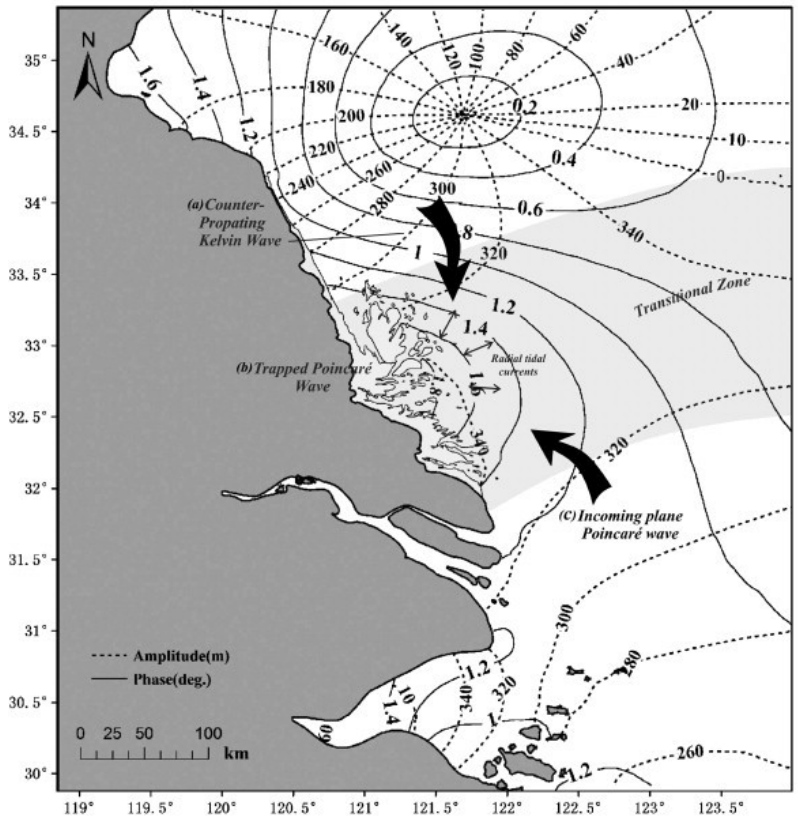

Figure 2.2: The tidal system within the South Yellow Sea (from Xing et al., 2012)

2016; Zhou et al., 2014).

2.2.2 Waves

Wind exerts friction on the water surface from which wind-driven currents can originate. The effect of wind on small scale is seen by wave formation. Hereby are the duration, fetch and wind force important parameters determining the wave height and its energy. Strong waves affect the Suspended Sediment Concentration (SSC) due to their high exertion capacity of bringing bed material into suspension (Yao et al., 2018). The effect of waves are localised and seasonal varying. Waves are considered of secondary importance, however play a relatively important role in the erosion of the AYRD (Su et al., 2017a). The deep shoreface is in favour of wave energy conservation and with no sheltering effects due to offshore sand ridges, waves can easily increase local SSC rates (Xing et al., 2012; Yao et al., 2018).

The AYRD is influenced by winds mainly controlled by the monsoon climate, varying both spatially and temporally. The wave direction is closely related to the monsoon (Zhang et al., 2015). Available wave data shows wave from multiple directions different than of the governing monsoon winds, indicating the large effect of local wind set-up. The monsoon climate induces mild summer winds prevailing from the south-east with average wind speeds ranging between 3 - 6 m/s. Small waves are induced on consistent frequency from pre-dominantly south-east direction. Significant wave heights are generally ranging between 0.5 - 1.0 m with a total frequency $> 50\%$. In winter strong winds are prevailing from the north, north-east in which average wind speeds

reach 6 - 10 m/s. Waves from the north-east are dominant and average wave heights can reach up to 2.9 m with a total frequency of 39% - 47%. The wind in the winter are statistically seen stronger than the summer winds (Ren, 1986; He et al., 2010; Liu et al., 2013; Zhou et al., 2014; Zhang et al., 2014, 2015; Lu et al., 2015; Xu et al., 2016; Zhu et al., 2017; Yao et al., 2018).

Aside its relatively calm sea state, the SYS is occasionally hit by strong seasonal storms and infrequent calamitous typhoons. These induce large waves with maximum wave heights exceeding 4.0 - 5.0 m (Liu et al., 2013; Zhou et al., 2014). These waves inundates large areas of the coast and have high capacity in reworking large quantities of sediment.

2.2.3 River discharge

The Jiangsu coast was fed by two major rivers, the Yellow- and Yangtze River. The Yellow River shifted its course to the Bohai Sea in 1855. The old delta was left abandoned and presently acts as a sediment source to the Jiangsu coast. Today, the abundant sediment supply of the modern Yellow River progrades a new delta in the Bohai Sea (Chu et al., 2006).

The Yangtze River is the largest river in China regarding water discharge. Its sediment load is considered low in comparison with the Yellow River. The Yangtze River Estuary (YRE) acts as a sink due to the low river run-off and tidal range. Most sediment however is subtracted from the estuary and transported south into the Taiwan Strait (TS) and eastward into the ECS (Lee and Chough, 1989). Roughly 10% of the total discharge flows northward mainly during the summer period. The flow dilutes salinity in the adjacent estuary region. Herewith, small amounts of sediment are transported to the SRSRF (Su et al., 2015; Yuan et al., 2016; Yao et al., 2018; Du et al., 2019; Wu et al., 2013, 2014). The established Three Gorges Dam (2003) decreased sediment load significantly (Dai et al., 2014).

The vast plain of Jiangsu is cut across by small rivers and numerous canals. These man-made channels distribute fresh water from the Yangtze River. Intersected by transverse canals which redistribute the water over a large plane northward. These small rivers eventually emerge into the SYS, however cause negligible effect on the flow regime. The sediment load carried by the small rivers is negligible due to the numerous dams built upstream (Zhu et al., 1998; Yao et al., 2018; Du et al., 2019; Lu et al., 2015).

2.2.4 Large-scale currents

Aside tidal- several large-scale currents can be found within the Yellow Sea (YS). Along the AYRD the Yellow Sea Coastal Current (YSCC) advects resuspended sediment in east- and south direction (Lee and Chough, 1989; Liu et al., 2013). However, recent research points that seasonal influence affects the current direction. The YSCC flows northward in summer and south in winter (Lu et al., 2015; Yuan et al., 2017).

The Bohai Current (BC) carries suspended sediment from the modern Yellow River southward. These turbid plumes have summer concentrations of 5 mg/l. The current bypasses the Shandong Peninsula and deposits significant amount of fine sediment in the Central Yellow Sea (CYS) (Lee and Chough, 1989; Ren, 1986; Zhang et al., 2014).

The Min-Zhe Coastal Current (MZCC) starts of from the Yangtze River Estuary (YRE) and flows southward during winter. Large amounts of sediments are transported on the inner shelf and are kept from being transported into the deep ocean by the north flowing Taiwan Warm Current (TWC). Measurements have indicated a low salinity surface plume in north-east direc-

tion. According to the measurements, small amounts of suspended sediment were transported along with. Hence, it was shown that the MZCC has slight influence on siltation processes in the SRSRF (Liu et al., 2007; Wu et al., 2013, 2014; Yao et al., 2018; Lee and Chough, 1989).

2.3 Sediment Characteristics

2.3.1 Morphology

Overall, three distinct geographical features are present at the Jiangsu coastline; Haizhou Bay, the Abandoned Yellow River Delta and the Radial Sand Ridge Field. These are the result of the governing hydrodynamical system. The tide is the dominant forcing. Waves are considered important in stirring up sediment at near- and offshore shoals (Su et al., 2017a).

The Yellow River emerged into the SYS between 1128 - 1855 through which a delta prograded. It carried abundant amount of sediment, mainly silt and clay, which turned the sandy beaches of Jiangsu into a muddy coast. The Yellow River shifted its coarse in 1855 to the Bohai Sea as a result of flooding (Zhou et al., 2014). The sediment supply was cut off and meanwhile the delta started to erode as strong tidal currents and waves reworked the sediment (Zhang et al., 2002). The AYRD has undergone continuous erosion ever since, however a gradually declining erosion rate has been noticed. Fine sediments of the AYRD are mainly transported south and offshore, nourishing the tidal flats along the Jiangsu coast. The AYRD is an important sediment source for the RSRF. The transition from an erosional to stable and depositional coast is near Sheyang River Estuary. In Figure 2.1 it is pointed by the southern study area boundary.
However, fine sediment is also transported northward of the AYRD. Wang (1980) pointed that the Guanhe River mouth has been formed by north-east flowing currents Zhang et al. (2002); Yao et al. (2018); Zhang et al. (2014, 2015). The northern Jiangsu coast is an erosive coast in general, whereas the southern is accretive (Zhou et al., 2014; Su et al., 2017b; Gao, 2009; Yao et al., 2018; Zhu et al., 1998; Liu et al., 2013). The profile of the erosive coastline is concave upwards (Wang and Ke, 1997), where the accretive mudflats in abundant sediment supply can prograde seaward maintaining an equilibrium convex-up profile Liu et al. (2011).

The coast of Haizhou Bay is the only stretch along Jiangsu where sandy beaches can be found. Here, small rivers emerge which supply sediment. Due to upstream damming (i.e. Xiaotashan reservoir) and construction of tidal barriers sediment supply is cut off to the coast. Another reason why the coast is erosive can be found in anthropogenic activity (i.e. sand extraction) (Zhang et al., 2002).

The Radial Sand Ridge Field is an accretive system in which the tidal forcing is dominant. The protective offshore ridges ensures a calm environment where fines can settle. The converging point of the tidal system is an important feature for the existence of the RSRF. As a result of continuous erosion at the AYRD, the rotary tidal wave smooths in the north leading to a southward shift of the converging point between the incoming progressive- and rotary tidal wave. This forces shoals and tidal channels to migrate south, withholding the RSRF migrating south (Chen et al., 2009, 2016).

The Yangtze River Estuary has become erosive due to the sediment blockage by upstream damming in 2003 (i.e. Three Gorges Dam) (Luan et al., 2018).

2.3.2 Bed composition

The bed composition along the Jiangsu coast is spatially distributed. The most commonly found types are silt, sandy silt, sand and clayey silt from which silt is the most dominating type (Table 2.1). Sediments are distributed in zones parallel to the shoreline and grain size differs in cross-shore direction from fine to coarse (Wang and Ke, 1997).

Haizhou Bay (HB) differs spatially. The north of HB is mainly composed of fine sand. While head more south, clay patches are found within the estuary and fine sand is found more offshore.

The most dominant type of sediment found at the Abandoned Yellow River Delta are silt, clayey silt and very fine sand (Lu and Chen, 2011; Yao et al., 2018). The cross-shore profile at the AYRD has a different trend compared to the rest of Jiangsu. The sediment is coarse nearshore and becomes finer seaward. Coarse sediment, such as silty sand, is found at the river mouth (Xingjian, 2011; Lu and Chen, 2011). The characteristics of sediment distribution are found in a close relationship with the governing hydrodynamics (Zhang et al., 2014, 2015).

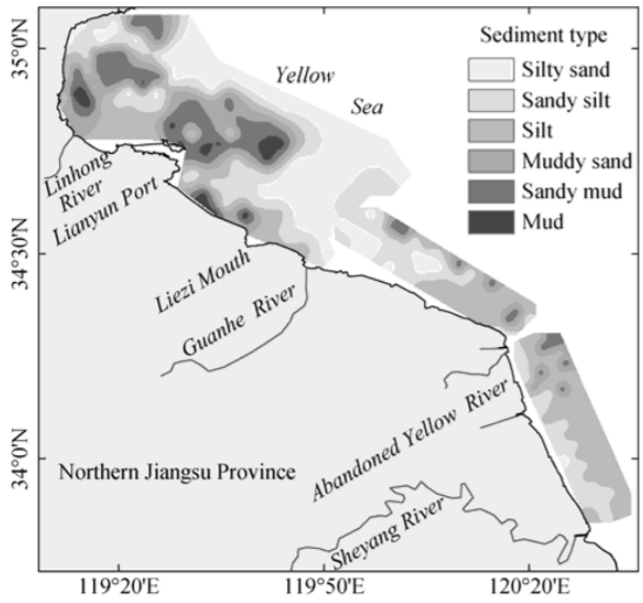

Figure 2.3: Sediment fractions found along the Abandoned Yellow River Delta. Spatial distribution composed from a field campaign dating July 2012 (from Zhang et al., 2014)

In the RSRF mainly fine sand, silty sand and clayey silt are found. Grain size decreases in offshore direction. Fine sand and coarse silt can be found at the ridges. Higher contents of silty sand and clayey silt are found at greater depths of 30 m (Li et al., 2001; Yao, 2016) The tidal flats of the NRSRF differ from the SRSRF. The southern flats are more narrow and composed of coarser sediment. Whereas in the north, tidal flats are wider and composed of fine sediment. The transition can be found at Jianggang (Wang and Ke, 1997).

2.3.3 Sediment transport

The abundant amount of fine sediment found along the Jiangsu coastline is brought easily into suspension by waves and currents (Wang et al., 2011; Zhou et al., 2014). Large SSC are therefore observed at the Western South Yellow Sea (WSYS) (Xing et al., 2010). The SSC flux is closely

Sediment type	Content (%)			Median grain size	Mode
	Sand	Silt	Clay		
Fine sand	70-90	10-20	<5	125–250 μm	2-3ϕ ; single mode
Sandy silt	30-40	>50	<10	62.5-125 μm	4-5,6-7ϕ; single/double modes
Silt	5-20	65-75	<10	16-39 μm	4-5,7-8ϕ; single/double modes
Clayey silt	5-10	>60	20-25	8-39 μm	5-6,8-9ϕ; double modes
Clay	<15	20-25	45-70	4-8 μm	8-9,4-5ϕ; single/double modes

Table 2.1: Characteristics of dominant sediment types found along the Jiangsu coast. Wherein ϕ, (ϕ=log2·D/D0), set as the Krumbein phi scale (from Wang and Ke, 1997)

following the hydrodynamic forcing influenced by the seasonal variability. The East Asian Monsoon induces the YSCC which transports the sediment mainly in offshore and south direction (Zhang et al., 2014). Winds are prevailing from the south-east in summer. Hence, wind-induced waves and currents transport sediment in northern direction. In winter, prevailing winds are from the north-east. These provoke wind-induced waves and currents through which sediment is transported south (Zhou et al., 2014). Yao et al. (2018) underlines the uncertainty if and to what extend monsoon-driven sediment transport can influence nearshore sediment resources.

The residual sediment transport at Haizhou Bay is directed south towards the bay head. This concedes with the local hydrodynamics. Sediment transport at the bay head is directed south-east, while more offshore it is directed south-west. The Northern Abandoned Yellow River Delta (NAYRD) and Southern Abandoned Yellow River Delta (SAYRD) are affected different by the strong tidal currents governing the AYRD. The residual sediment transport at the NAYRD is north-west directed from the tip of the AYRD. The residual sediment transport mechanisms coincide at the Guanhe River Estuary resulting in a sand spit formation prograding seaward (Xie et al., 2008; Zhang, 2012; Zhang et al., 2014). The SAYRD can be divided in a northern and southern part respectively. The residual sediment transport at the northern SAYRD is offshore directed, while in the southern SAYRD it is directed south. The tip of the AYRD has shown a coarsening trend due to the strong tidal currents transporting the fine sediments Xingjian (2011); Zhou et al. (2014); Zhang et al. (2014). A detailed overview is given in Figure 2.4.

2.4 Ecology

The Jiangsu coast comprises large intertidal mudflats that sustain a rich biodiversity and provide in different high-value ecosystem services. Recognisance of the importance has given them a protective status by the Chinese Central Government in 2017, nominating fourteen sections as UNESCO World Heritage site (Chan et al., 2019).

The mudflats are highly valuable for shorebirds and for some species even indispensable. The mudflats serve as stop-over sites and nourish- and roosting sites during non-breading seasons (Melville et al., 2016). Over the pasts decades, bird counting and satellite tracking research revealed the existence of major staging sites along the Yellow Sea coast. Recordings show that 30% of the entire East Asian-Australasian Flyway (EAAF) is supported by the mudflats of the Yellow Sea and counts eleven endangered species (Barter, M.A., 2002; Chan et al., 2019; Battley et al., 2010). The mudflats along the Chinese coastline are part of the EAAF, where migratory shorebirds use the mudflats as their stop-over sites during north- and southward migration (Figure 2.5).

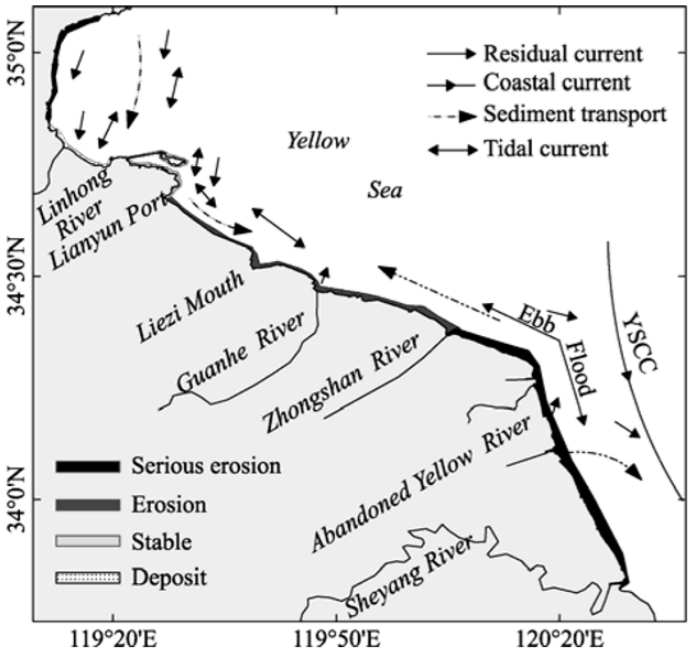

Figure 2.4: Detailed overview of tidal current directions and Yellow Sea Coastal Current (YSCC). The sediment transport is shown by the dashed line. Furthermore, the erosion/deposition areas are denoted (from Zhang et al., 2014)

Since the 1950's, approximately 50% of the total mudflat area along the Chinese coastline has been reclaimed due to rapid economic development and urbanisation (Wang and Wall, 2010; Murray et al., 2014). Mudflat loss has been correlated to a decrease in shorebird population due to the overall loss of direct habitat and degradation of the lasting mudflats by anthropogenic activity. Additionally, recent analysis of bird data has shown steep population declines of shorebird species relying on these mudflats to the largest degree (Melville et al., 2016; Piersma et al., 2017; Chan et al., 2019).

In the 20th century, Common and Smooth Cordgrass (Spartina Anglica, Spartina Alterniflora) were introduced in order to trap fine sediment for land expansion and protection purposes. It has spread aggressively along the Jiangsu coast, which has negative effect on the habitat of certain shorebird species Du et al. (2019).

In order to preserve (near-extinct) shorebird species, it is stated crucial to maintain and restore the mudflats along the Chinese coast. As a result, overall reclamation policy has become more strict and within Jiangsu, a National Wetland Nature Reserve has been set-up at Yancheng county (Bennett et al., 2018).

Figure 2.5: Overview of the East Asian-Australian Flyway in which the mudflats of the Yellow- and Bohai Sea are serving as the main 'hub' for shorebirds (from Piersma et al., 2017)

3 Method

The Abandoned Yellow River Delta is subjected to a complex hydrodynamic system. In order to obtain a better understanding of the hydrodynamic forcing and its corresponding transport patterns, the Jiangsu Regional Model (JRM) is used (Yao, 2016). The model includes the entire Jiangsu coast and is further modified for the Abandoned Yellow River Delta, defined as the Abandoned Yellow River Delta Model (AYRDM).
This chapter depicts the model description, the model configuration and validation methods.

3.1 Process-based numerical model

Use is made of the process-based numerical model Delft3D to examine the hydrodynamic processes in order to simulate the morphological development and to evaluate island configurations at the Abandoned Yellow River Delta. The state-of-the art model can be applied in different coastal environments including complex geomorphological features (i.e. sand spits) (Dan et al., 2011; Deltares, 2019).

Delft3D is a modelling framework consisting of several integrated modules which can be coupled. Altogether these allow the computation of flow, waves, sediment transport, morphology and other phenomena (i.e. water quality and ecology). The core of the modelling suite is the Delft3D-Flow module which calculates the flow by solving the Reynolds-averaged Navier-Stokes equations under the Boussinesq assumption. Calculations are done in 2D (depth-averaged) or 3D setting and based on a staggered grid by a finite difference scheme (Lesser et al., 2004). The Delft3D-Wave module accounts for the inclusion of waves. Wave simulations in coastal areas are performed using the spectral wave model SWAN (Holthuijsen et al., 1993) which calculates short-crested wind-generated waves.
The Wave and Flow module can be coupled one- or two-way. Generally, the one-way coupling meaning that the output of the Wave module is used for the Flow simulation. Whereas in two-way, online, coupling both Flow and Wave modules use the output from the other as their input in order to account for the impact of flow on waves and vica versa. The effect of waves can be taken into account within Delft3D-Flow. Included features are enhanced bed shear stress by wave breaking, wave forcing due to breaking, wave-induced mass flux, turbulence by waves and wave-induced currents in the direction of wave-propagation in the bottom boundary layer (Kaji et al., 2014; Lesser et al., 2004).

Delft3D-Flow has the ability to compute sediment transport for multiple sediment fractions wherein a distinction is made between cohesive and non-cohesive sediments. Sediment transport is computed each half time step and uses the flow results as input. The total sediment transport

is the summation of bed- and suspended transport, which is determined by the partitive reference height proposed by van Rijn (1993). Bed load transport is considered only with non-cohesive sediments and is assumed to respond instantaneous to the flow. The bed load is defined as all transport below the reference height, whereas suspended sediment load is all above. The transport of sediment is computed by the transport formula as suggested by van Rijn (2007a,b,c). Bed- and suspended load are computed separately, in which suspended load is calculated with an advection-diffusion equation. Within this research use is made of a 2D (depth-averaged) setting for both flow and suspended sediment transport (Yao et al., 2018).

Much research has been conducted on sediment transport formulations of non-cohesive, cohesive and a combination of both in clay-dominated environments. However, at the Jiangsu coast mainly a sand-silt mixed environment is found. To extend the knowledge of transport in these environments, Yao et al. (2015) conducted flume experiments considering waves and currents with samples taken from the Jiangsu mudflat. Yao et al. (2015) suggests the use of a multi-fraction approach for which the 2D (depth-averaged) advection-diffusion equation needs to be computed individually, wherein the total sediment transport is the summation of all fractions. Yao et al. (2015) re-calibrated several formulations of van Rijn (2007a,b) through which model results show better accordance with the measurements. As such, Yao et al. (2015) has extended the conventional transport formulation to the silt range (i.e. 8 - 250 µm) and implemented it into Delft3D-Flow. For more details on the multi-fractional 2D (depth-averaged) transport module regarding a sand-silt mixed environment, the reader is directed to Yao et al. (2015, 2018).
Within this study, the available sediment fractions were revised and decreased in order to save computational time. A cohesive sediment fraction has been added as earlier introduced by Muller (2018), for which additional sediment transport formulations were utilised as described by Partheniades (1965). Consequently, changes in bed level are computed at every time step based on the sediment mass balance. The bed level and composition are fixed at open boundaries. The morphological bed changes can be accelerated with the use of a morphological acceleration factor. After each time step, the bed changes are multiplied with a constant factor effectively increasing the morphological time step.

The wave-current model according to Fredsoe (1984) is used during simulations. Yao et al. (2015) describes the enhancement of the critical bed shear stress by current-wave interaction. Hereafter Yao et al. (2015) describes that high concentration layers are seen during wave forcing. These layers are not seen under wave-current forcing, since the current induces a larger vertical mixing of sediments.

The JRM considers many physical processes as described by Yao (2016), which are held identical within the AYRDM. These processes include hindered settling effects for all fractions and flocculation effects of fine sediment fractions (i.e. grain size $<$ 40 µm). Yao et al. (2015) points that mixed sediment's structure plays a role on the erosional behaviour of the bed. Hence,the effects of cohesion and packing density of fresh deposits on the critical bed shear stress are taken into account for a median grain size of the mixed sediment bed smaller than 62 µm (i.e. silt range). Next, the cohesion effects on the critical bed shear stress are taken into account for a median grain size of the mixed sediment bed larger than 62 µm (sand range). Hiding and exposure effects are considered for each fraction when the median grain size of the mixed sediment bed is larger than 40 µm. These effects are implemented by decreasing the critical shear stress for coarse fractions and increasing for fine fractions. Furthermore, bed slope effects on the critical bed shear stress and bed-load transport are taken into account by multiplication with a certain correction factor. Bed slopes can have influence on the threshold of initiation of motion and furthermore change the bed-load transport rate. A wave-related sediment mixing coefficient is calculated in which breaking waves are considered. Hence, the sediment mixing coefficient is

calculated for combined current and wave conditions.

3.2 Model configuration

Both waves and currents are taken into account within this research. Consequently, use is made of both Delft3D-Flow and Delft3D-Wave modules. A general description is given regarding the Flow configuration in which the Jiangsu Regional Model (JRM) and Abandoned Yellow River Delta Model (AYRDM) are elaborated. Then, the Wave configuration is elaborated for which a similar multi-domain approach is used. The bed composition and sediment characteristics are discussed hereafter.

3.2.1 Flow - Abandoned Yellow River Delta Model

3.2.1.1 Domain

The JRM comprises the entire Jiangsu coastline and has two open boundaries. These boundaries are situated just north of the YRE and parallel offshore via open sea to the Shandong peninsula. The model domain constitutes an outline in which a computational grid has been set-up. The grid size counts 573 x 346 cells and has a resolution varying between 655 - 1205 m. The tidal wave propagation has been successfully reproduced in an overall larger model encompassing the entire Bohai Sea (BS), YS and ECS (Su et al., 2015). These hydrodynamic results have been deducted and implemented at the two open boundaries in order to reproduce the tidal propagation within the JRM (Yao et al., 2018; Su et al., 2017a). The JRM has good ability to reproduce hydrodynamic processes in significant high resolution. The same holds for sediment transport and morphological development.

In order to increase the model's accuracy at the area of interest, the grid has been refined and implemented within the JRM (Su et al., 2015). The AYRDM counts 331 x 321 cells and has a resolution of 215 - 345 m. Hydrodynamic data available for calibration purposes however did not overlap the computational grid. The grid has been extended complying with a more recent land boundary (2016). A grid refinement factor of three has been chosen, since a larger refinement would lead to excessive computational time. A grid ratio of 3:1 is reached in comparison with the JRM. More on the calibration of the AYRDM and the grid extension in Appendix B.1.2 and Figure B.4.

The AYRDM is cropped from the JRM leaving three open boundaries between the JRM and AYRDM. These boundaries were carefully chosen in order to obtain minimum depth deviations along the boundaries and maintain a rather compact model. The southern boundary is chosen at Sheyang River Estuary, since the coast transitions from erosive to stable and depositional further south.
Due to coupling, the refined grid needed to be established along the current grid structure through which only a rectangular outcrop could be established. The inter coupling or nesting of both models is attained by using the Domain-Decomposition (DD) approach. This approach is an 'online' coupling method in which both models continuously feedback each other. This 'online' method is chosen due to the highly erosive trends and strong flow near the area of interest. Conventional nesting, regarded as 'offline', knows only one-way interaction from the base- to sub model. The computational advantage of the DD approach is while supporting multiple domains, these can be executed parallel achieving a higher computational efficiency. As discussed earlier, the refinement of the smaller grid leads to a higher accuracy at the area of interest (Deltares,

2019).

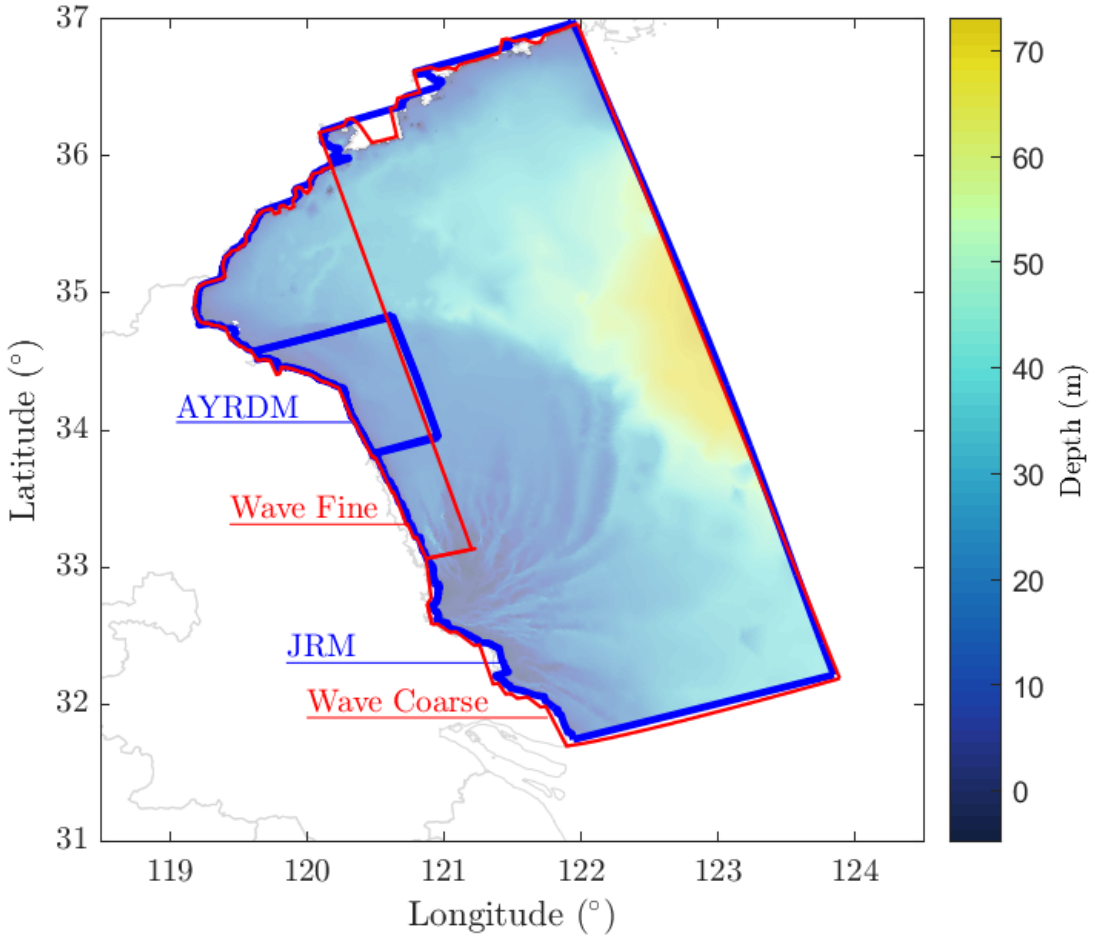

Figure 3.1: Overview of the Flow and Wave computational grids. The grids from the AYRDM and JRM are depicted in blue, whereas the coarse and fine wave grids are depicted in red

3.2.1.2 Bathymetry

The bathymetry of the AYRDM is based on the bathymetry of the JRM. The bathymetry of the JRM is composed of two segments from which the first are measurements of the Radial Sand Ridge Field taken in 2006 (Zhang and Ed., 2012). The remaining is supplemented with Electronic Navigational Charts (ENC's) issued by the Navigation Guarantee Department of the Chinese Navy Headquarters (Yao, 2016).

The model domain has been updated with a recent land boundary (2016), which exceeded the initial land boundary in landward direction at the AYRD. The model domain and consequently the computational grid have been extended to cover the 'gap'. The extended area is not covered by the JRM's initial bathymetry and therefore the local depth is unknown (Figure B.4). The AYRD has been surveyed in 2016 in order to investigate the influence of Binhai Port's breakwaters, which were constructed during 2010 - 2011. The survey data is made available for this research.

In order to verify the model's performance, additional data has been made available. The data includes water levels, current velocities, current directions and suspended sediment concentrations for six stations. Xiangshui station is located in the NAYRD at which water level- and wave measurements have been conducted. All measurements are conducted from a spring-neap tidal cycle in June 2007. Wave measurements however are obtained during 2014-2015. A clear overview of the locations of stations and data availability can be seen in Appendix A.2. Since the AYRD is an erosive coastline and due to the increased morphological changes caused by the construction of Binhai Port, herewith the fact that no port construction had taken place in 2007 and thus hydrodynamical characteristics and morphological changes were not yet influenced by breakwater construction, it is chosen to do an alternative depth calibration based on literature. More on this calibration in Appendix B.1.2.

3.2.1.3 Boundary conditions

The boundary conditions are an important aspect in morphological modelling as these induce hydrodynamic forcing and consequently sediment transport.

The AYRDM is 'online' nested within the overall coarser JRM using the DD approach (Deltares, 2019). The 'online' nesting method provides the exchange of information in time steps between the base- and sub domain continuously throughout the modulation. With a two minute time step information is exchanged at the three open boundaries of the AYRDM including water level, current velocities and sediment concentration. As such, the AYRDM does not demand for pre-set defined boundary conditions since these are provided at each time step by the JRM.

The boundary conditions of the JRM are set-up in order to represent the outer world influence on the model domain. The water level fluctuations within the JRM are derived from time-series of astronomical tides resulting from the output (10min interval) of a large-scale model (Yao, 2016). The large-scale model is comprehending the BS, YS and ECS in which the water level is prescribed by 13 astronomical tidal components ((M2, S2, N2, K2, K1, O1, P1, Q1, M4, MN4, MS4, MM and MF). The tidal components were obtained from a global scale ocean model TPXO7.2, and were calibrated with tidal gauge data situated at its three open boundaries (Su et al., 2015). Due to the extensive area coverage Su et al. (2015) included the influence of 14 rivers along its coastline boundary. Consequently, the Yangtze River influence on water level is included within the JRM prescribed boundary conditions (Yao, 2016).

The Yellow Sea comprises turbid waters due to the presence of high suspended sediment concentrations. These high concentrations are found due to strong hydrodynamics and fine sediment properties. Sediment distribution along the Jiangsu coast is non-homogeneous and ranges from silt to sand. Yao (2016) introduced a multi-fraction modelling approach in order to simulate the morphological processes closely. The JRM is set-up with four sediment fractions found representative for the Jiangsu coastline. These fractions are resembling fine silt, silt, very fine sand and fine sand belonging to the grain sizes 16, 45, 90 and 180 µm respectively. However, within this research only use is made of fractions 16 and 90 µm (more on this in Section 3.2.3.1). Additionally, a cohesive sediment fraction has been added as earlier proposed by Muller (2018).

The JRM is set-up with continuous sediment concentration influx entering the domain at its two open boundaries. Yao (2016) assumed that fluxes entering via the eastern boundary are rather small. He has set the inflow of 16 µm fraction to 0.5 mg/l, while retaining the other fractions zero. An exception is the cohesive fraction, however this will be treated in Section 3.2.3.2. The sediment concentration inflow of the southern boundary has been argued by (Yao, 2016) due to the close presence of the Yangtze River. As discussed earlier, the Yangtze River

derived sediment load is directed Exploratory mainly under the presence of the Min-Zhe Coastal Current (MZCC) (Liu et al., 2007). Seasonal variates occur through which northward transport is present, however to what extent is unclear (Wang et al., 2015). Yao (2016) performed a sensitivity analysis and concluded that the morphological development of Jiangsu is independent of the SSC open boundaries and can be considered a quasi-closed coastal system. Hence, it is assumed that suspended loads enter only at depths smaller than 30 m. The sediment concentration influx regarding the 16 µm fraction (e.g. representative fraction Yangtze River) is set at 100 mg/l nearshore, linearly decreasing to a depth of 30 m offshore (Wang, 2002). From a depth of 30 m to offshore, the SSC is set to a constant of 0.5 mg/l.

3.2.1.4 Tidal forcing

The JRM encompasses a large seashore area with deep ocean sections. The gravitational forces contribute significantly to the water motion. As such, the JRM has included the tidal forcing since it can not be neglected Deltares (2019). Tidal forcing is not included within the AYRDM, since it is focussed on the nearshore shallow area.

3.2.1.5 Secondary flow

The Abandoned Yellow River Delta area has no extensive channel-ridge formation as in the RSRF. Therefore, secondary flow within the RSRF induce significant sediment transport through velocity gradients. The AYRD has its depth contours parallel to the coast. Large velocity gradients are therefore not observed and hence no significant sediment transport by secondary flow is induced. The implementation of islands will increase current velocities around the islands which is the effect of current divergence. This flow circulation is relevant in sediment transport. Hence, secondary flows are initiated which may induce significant siltation around the islands. Consequently, the use of secondary flow is introduced within the AYRDM and JRM. The depth-averaged shallow water equations are therefore extended as described by Deltares (2019), since the model is set-up depth-averaged.

Estuarine circulation is not taken into account within this research, since fresh water run-off by rivers is neglected (see Section 3.2.1.7).

3.2.1.6 Bed roughness

The bed shear stress as caused by the wave-current interaction is calculated as described by Fredsoe (1984) (Deltares, 2018). The Manning Roughness coefficient is used within this research, where $n = 0.01$ s/m$^{1/3}$ is typically for muddy smooth beds and where $n = 0.015$ - 0.02 s/m$^{1/3}$ is typical for sand beds (Maren et al., 2015). The spatial varying roughness as set-up by Yao (2016), has not been changed within this research. However, calibration has been done up on the extended grid area which can be found in Appendix B.2.3. The manning roughness coefficient (n) has been adjusted to a uniform value of $n = 0.014$ s/m$^{1/3}$ for the extended grid cells.

Within the WAVE module, the JONSWAP bed friction is standardized at $C_b = 0.067$ m^2/s^3. This typical sand-bed value is suggested for a fully developed wind-sea state in shallow water (Bouws and Komen, 1983). Another lower value of C_b is suggested by Hasselmann et al. (1973), which corresponds to $C_b = 0.038$ m^2/s^3 and has been assigned to swell conditions. Research by Vledder et al. (2011) firmly suggest the use of $C_b = 0.038$ m^2/s^3 for both wind-sea and swell conditions. Preliminary results with $C_b = 0.067$ m^2/s^3 showed damped wave heights. Within

this research $C_b = 0.038$ m^2/s^3 is used as bed friction parameter. This is supported by the muddy environment. The muddy beds are smooth duo their small grain size. Aside their grain size, no large-scale sand dunes are found in muddy environments. Therefore, the environment can be considered hydraulically smooth (Maren et al., 2015).

3.2.1.7 Salinity

Salinity can amend properties of water and hereby affect both flow velocity and sediment transport (e.g. density driven current). One reason for salinity differences along the coast is by the presence of fresh water supply. Along the Jiangsu coast a few small drainage channels emerge into the SYS. Most of the Yangtze River is bend to the Exploratory. As such, no large fresh water supply is appointed to the Jiangsu coast. The salinity along the AYRD varies from 30% - 32% and is defined as brackish water (Zhu et al., 1998). Therefore, both JRM and AYRDM are set up with a constant salinity value of 30 ppt.

3.2.1.8 Morphological scale factor

Morphological modelling requires much time and large computational power. As such, it is preferential to accelerate the simulation in order to decrease modulation time. In order to meet this demand, Delft3D offers the use of a so-called Morphological Acceleration Factor (MORFAC). The morphological change at each time step is multiplied by the MORFAC in order to efficiently increase the bed level change and enhance long-term morphological modelling (Roelvink, 2006). This technique however induces inaccuracies both spatially and in magnitude. As such, the use of a MORFAC could lead to unrealistic erosional/siltation patterns. A sensitivity analysis need to be performed for the use of MORFAC values. The bed level changes need to be compared for model results when no MORFAC is set. The highest value of MORFAC with least deviations in bed level is chosen.

Research conducted by Su et al. (2017a) has shown satisfactory results on a hindcast regarding the evolution of the Jiangsu coast. A MORFAC of 108 has been used considering a timescale of 300 years. Yao (2016) pointed that the use of a MORFAC could be argued for its applicability within a multi-sediment approach. Muller (2018) has modified the JRM for a higher resolution model at the RSRF are. A MORFAC of 24 has been successfully used in a four year hindcast. Muller (2018) then implemented a MORFAC of 48 in order to obtain a eight morphological year simulation. Since the bathymetry of the AYRD is less complex in comparison with the RSRF, it is chosen to use a MORFAC of 50 in order to simulate ten morphological years.

3.2.2 Wave - Abandoned Yellow River Delta Model

Yao (2016) did not include wind or waves within his research, due to the complexity of spatial and temporal variation and lack of long-term multi-station measurements. The focus was mainly on long term tide-induced sediment dynamics and hence, tidal forcing was sufficient (Yao, 2016). The tide has been suggested as the most important forcing by Xing et al. (2012), where wind and waves are mainly considered of secondary importance. However, multiple studies recognise the importance of waves on sediment resuspension and transport capacity (Zhang et al., 2014; Du et al., 2019). Wang et al. (2012a) pointed the significant increase in bed shear stress under wave-current interaction along the Jiangsu coast. The increased bed shear stress ensures more sediment to be resuspended into the water column and on its turn to be transported along the

coast (Wang et al., 2011). The effect of waves is considered significant for erosion at the AYRD (Su et al., 2017b). As such, waves have been included within this research.

3.2.2.1 General wave description

One-year wave data is made available which originates from Xiangshui station. Xiangshui station is located in the Northern Abandoned Yellow River Delta (NAYRD). Unfortunately, no additional wind- and water level data were available regarding that specific time span. An overview of its location and detailed information about the data can be found in Appendix A.2.
The implementation of waves has been done by setting a wave time series at the two open boundaries of the base wave grid. No additional wave data was available near the two open boundaries which could be used as boundary conditions. As such, the wave data has been calibrated in a pragmatic way by multiple iterations of data editing and implementation at the open boundaries. More on calibration of waves can be found in Appendix B.3.1.2.

The wave direction (dir) has been filtered for directions between 30° and 180°. Wave directions smaller or larger are not achievable within the model at Xiangshui station. The main suggested reason is the lack of wind within the model. The analysis of wave data has shown that waves are measured from the north-west direction, which can only be the result of local wind-induced waves (Figure A.5). Wind data is not available for a similar period and therefore not taken into account. Another reason could be the effect of sheltering due to land boundaries.

The edited wave data has been translated into a Wavecon-file as described in Deltares (2018). The individual wave conditions within the Wavecon-file are set at a 20 minute interval. Stationary wave computations are performed and are exchanged on a 20 minute interval with Delft3D Flow. The boundary conditions are uniformly set at both open boundaries. The JONSWAP bottom friction coefficient has been set to 0.038 m^2/s^{-3}. Furthermore, a 10° directional spread has been assumed. Other settings are held original as described by Deltares (2018).
The calibration- and production simulations differ in time span. The calibration simulations cover four consecutive spring-neap tidal cycles, whereas the production simulations cover a longer hydraulic period. The 20 minute time interval between each wave condition is set in both cases. Therefore, the calibration simulation only runs part of the total year wave data, while the production simulations represent a full year measurement data.

Preliminary results showed that the use of flow characteristics by the wave computations has a decreasing effect on the wave height. Wind effects are not taken into account however proved extremely important. It was decided to not take flow characteristics into account on wave computations. Preliminary results show that small waves, which are dominating, are attenuated significantly by the strong tidal currents.

3.2.2.2 Multiple domain and coupling

The wave simulations are performed on two computational grids in which one grid is refined, i.e. a base- and sub-grid respectively. The wave grids are equally set-up, although a larger mesh size is set. The boundaries of the refined grid are chosen at the RSRF, enclosed by an offshore boundary to the Shandong Peninsula (Figure 3.1). Sheltering effects only results at the RSRF, which is sufficiently far from the area of interest.

The grid size of the base domain counts 145 x 64 cells and has a resolution varying between 3000

- 4800 m. The grid size of the sub domain counts 353 x 141 cells and has a resolution varying between 800 - 1000 m. The refinement factor for wave grids has been set to four, which leads to a 4:1 ratio between the base- and subdomain. The wave grid is overlapping the flow grid at its two open boundaries (Deltares, 2018). The refined grid is nested into the coarser grid by means of 'offline' or one-way coupling. Different as for FLOW, the base domain inputs the sub domain only (Deltares, 2018).

The FLOW and WAVE module are coupled by means of 'online' coupling based on a 20 minute interval in between sequential stationary wave computations.

3.2.3 Sediment - Abandoned Yellow River Delta Model

3.2.3.1 Bed composition

The bed composition of the AYRD is set different from the initial JRM as proposed by (Yao, 2016). The JRM includes four sediment fractions from which all non-cohesive sediments (i.e. 16, 45, 90, 180 µm). These were carefully chosen by (Yao, 2016) after analysing multiple studies of bed samples taken along the Jiangsu coast. (Yao, 2016) introduced a spatial varying bed composition along the entire Jiangsu coast based qualitatively on the present understanding. Preliminary tests pointed the individual contribution of each fraction to the total SSC. Regarding the sediment fractions found along the AYRD (see Section 2.3.2) and in order to save computational time, it was decided to revise the composition of sediment fractions.
The bed composition of the AYRDM has been reduced to three sediment fractions from which two initial non-cohesive are used (i.e. 16 µm and 90 µm) and one cohesive fraction has been added. The 16 µm fraction represents silt, whereas the 90 µm fraction represents fine sand. The addition of the cohesive fraction adds on the pseudo-cohesive environment. The spatially non-uniform bed composition has been redefined, since the reduction in sediment fractions did not allow the same spatial configuration.
A new simplified bed composition has been composed in which each non-cohesive fraction is set for 48.6% of the entire bed layer. A sensitivity analysis has been performed on different bed compositions. The results are shown in Appendix B.3.3. Yao (2016) pointed that a bed layer thickness of six meter was sufficiently thick during a simulation of three morphological years. However, recent research by Liu et al. (2016) on the effect of Binhai Port's breakwater construction states that erosion has increased. Maximum water depths in 2014 ranged between 10 - 14 m at the tip of the breakwater. Considering the effect of enhanced erosion and local initial depth, a bed layer thickness of seven meter was chosen. The bed layer thickness of the cohesive fraction has been calibrated in order to provide for sufficient erodible material. A sensitivity analysis gave acceptable SSC results for a thickness of 0.2 m. Hence the non-cohesive sediment fractions make up for 3.4 m respectively.

The bed layer stratigraphy has been constructed similarly as the JRM. A multi-layer approach has been applied in which bed changes are managed by an active layer, administrating input from each sediment fraction to each layer and each computational grid cell. The top layer (i.e.transport layer) is continuously active in eroding and sedimentation. The transport layer has layer thickness of 0.25 m (Yao, 2016) and is fixed during the simulation. A total of 10 sublayers have been defined underneath the transport layer to define the substrate. These layers are only active when the layer above is in need for additional material. Underneath, a base layer has been defined of 1.75 m in thickness. The multi-layer approach results in a more realistic erosion and sedimentation pattern compared to a single bed layer. More on the latter in Deltares (2019).

Critical bed shear stress for sedimentation	τ_{cs}	$1.00{\cdot}10^{3}$	(N/m^2)
Critical bed shear stress for erosion	τ_{ce}	$2.90{\cdot}10^{-1}$	(N/m^2)
Settling velocity	W_s	$1.00{\cdot}10^{-4}$	(m/s)
Erosion parameter	M	$5.00{\cdot}10^{-4}$	$(kg/m^2/s)$
Specific density	ρ_s	$2.65{\cdot}10^{3}$	(kg/m^3)
Dry bed density	$\rho_{s,dry}$	$3.00{\cdot}10^{2}$	(kg/m^3)

Table 3.1: The characteristics of the cohesive fraction after calibration

3.2.3.2 Suspended sediment

Preliminary results showed instantaneous responses of the depth-averaged SSC to the governing currents. The model results do not fit the measurement data well. Muller (2018) had similar issues and suggested the use of a finer cohesive fraction. In previous studies a profound fluid mud layer was found along the Jiangsu coast due to the high SSC. It was suggested that fine material is easily to be resuspended at lower bed shear stresses (Zhang et al., 2016; Shi et al., 2017). As such, a cohesive fraction was added.
The modified sediment formulations as described by Yao (2016), include the flocculation of pseudo-cohesive sediments larger than 16 μm. The added cohesive sediment fraction can therefore not be modelled according to these sediment transport formula. As such, additional transport formula as described by Partheniades (1965) are set for the cohesive sediment fraction.

The final sediment properties of the cohesive fraction were not yet known. Hence, the cohesive sediment characteristics as suggested by Muller (2018) were implemented initially. Preliminary results did not show good accordance with the measurement data. Further calibration of the cohesive fraction was opted.
Multiple parameters which determine the sediment's behaviour have been subjected to a sensitivity analysis. These parameters are the Erosion parameter M ($kg/m^2/s$), the critical bed shear stress for erosion τ_{ce} (N/m^2) and the settling velocity W_s (m/s). Research by Shi et al. (2018) suggest a threshold value for the critical bed shear stress τ_{ce} found at different depths. For the uppermost 0.02 m of bed within fluid mud layers Shi et al. (2018) suggests $\tau_{ce} = 0.18$ N/m^2. The sub-surface layers are given $\tau_{ce} = 0.29$ N/m^2 due to their increased stability. Both values are the result of wave-current measurements. Due to the coarsening trend at the AYRD, the sub-surface layer value of $\tau_{ce} = 0.29$ N/m^2 is chosen. More on the calibration of the cohesive sediment fraction can be found in Appendix B.2.1.1. The final parameter settings of the cohesive fraction can be seen in Table 3.1.

The Jiangsu coast borders a shallow shelf where high turbid waters occur. The high SSC is caused due to wave-current interaction and is bound to the inner-shelf through e.g. large-scale longshore currents (Wang et al., 2011). The JRM and AYRDM are not set-up with large-scale longshore currents or other phenomena (e.g. wave set-up induced currents). The only residual current is due to tidal motion.
The boundary conditions are carefully investigated for the added cohesive fraction in order to sustain fine sediment supply throughout the simulation. Hence, a six month simulation has been set-up in order to see whether and to what extent the boundary conditions influence the AYRD. The simulation has been set with zero initial sediment concentrations and no bed composition. A uniformly distributed influx of 300 mg/l has been set at the two open boundaries for the cohesive sediment fraction. The results showed negligible amount of SSC at the AYRD after six months.

It can be concluded that the effect of the boundary conditions do not affect the AYRD region to significant extent. Hence, the initial concentrations were varied for similar boundary conditions and no bed composition. The results showed large decline at first, however steadily increase of the SSC over time. More on the calibration and results in Appendix B.3.2.
The boundary conditions of the AYRDM are the same as the JRM due to coupling. As such, the eastern open boundary has been set-up with a continuous sediment influx of 20 mg/l. A low value since the boundary is located at deep water, where no significant influx of sediment is present. The southern boundary is set-up with a SSC starting at 200 mg/l nearshore, linearly decreasing to a depth of 30 m offshore. From here to further offshore it is set to a constant of influx of 20 mg/l. The latter is similar to the approach of the 16 μm fraction by Yao (2016) (i.e. due to the Yangtze River plume deflection (Liu et al., 2007)). Furthermore, the initial concentration of the cohesive sediment has been set to 20 mg/l in both the JRM and AYRDM.

3.3 Model performance

The validation of the model performance is done through qualitative- and quantitative assessment methods in which model results are compared to local retrieved measurement data. In this comparison, results are compared visually and statistically. The approach of the performance assessment is done similarly as by Yao (2016), through which both models can be quantitatively compared.

Measurements were conducted at seven monitoring stations located along the AYRD. The locations of these monitoring stations can be found in Appendix A.2.

The qualitative performance assessment is done by visually comparing time series plots of the model results and measurements. The quantitative performance assessment is done through statistical quantities where model results and measurements are statistically compared. For a coupled hydrodynamic-ecosystem model, Allen et al. (2007) suggests that it is sufficiently informative to evaluate for the Nash Sutcliffe Model Efficiency (ME) (Nash and Sutcliffe, 1970) and Percentage Bias (PB). The statistical quantities, equivalently used in Yao (2016), both include the effect of measurements errors.

The Nash–Sutcliffe model efficiency coefficient is a ratio of variances between the values of the predictions and measurements. The ratio quantifies the variance of measured values and predictions with respect to the mean of the measured data. The ME is sensitive to large outliers and ranges from -∞ to one. The ME including measurement errors, is defined as follows (3.1):

$$ME = 1 - \frac{\sum(\mid m - p \mid - \Delta m)^2}{\sum(m - \bar{m})^2} * 100\% \tag{3.1}$$

where m accounts for the measured values; p are the model results; $\bar{m}$ is the mean value of the measurements; Δm is the error of measurement. Additionally, when the absolute difference of the model results and measurements minus the error in measurement is smaller than zero; the whole term should be zero.
The outcome of ME is classified accordingly to the model performance. This classification is defined as such: Excellent (ME $>$ 0.65), Very good (0.5 $<$ ME $<$ 0.65), Good (0.2 $<$ ME $<$ 0.5) and Poor (ME $<$ 0.2).

The PB is defined as follows (5.1):

$$PB = \frac{\sum[(m - p) \pm \Delta m]}{\sum m} * 100\% \tag{3.2}$$

if (m - p) $>$ 0 than the numerator becomes (m - p) - Δm and when (m - p) $<$ 0 occurs, the numerator is changed into (m - p) - Δm.
The outcome of the PB is also classified into four classes, namely: Excellent ($\mid$ PB $\mid$ $<$ 10%), Very good (20% $<$ $\mid$ PB $\mid$ $<$ 20%), Good (20% $<$ $\mid$ PB $\mid$ $<$ 40%) and Poor ($\mid$ PB $\mid$ $>$ 40%).

4
Model results

In order to gain confidence in the model ´s ability to reproduce the hydrodynamic environment and sediment transport characteristics, a calibration simulation has been set-up spanning a four consecutive spring-neap tidal cycle. The model results are compared with short-term measurement data and furthermore validated visually and statistically. The production simulation is elaborated hereafter for general aspects followed by a comparison of tidal forcing only. The production run comprises a morphological development of ten morphological years.

4.1 Model performance

Within this section the model's performance is elaborated. The model has been set-up as described in Chapter 3 and is set from 15/05/07 - 17/06/07. The calibration simulation covers a four consecutive spring - neap tidal cycle. The model results are evaluated for measurement data comprising a neap- (10/06/07 - 11/06/07) and spring tide (15/06/07 - 16/06/07). The measurement data contains water levels, current velocities, directions and suspended sediment concentrations for the given period. These measurements were obtained from six temporary stations located prior to construction of Binhai Port. Stations B, D and F are treated within this section.
Another station is present at the NAYRD, which is further indicated as Xiangshui Station. These measurements contain water levels during the same neap- and spring tide. Furthermore, wave measurements have been conducted which span from December 2014 until August 2015. The available measurement data is further elaborated within Appendix A.2. An overview of the study area and the station's locations can be seen in Figure 4.1. The stations are shown including the Binhai Port outline. The breakwaters were constructed during 2010 - 2011 and therefore only taken into account during the production simulations. The calibration simulation was set-up without the physical presence of Binhai Port as shown in the cropped sub-figure. Here, the port's outline is shown in order to obtain a spatial understanding.

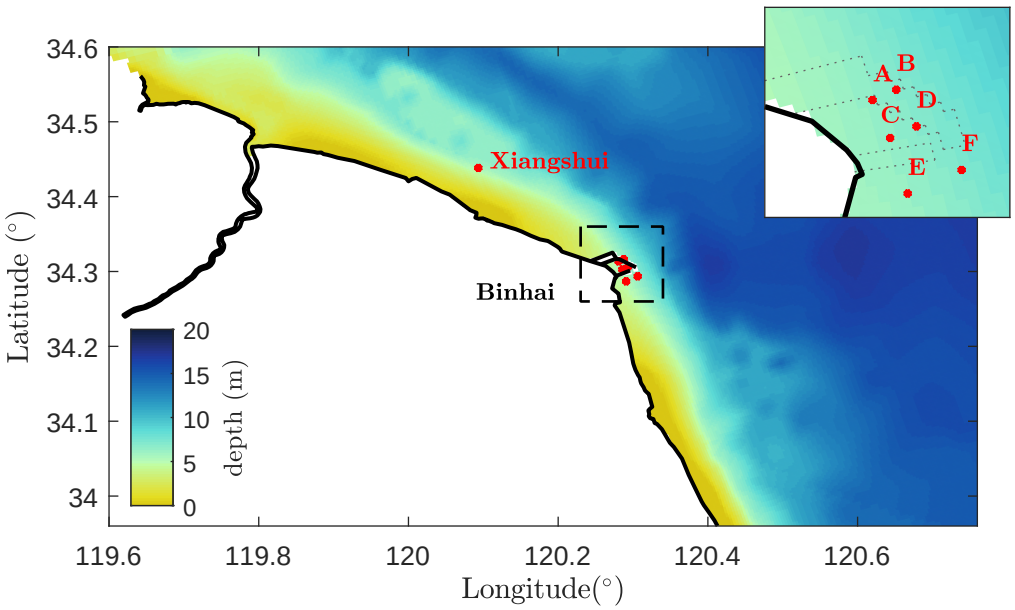

Figure 4.1: Overview of the study area and the locations of measurement stations. The stations at Binhai Port were temporarily present prior to port construction. Binhai Port is only taken into account during the entire production simulations. The cropped sub-figure shows the calibration simulation set-up for Binhai area

4.1.1 Visual validation

4.1.1.1 Flow

Figure 4.2 shows the validation results on Xiangshui Station. The predicted and modelled water level results are plotted against each other. The model is very well capable of simulating the tidal elevation and tidal phase. During neap tide it can be observed that high tides are slightly under-estimated and slightly overestimated during low tide. Yao (2016) found similar tidal results and assigned these errors due to the presence of waves, since his validation data was taken in winter. However, within this research data dates from June when generally small summer waves govern. Therefore, tidal wave deviations can possibly be assigned to low bathymetry accuracy as also suggested by Yao (2016).

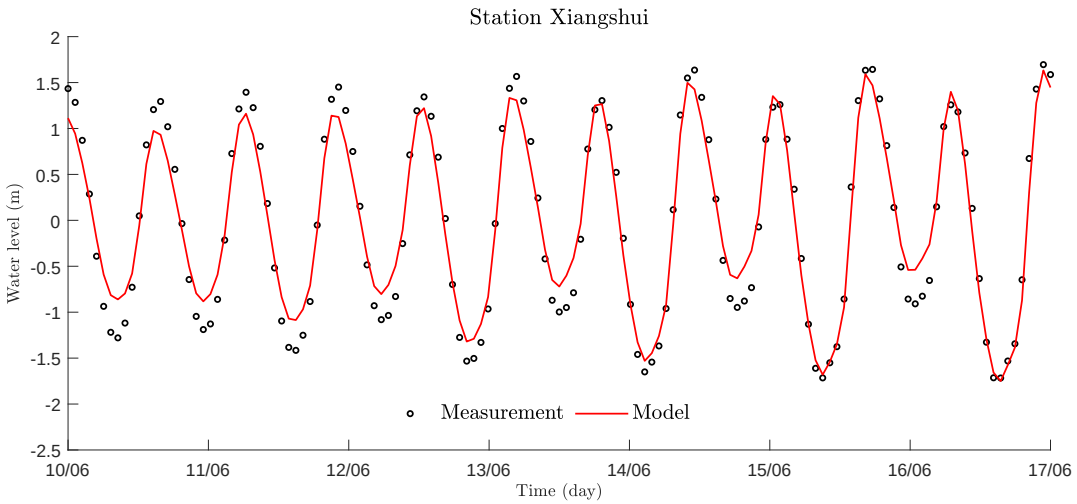

Figure 4.2: Water level at Xiangshui Station during neap- to spring tide

Figure 4.3 shows the water level predictions and modelling results for stations B, D and F, which are located at Binhai. The left and right column show neap and spring tidal results respectively. In general it can be seen that the water level predictions are well reproduced. These good results have been obtained after extensive calibration of local water depth in combination with the Manning's friction coefficient, which is spatially variable as described by Yao (2016). The calibration is further elaborated in Appendix B.1.

Figure 4.4 shows the velocity and its direction for both neap- and spring tide, left and right respectively. The modelling results on the direction agrees very well with the measurements. The current velocity however agrees less on the measurements. The velocity measurements show less variance between ebb- and flood velocities, which are clearly visible for the model results. The model is reproducing higher values for flood velocities than for ebb velocities. Again, these values are the result of extensive calibration due to early issues in bathymetry. Further calibration details are elaborated in B.1.

Figure 4.5 shows the depth-averaged Suspended Sediment Concentration (SSC) for both neap- and spring tide, left and right respectively. The measurement data represent depth-averaged values. In general, it can be seen that the SSC is regularly under-estimated. Station F shows however excellent results at neap tide. Inaccuracies can be assigned to under-estimated flow

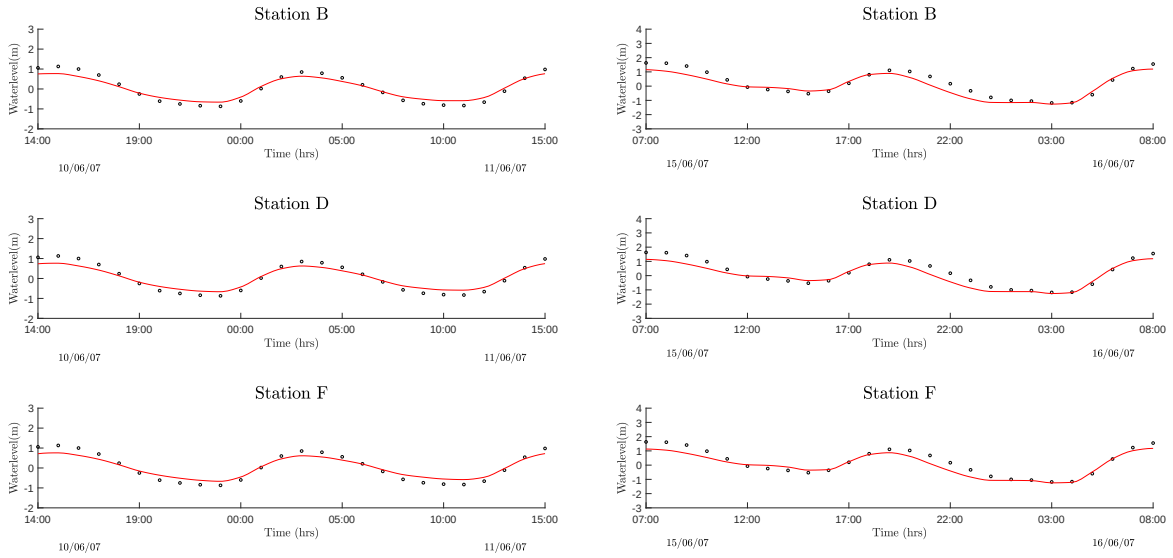

Figure 4.3: Waterlevel at both neap- and spring tide (left, right respectively) for stations B, D and F at Binhai

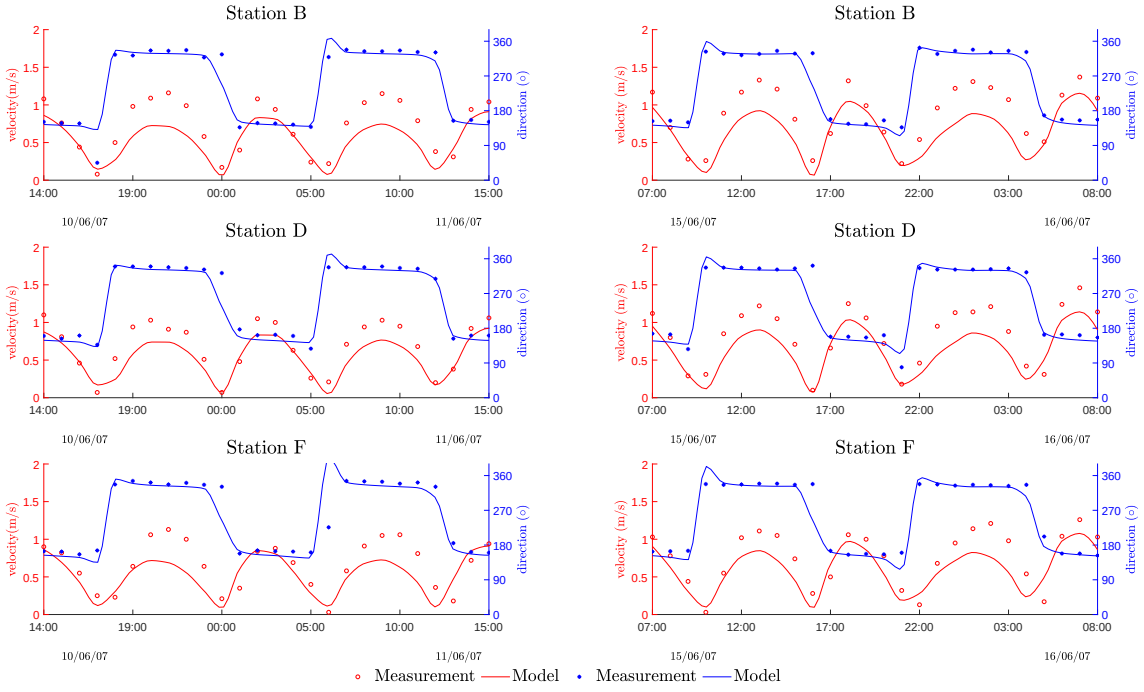

Figure 4.4: Velocity and direction at both neap- and spring tide (left, right respectively) for stations B, D and F at Binhai

velocities and the removal of two initially embedded non-cohesive sediment fractions. Yao (2016)

had similar under-estimations of the SSC. It was suggested that the erosion is reduced by the use of a layered bed stratigraphy within the model.

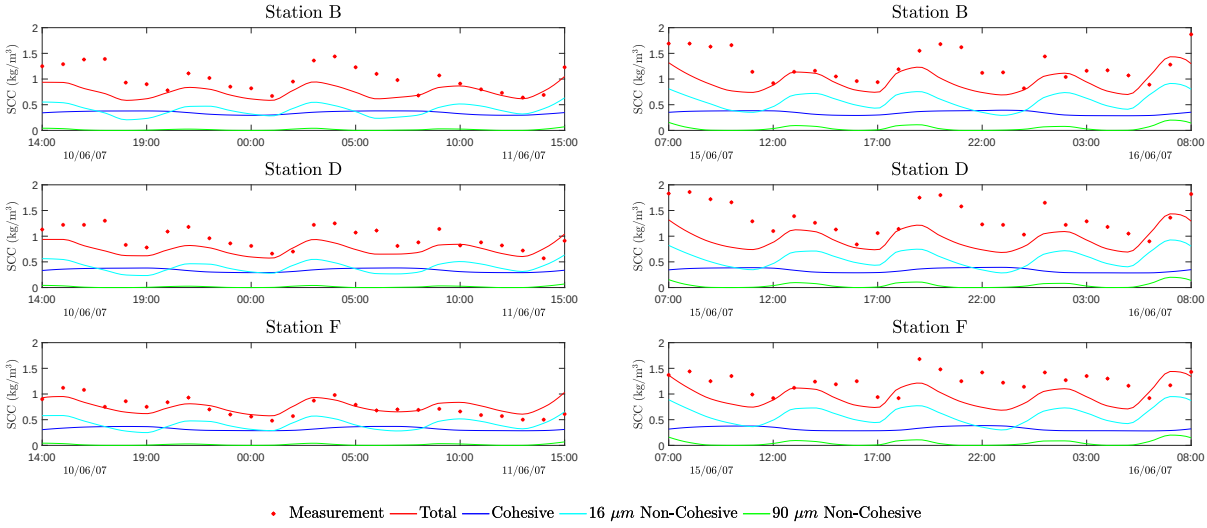

Figure 4.5: Depth-averaged suspended sediment concentration at both neap- and spring tide (left, right respectively) for stations B, D and F at Binhai. The measurement data is depth-averaged

4.1.1.2 Wave

The wave results from the calibration simulation are shown in this section. The calibration simulation was set from 15/05/07 - 17/06/17, comprising a four consecutive spring - neap tidal cycle. The calibration simulation approximately runs through half of the wave conditions set in the production run, since a constant 20 minute interval was chosen between wave conditions. The base wave grid contains two open boundaries at which equal wave time-series have been implemented.

Figure 4.6 shows the measurement- and model results for the significant wave height (H_s), wave direction (dir) and peak wave period (T_p) at Xiangshui station. Sub-Figure A shows the model predictions of the significant wave height, which fit the measurements very well. Large waves however tend to loose their wave height quite easily nearshore, which can be seen within this figure. These under-estimations of large waves can be caused by inaccuracy of the bathymetry and wave grid coarseness. However, preliminary results of using an extra refined grid did not show significant difference. Another point is the lack of wind within the model. Large waves are induced by strong winds. When wind data would have been implemented, it would have exerted a shear force over the wave domain and hence increase wave heights. Wind data was however not available and therefore not taken into account.

Sub-Figure B shows the measurement- and model results of the incoming wave direction (dir). The model results show reasonable resemblance to the measurements. The model is able to reproduce directions between 40° - 115°. It show good resemblance for incoming waves from the north-east, however poor results on incoming waves from the south-east. After extensive calibration and testing, these inaccuracies are believed due to refraction and the lack of wind within the model. The wave station is sheltered behind the tip of the AYRD which complicate the incoming waves from the south-east. Since the area between the tip of the AYRD and Xiangshui station is shallow, the process of refraction deflects the incoming waves to shore normal. The NAYRD coast has a wide shallow coast which deflects to the west in northern direction. The incoming waves are hence for over a longer distance deflected due to this coastal feature. It is therefore suspected that southerly waves are therefore induced by local wind. The wind data shown in Appendix A.2.4, shows measured wave directions from the north-west, west and south-west, which can only be induced by local wind.

Sub-Figure C shows the model results of the peak wave period (T_p). In general, it can be seen that measurements and model predictions show a reasonable fit.
The model results of the significant wave height, wave direction and peak wave period are enlarged shown in Appendix B.3.1.3.

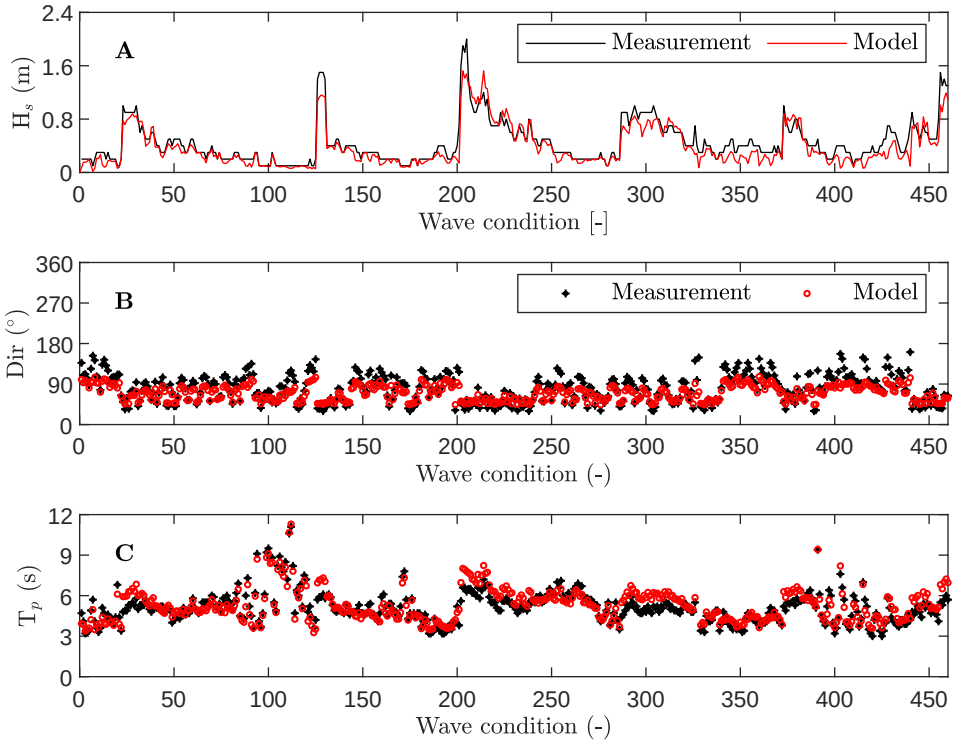

Figure 4.6: Comparison of measurements with model results on significant wave height (H_s), wave direction (dir) and peak wave period (T_p). Measurements and model results from Xiangshui station

4.1.2 Statistical validation

4.1.2.1 Flow

Figure 4.7 shows the statistical validation of the water level results. All seven stations are considered herein.
The Model Efficiency coefficient shows 'excellent' results for all stations. The Xiangshui Station scores significant higher than the other at Binhai. The Percentage Bias method shows 'good' results for Binhai's stations and 'very good'. The stations at Binhai perform slightly less. Reason could be found in inaccuracy of the bathymetry.

Figure 4.8 shows the statistical validation results considering current velocity, direction and the depth-averaged SSC at Binhai's stations. In general, the results are fairly good however differences can be seen between stations.
The Mean Efficient coefficient concerning current velocity shows 'very good' results for stations D, E and F. The other stations A and B show 'good' results, whereas Station C shows a 'poor' result. The wave direction, here denoted as angle, scores as 'excellent' for every Station with exception of E (very good'). The suspended sediment concentration shows 'good' results at Station F, however for all others it shows negative values. As discussed earlier, the ME reacts strongly. The Percentage Bias shows similar results as the Mean Efficient coefficient, however SSC shows significant better results due to the different approach. The SSC show 'good' results for all stations with exception of Station F, which shows 'very good' results. The angle (direction) scores 'excellent' in general with exception of Station E ('very good').

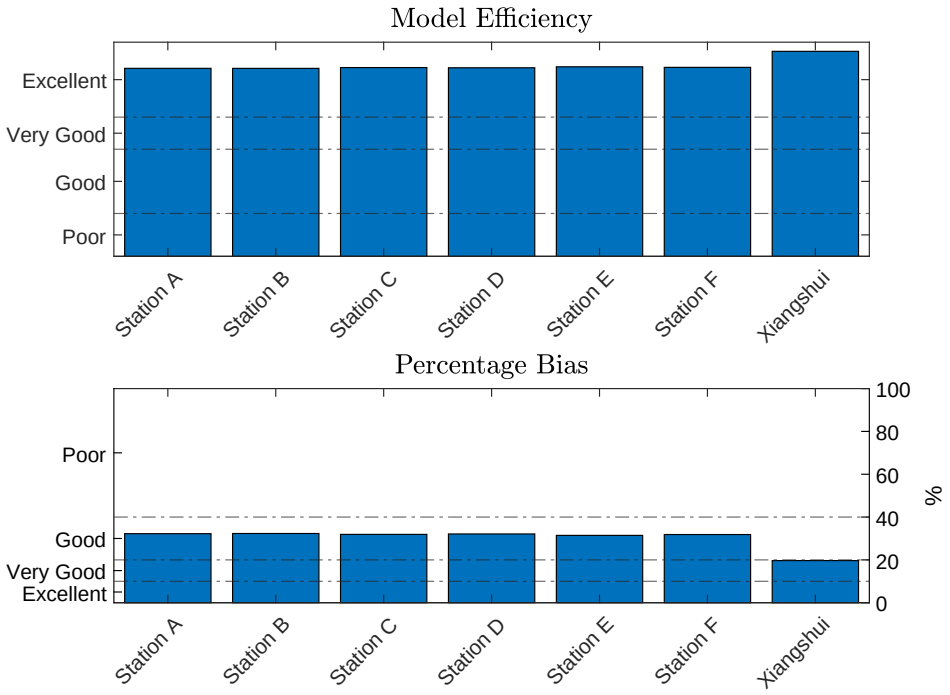

Figure 4.7: Statistical validation of all stations concerning water level. Considering the Model Efficiency coefficient and Percentage Bias

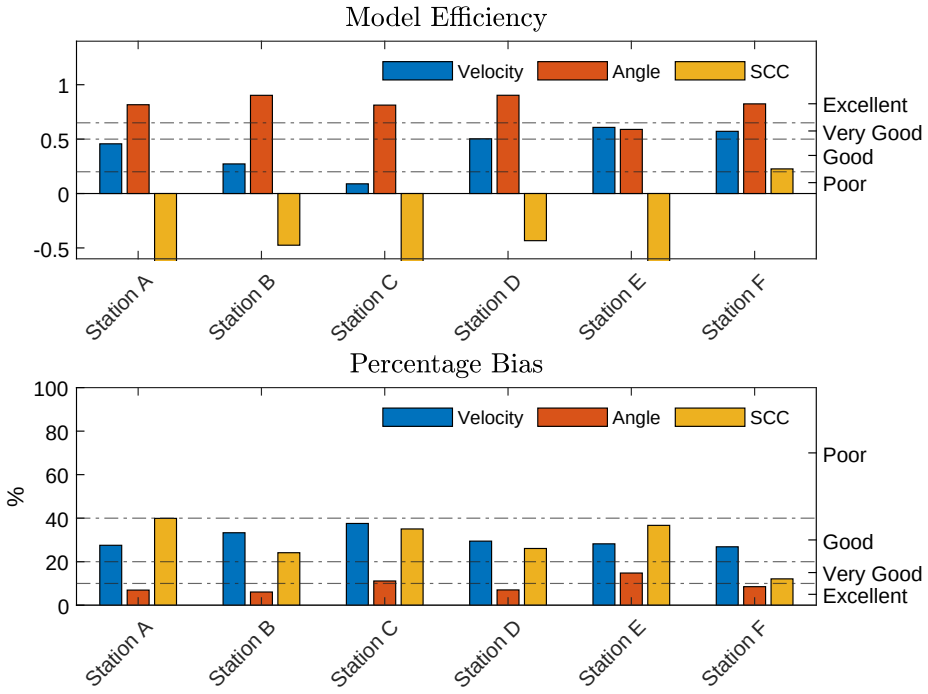

Figure 4.8: Statistical validation of all stations concerning current velocity, current direction and suspended sediment concentration. Considering the Model Efficiency coefficient and Percentage Bias

4.1.2.2 Wave

Figure 4.9 shows the wave validation results. The Model Efficiency coefficient shows a 'very good' result regarding the significant wave height (H_s), although negative scores are obtained regarding direction (dir) and peak wave period (T_p). The Percentage Bias results show 'good' results for both the significant wave height and direction. The peak wave period scores 'poor'.

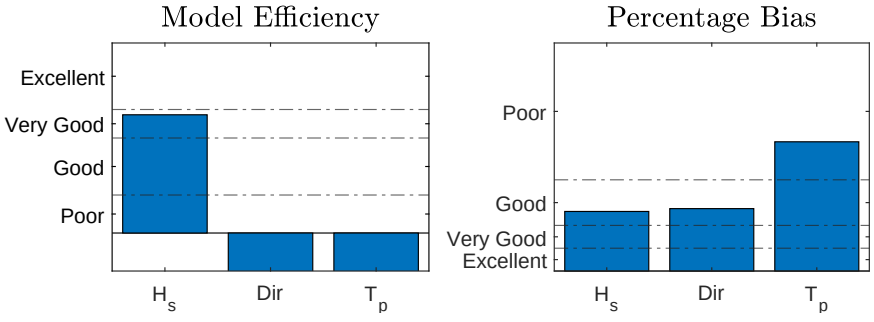

Figure 4.9: Statistical validation of waves measured at Xiangshui Station

4.2 Tidal dynamics and sediment transport

The model has been verified in the previous section by analysing the calibration simulation. It provides satisfactory results in its ability to reproduce the hydrodynamic environment and sediment transport characteristics. The calibration simulation is further elaborated in two dimensions in order to obtain a better understanding of the Abandoned Yellow River Delta and its dynamics. The following findings are the result of a high temporal resolution simulation of one hour.

4.2.1 Tide

The maximum tidal range is calculated for the entire Abandoned Yellow River Delta Model, which is shown in Figure 4.10. The results show good agreement with literature. The tidal range increases from the tip of the AYRD towards the northern end of the NAYRD. Furthermore, the tidal range increases southward along the SAYRD in direction of the RSRF. In Table 4.1 and overview is given of the mean spring tidal range, Mean High Water (MHW) and Mean Low Water (MLW) for Binhai and Xiangshui. Station A represents the Binhai area. The MLW is the mean of all low tides, where the MHW is the mean of all high tides. Literature describes a tidal range of 2.7 m in NAYRD, 1.8 m at the tip of the AYRD and 1.6 m in the SAYRD (Liu, 2011), which coincide well with the mean spring tidal range values.

Tide	Mean spring tidal range (m)	MHW (m)	MLW (m)
Binhai	2.01	0.78	-0.74
Xiangshui	2.79	1.05	-0.88

Table 4.1: Maximum and mean tidal values relative to mean sea level. Station A represents all stations at Binhai

The mean tidal current (depth-averaged) pattern is determined hereafter. The direction and magnitude of the mean tidal current can be seen in Figure 4.11. Distinct higher velocities are observed on the nearshore shoals at the NAYRD. The velocity is slightly less in between land and the offshore shoal, which is bound by the eight meter depth contour. Hence, magnitudes are slightly smaller due to the larger depth in between the shoals. Zhou et al. (2014) describes that the offshore shoal de-connects from shore due to the strong tidal currents entraining sediment. Overall, it can be seen that the current is south-east directed in the NAYRD. Furthermore, the direction just of the eight meter depth contour is directed offshore / eastward. In the SAYRD the current direction is offshore / eastward. As similar to the NAYRD, the current velocities are larger in shallow areas and decreases significant in magnitude just offshore. As a result, it can be concluded that the NAYRD has a larger shallow area in front of its coast compared to the SAYRD, which is confirmed by a bed slope analysis of initial- and modelled cross-sections. The latter can be seen in Figure 4.16. The mean current at the tip of the AYRD is directed south and becomes significantly smaller just offshore.

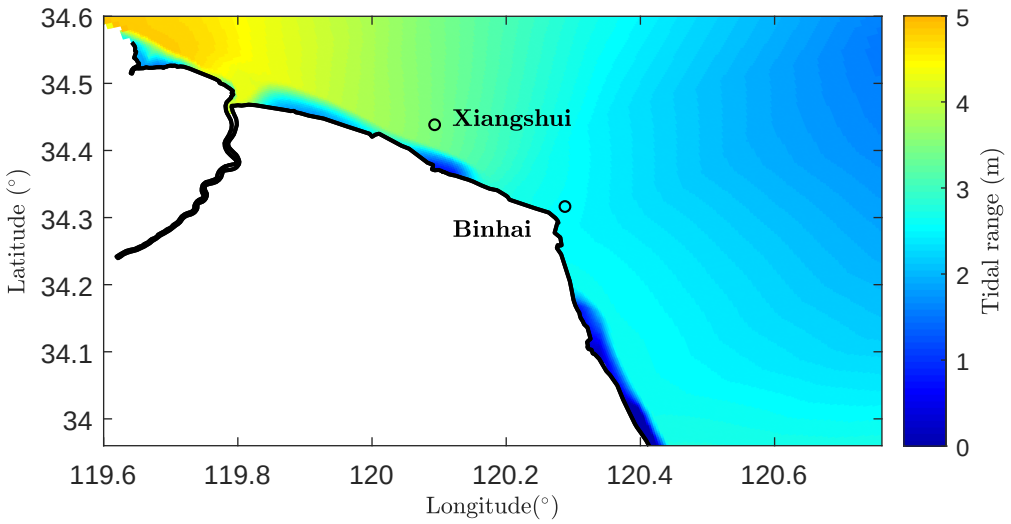

Figure 4.10: Maximum tidal range along the Abandoned Yellow River Delta

4.2.2 Sediment transport

The total mean sediment transport (depth-averaged) has been calculated for all sediment fractions. The results are shown in Figure 4.12. The sediment flux alongshore is mainly directed southward. The observations coincide with the expectations, since the area was earlier denoted as flood-dominant and hence residual sediment transport is directed south (4.1.1). The magnitude of sediment transport increases just offshore and hereafter decreases again, which coincides with the larger flow velocities observed nearshore (not shown here). The northern situated river mouth (old branch of the former Yellow River) is naturally trapping sediment, which is also read in literature.

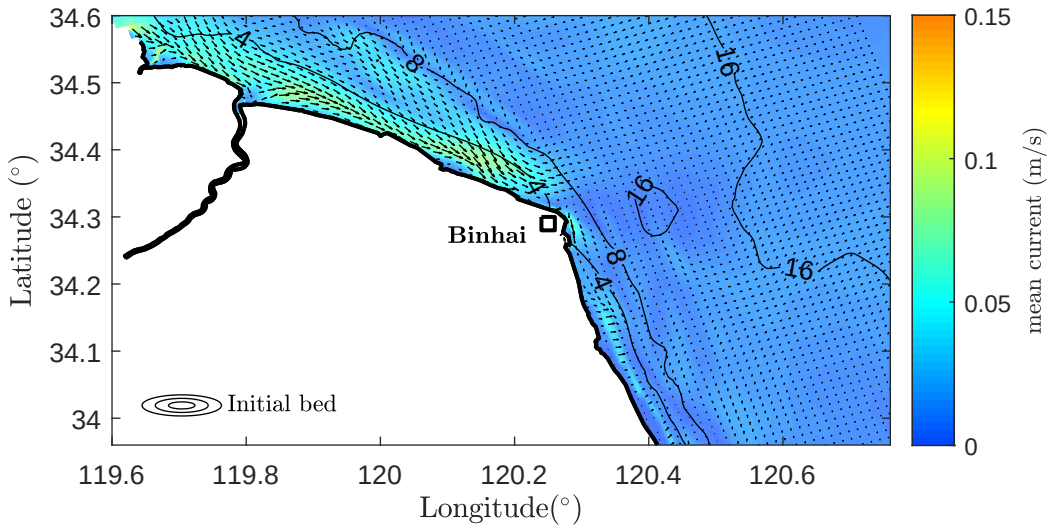

Figure 4.11: Depth-averaged mean current pattern at the Abandoned Yellow River Delta

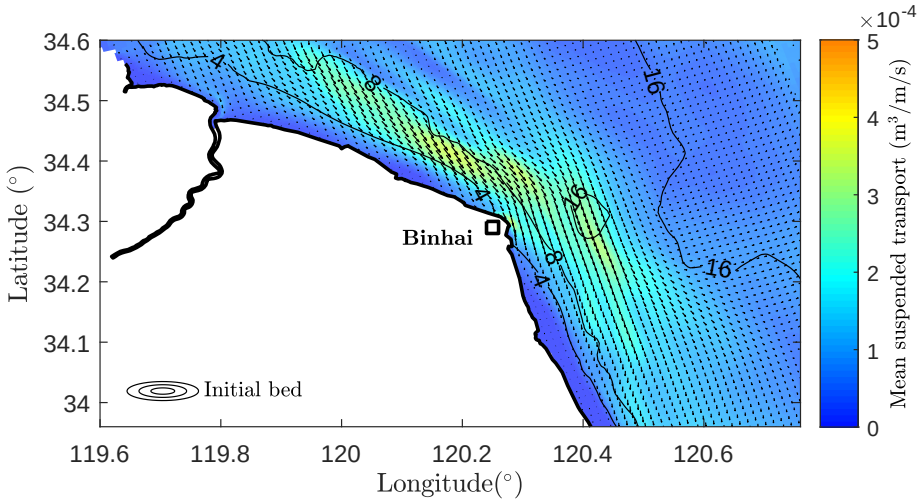

Figure 4.12: Depth-averaged mean suspended sediment transport for all fractions at the Abandoned Yellow River Delta

4.3 Morphological development

The production simulation is set-up for a longer time span in order to calculate ten morphological years of development along the Abandoned Yellow River Delta. The model has been set from 05/04/07 - 17/06/07 and comprises ten years by using a MORFAC of 50. Within this research the effect of waves is taken into account by a full one-year wave time series on the two open boundaries of the base wave grid. This time series is set over the full simulation time span. In order to gain better insight in the effect of waves, production simulation results will be shown of tide-only and wave-current forcing. The results of wave-current forcing are discussed and taken as future reference. The production simulations include the phsyical presence of Binhai Port during the entire simulation.

A good understanding of the sediment pathways within the AYRDM is important. Hence, a sediment budget analysis has been performed for the reference production simulation. Several cross-sections were assigned over the domain including borders, through which certain cells originated. These cells are denoted by a letter. Each cross-section is set with their total sediment transport rate over the considered section in 10^7 ton/year. The results are shown in Figure 4.13. An overview of the cells and its erosional or siltation trend can be found in Table 4.2.
The entire AYRDM shows a net sediment loss of $34.4 \cdot 10^7$ ton/year. The northern border of the AYRDM shows an anti-clockwise circulation trend around the present shoal. The effect is also seen in flow results which are not shown here. Hence, due to the rotative flow an outgoing sediment flux is seen at the north-eastern section and a large incoming flux at the north-western boundary. The offshore northern section shows a small sediment influx. Overall sediment transport is directed south and offshore. All cells are considered erosive except for cells A, I, J and L. Cell A is located in the NAYRD where large siltation is found near the present river mouth. Cell I and J enjoy a siltation status due to the large erosion observed at Binhai's breakwater tip. The effect of flow contraction and hence increase of current velocity entrain sediment and deposit just south of the port. Siltation within the port occurs with a rate of $0.13 \cdot 10^7$ ton/year. Northward transport along the NAYRD is not seen, since the seasonally large-scale currents are not taken into account.

Zone	Location	Total transport (10^7 ton/year)	
A	NAYRD	+1.2	Siltation
B	NAYRD	-0.5	Erosion
C	NAYRD	-2.3	Erosion
D	NAYRD	-3.3	Erosion
E	NAYRD	-2.1	Erosion
F	Offshore	-61.4	Erosion
G	SAYRD	-0.1	Erosion
H	SAYRD	-0.3	Erosion
I	SAYRD	+1.1	Siltation
J	SAYRD	+0.2	Siltation
K	SAYRD	-2.1	Erosion
L	Binhai Port	+0.13	Siltation

Table 4.2: The allocated transport zones within the Abandoned Yellow River Delta Model. The zonation as indicated in Figure 4.13 features siltation or erosion and the total sediment flux in 10^7 ton/year

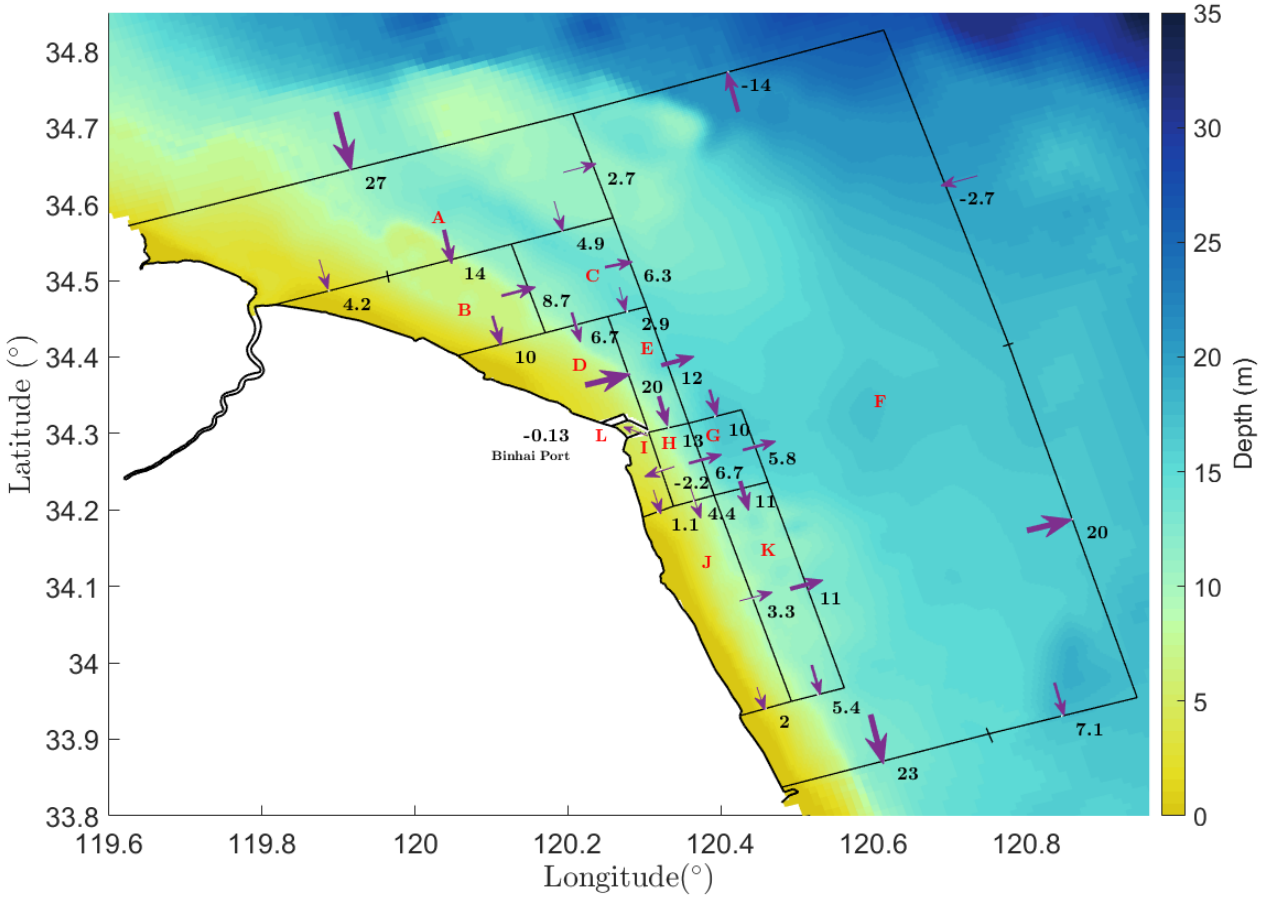

Figure 4.13: Sediment pathways within the Abandoned Yellow River Delta Model (AYRDM). Total sediment flux in 10^7 ton/year

The morphological development of the production simulation is further elaborated in more detail. In order to obtain a better understanding of the effect of waves at the AYRD, the production run has been set for two forcing scenario's. The first scenario comprehends the effect of tidal forcing only. The results can be seen in Figure 4.14. The protruding area is eroded most due to the large current velocities, which is the main principle smoothing the coastline. The Binhai Port breakwaters induce flow contraction which goes along with rapids. Hence, a larger sediment transport capacity is reached for which sediments were entrained. These sediments were deposited mainly just south of the Binhai Port and along the coast of the SAYRD. The shoals just south of Binhai Port are crossed by two small channels created by the tidal flow. Furthermore, significant siltation is observed at the offshore shoal in the NAYRD. The siltation may be the result of longshore sediment transport due to eroded sediment from the area of maximum flow contraction. Although, it may be derived from southward sediment transport into cell A (Figure 4.13). Slight siltation is observed just north of the Binhai Port and significant siltation near the river mouth.
The addition of waves, denoted as wave-current forcing, lead to the results shown in Figure 4.15. Obvious changes in the erosion - siltation pattern can be observed. Waves cause a smoothing effect of high siltation regions. The offshore shoal in the NAYRD shows a significant reduced

amount of siltation by approximately 40 - 50%. Just south of Binhai Port the siltation pattern has been smoothed by the waves. The clear tidal channels disappeared and slightly reduced siltation is seen, which also holds for the SAYRD coast. The river mouth situated in NAYRD shows an increase in siltation, which may be the effect of higher SSC and the natural sediment trapping character. Binhai Port shows siltation due to the large breakwaters creating a low energetic environment.

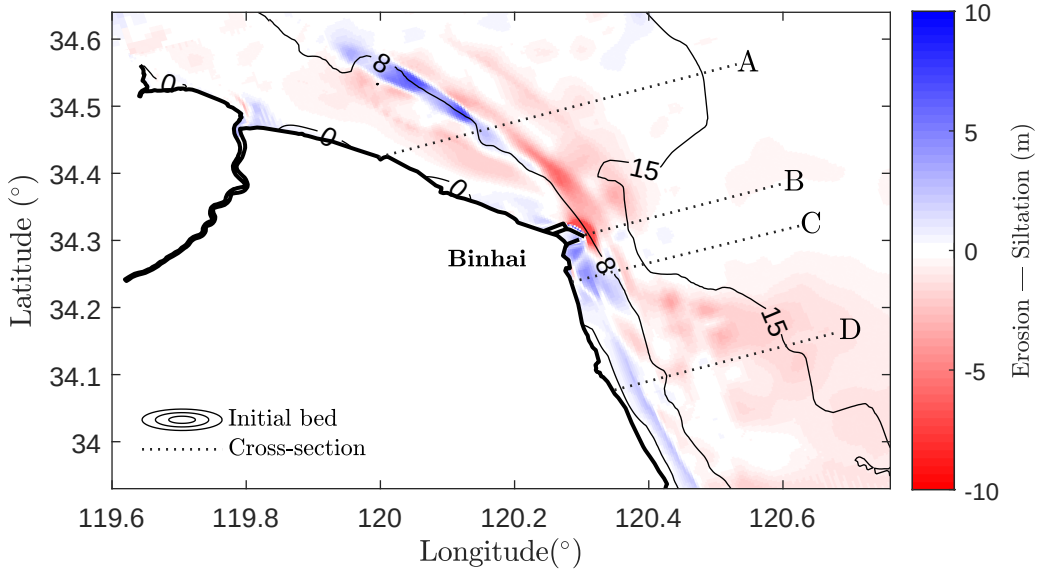

Figure 4.14: Ten year morphological simulation at the AYRD; results from current forcing only. Overview of siltation (blue) and erosion (red) patterns around Binhai Port

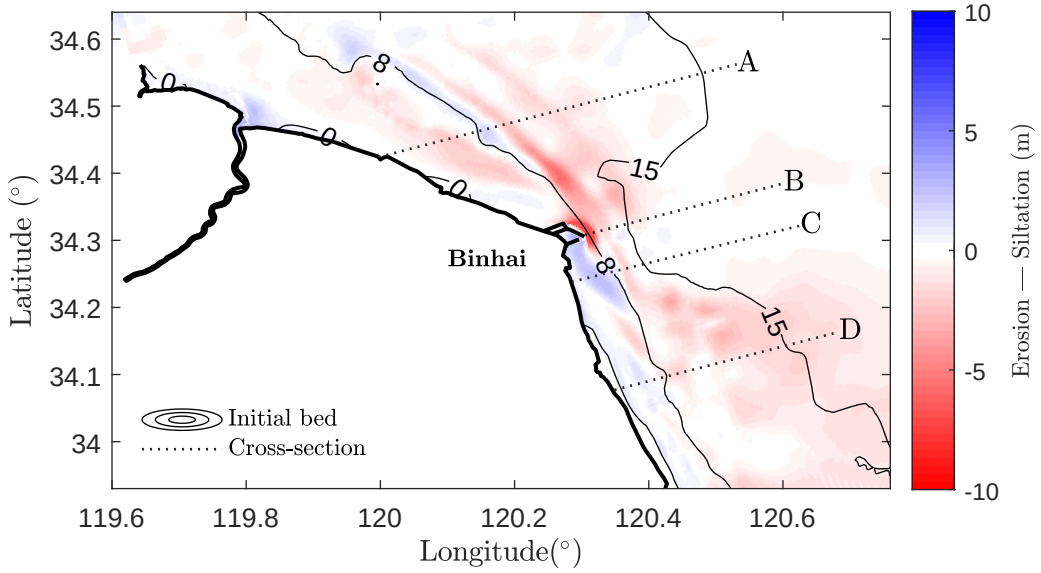

Figure 4.15: Ten year morphological simulation at the AYRD; results from wave-current forcing. Overview of siltation (blue) and erosion (red) patterns around Binhai Port

The ten year morphological development is further elaborated by four pre-set cross-sections along the AYRD. The locations of these cross-sections can be seen in Figure 4.14 and Figure 4.15. The results are shown in Figure 4.16.
In general, it can be observed that the bed slope of the northern- and southern AYRD show a distinct difference. The bed slope of the NAYRD is smaller (A) in comparison with the SAYRD (D). Cross-section A is set over the offshore shoal in the NAYRD. The smoothing effect of waves is clearly shown regarding the shoal at 20 km offshore. Cross-section B is set over the tip of the Binhai Port breakwater from where significant increase in depth is visible and a small decrease in depth further offshore. Large flow contraction is observed here for which large flow velocities occur. Hence, sediment is easily entrained. Cross-section C is set over the siltation area south of Binhai Port. The waves show a smoothing effect of the siltation pattern resulting from tide-only forcing. The sediment is displaced near- and offshore. Similar sediment displacement can be seen in cross-section D.

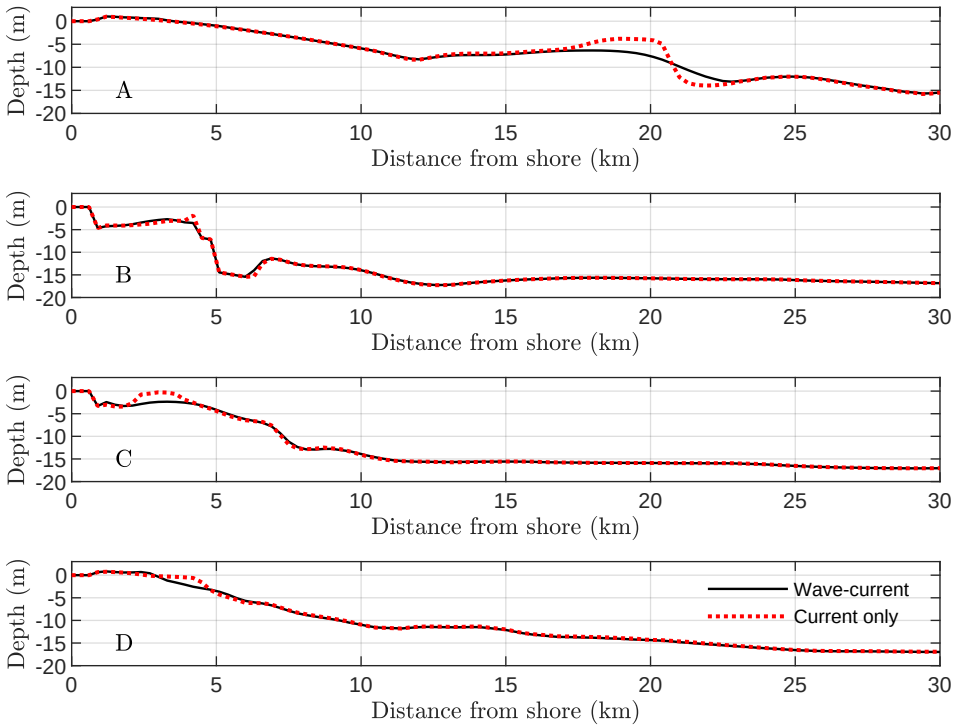

Figure 4.16: Depth along cross-sections at the Abandoned Yellow River Delta. The bathymetry are the result from current-only (red) and wave-current forcing (black)

The Binhai Port breakwaters were constructed during 2010 - 2011 (Liu et al., 2016). Research by Liu et al. (2016) has shown the erosion - siltation patterns along Binhai Port after ten morphological years. Two surveys were conducted in 2004 and 2014 respectively. It is hypothesized that the morphological changes are mainly due to Binhai breakwater construction. Hence, model results of three year morphological development were taken from the production run. The results were compared with the erosion - siltation pattern found by Liu et al. (2016), which is shown in Figure 4.17. Liu et al. (2016) indicates siltation as positive values (shown red) and negative values (shown blue) represent erosion. The opposite of the indications used within this analysis.

Overall, the model shows well resemblance with the results from two surveys. Similar siltation patterns are observed just south of Binhai Port, although the model's erosional predictions are spatially limited. The surveys show a siltation area in triangular form , whereas the model predictions show an initiating triangular form. Investigation of local current velocities show a steep decline in magnitude south of Binhai Port. Transport capacity is reduced as a result which features siltation. The velocity decrease might be the result of bathymetry inaccuracies as discussed earlier. Here, the erosional trend is not very well reproduced by the model. Furthermore, slight siltation can be seen just north of the port in both illustrations. Although some deviations are seen an overall conclusion can be drawn that the predictions are acceptable.

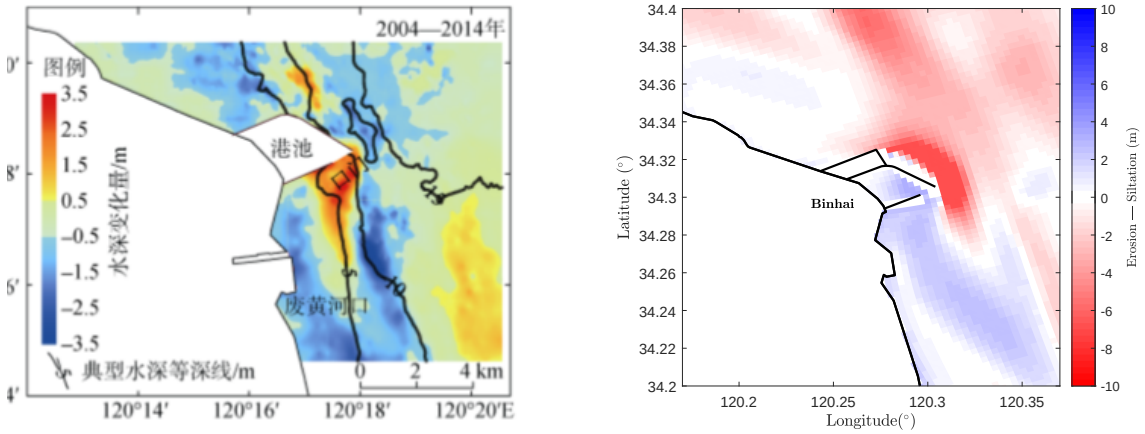

Figure 4.17: Erosion - siltation pattern comparison between survey data from (Liu et al., 2016) (left) and modelling results (right). The survey data time span is from 2004 - 2014, from which is hypothesized that main morphological development occurred after breakwater construction (2010 - 2011). The model results comprehend three morphological years after wave-current forcing

5 Island configuration

The preceding chapter has given a good understanding of the model's hydrodynamic processes and sediment transport characteristics along the Abandoned Yellow River Delta (AYRD). The erosive AYRD can be protected by different innovative solutions by following the Building with Nature approach. Within this research it is aimed to protect the AYRD by implementation of islands in front of the coast. This chapter elaborates on the island configuration design. The designs are implemented within the reference production simulation. Therefore, the shown simulation results comprehend ten years of morphological development. First, Section 5.1 elaborates on the design process. The designs are then elaborated within Section 5.2, which consist of two design series: the Basic- and Exploratory series. The optimal design is then elaborated in Section 5.3.

5.1 Design process

Designing in general is a cyclic process in which several steps need to be followed. The design process commonly used in engineering practice is likewise used within this research. The design process consists of four steps, which are called the analysis, synthesis, simulation and evaluation step respectively. This approach is indicated as an iterating process from coarse to fine to the endeavoured end.
Several Island configurations have been tested at first, in order to see hydrodynamic- and therewith morphological response. These are not added to the report. Two series of island configuration are designed consisting of eight and seven configurations each, the Basic- and Exploratory series respectively. The Basic series constitute to a better understanding of systematic island configuration, resembling barrier island formation. The Exploratory series are developed from perspective of the natural system, taking into account socio-economic factors.

5.1.1 Analysis

The gained understanding in previous chapters is fundamentally used within the design process. The intention of the analysis is to obtain a full understanding of the hydrodynamic- and morphological processes within the design area. This comprehension ensures the right formulation of design criteria and design consequently.
The AYRD is an erosive coast, which is threatened by continuous shoreface erosion undermining the present sea defence. The entire AYRD needs to be protected due to the high demand for land and existing socio-economic activity. Following the Building with Nature guidelines, it is

chosen to implement islands in front of the AYRD as one out of many conceivable solutions. The island implementation will protect the hinterland and enhance siltation in front of the AYRD. By constraining currents and wave attenuation, a less-energetic environment will be created through which fine sediment can settle. The latter will induce mudflat growth which on its turn provide roosting- and nourish grounds for shorebirds. The scope does not incorporate further on ecology and construction details of the islands itself.

This gained insight gives the following design criteria:

- The island configuration should protect the entire Abandoned Yellow River Delta.
- The island configuration should induce siltation along the entire Abandoned Yellow River Delta.
- The island configuration should induce maximum siltation for minimum island surface area.

5.1.2 Synthesis

The synthesis follows after a full comprehension of the design area and its processes. The synthesis pursues to enclose all gathered information and design criteria into alternatives. Within this step the Guidelines of the 'Building with Nature' are applied (de Vriend et al., 2014; Ecoshape, 2020).

The island configuration should protect the entire Abandoned Yellow River Delta, which is easily achievable by implementing islands along the coast. Siltation occurs when a less-energetic environment is created, which is attained by the construction of islands. Island dimensions however must be carefully chosen for unfavourable and unrealistic circumstances to be avoided. Therefore basic comprehension needs to be attained for which the Basic series is created. Herein a barrier island concept is tested for island dimension, number, inlet-size and distance relative to shore. The islands will not be submerged.
The mean suspended sediment transport along the coast is in south direction. This suggests the trapping of sediments at the southern ends, NAYRD and SAYRD respectively. The trapping of sediment enhances sediment accumulation alongshore over time, however groynes perpendicular to shore will not attenuate waves. Hence, it is suggested to implement islands which will attenuate waves. The shoal in the northern NAYRD shows natural accretion. From a 'Building with Nature' perspective it might be interesting to stimulate island growth at that specific area. The shoal will naturally attenuate waves, hence protecting the NAYRD. These suggestions are captured within the Exploratory series.

5.1.3 Simulation, Evaluation

The well-developed designs are finally implemented into the calibrated/validated model. The results are then evaluated for all design criteria.

The design criteria impose a maximum mudflat area growth while implementing as little island area as possible. In order to evaluate for this criterium a definition of mudflat must be set. Xiangshui station can be found at approximately the middle of the NAYRD. Since the tidal range is increasing from the south to north, this station is chosen to determine the minimum depth value for the mudflat definition. The mudflat is defined as all above MLW. The MLW at Xiangshui is 0.88 m and therefore the mudflat definition is set to 0.88 m to -∞ (positive depths

are considered). It is assumed that dry land (negative depth values) do participate in the housing of shorebirds.

Evaluation will be done by determination of the MI- (Mud-Island) ratio:

$$MI = \frac{A_{mudflat}}{A_{island}} \tag{5.1}$$

where $A_{mudflat}$ is the mudflat growth relative to the initial mudflat area (km^2) and A_{island} is the total island surface area implemented (km^2). A high MI-ratio will indicate high mudflat expansion while minimum island area is implemented.

5.2 Island configuration

In this section the island configuration results are explained, shown and further elaborated. The Basic series is treated first, followed by the Exploratory series.

5.2.1 Basic design

The Basic series consist of a clear systematic approach in which the barrier island concept is elaborated. The Netherlands is well known regarding barrier islands which span in the north. These barrier islands can reach up to 27 km in length. The width of the islands ranges from 1 - 10 km and furthermore inlet width ranges from 0.8 - 6 km. The length of the Wadden Sea Islands are strongly linked to the local tidal range. The tidal range increases in east direction for which the length of islands decreases (Roos et al., 2013). The island designs are partially based on the Wadden Sea Islands. Within the Basic island series the island length and inlet widths are deducted from the Wadden Sea and varied for two values each. The islands widths are however set smaller than seen in the Wadden Sea. The influence of the tidal range on island length has not been considered within the Basic series.

Two main types can be distinguished, in general denoted as two-two and three-three concepts, meaning two or three islands along the NAYRD and SAYRD respectively. An overview of the parameter settings can be seen in Table 5.1.

The models results are elaborated in Table 5.2 and can be seen in Figures 5.1, 5.2, 5.3, 5.4. The production simulation as described in Section 4.3, shows 45.02 km^2 of new mudflat area after ten years. The 0.88 m depth contour has shown significant seaward extension at the river mouth situated in NAYRD. Furthermore, slight seaward extension is shown along the SAYRD coastline with most observed just south of Binhai Port. The results from the production simulation without the implementation can be seen in Appendix C.1.
From the results it can be concluded that the largest increase in mudflat area is established by configuration N5+S5. The highest MI-ratio is acquired by N5+S5. This induces the largest realisation of mudflat area by implementing the least island area. However, it can be noticed that this island configuration uses the largest amount of island area. The design is elaborated in more detail in Section 5.3.
All island configuration are illustrated in Appendix C.2 in which the contours of the initial mudflat and the newly obtained mudflat are illustrated. The mudflat contour of the reference simulation after ten years is illustrated as well, in order to gain a better understanding of the effectiveness of islands.

Basic Configuration	Islands (-)	Island length (km)	Island width (km)	Inlet width (km)	Depth contour (m)
N1+S1	3 - 3	10	0.3	2.5	7 - 8
N2+S2	3 - 3	10	0.3	5	7 - 8
N3+S3	3 - 3	10	0.3	2.5	4 - 5
N4+S4	3 - 3	10	0.3	5	4 - 5
N5+S5	2 - 2	15	0.3	2.5	7 - 8
N6+S6	2 - 2	15	0.3	5	7 - 8
N7+S7	2 - 2	15	0.3	2.5	4 - 5
N8+S8	2 - 2	15	0.3	5	4 - 5

Table 5.1: The parameter set-up regarding the Basic series

Simulation results	Increase (km^2) relative to reference	Increase (km^2) relative to initial	Total mudflat (km^2)	Islands (km^2)	MI - ratio (-)
Reference	-	44.46	197.46	-	-
N1+S1	26.82	71.28	268.74	14.58	1.84
N2+S2	17.28	61.74	259.20	12.78	1.35
N3+S3	48.60	93.06	290.52	14.58	3.33
N4+S4	32.85	77.31	274.77	12.78	2.57
N5+S5	59.76	104.22	301.680	16.02	3.73
N6+S6	49.77	94.23	291.69	15.03	3.31
N7+S7	50.31	94.77	292.23	16.02	3.14
N8+S8	44.10	88.56	286.02	15.03	2.93

Table 5.2: Basic design results after ten morphological years

Within Appendix C.3 a quantitative analysis is elaborated on the morphological development differences between the NAYRD and SAYRD. Within the Basic series the NAYRD is denoted as 'N', while the SAYRD is denoted as 'S'. The division between the NAYRD and SAYRD is set at Binhai Port. The results of the NAYRD are shown in Table C.2, whereas the results of the SAYRD are shown in Table C.3.
From the results it can be seen that the NAYRD shows larger MI-ratio's. The island configurations are equal on both sides of the AYRD. Hence, it can be concluded that the islands on the NAYRD are more effective in mudflat formation. The effect may be due to the smaller bed slope in the NAYRD, for which the mudflat definition is earlier reached than at larger depths.

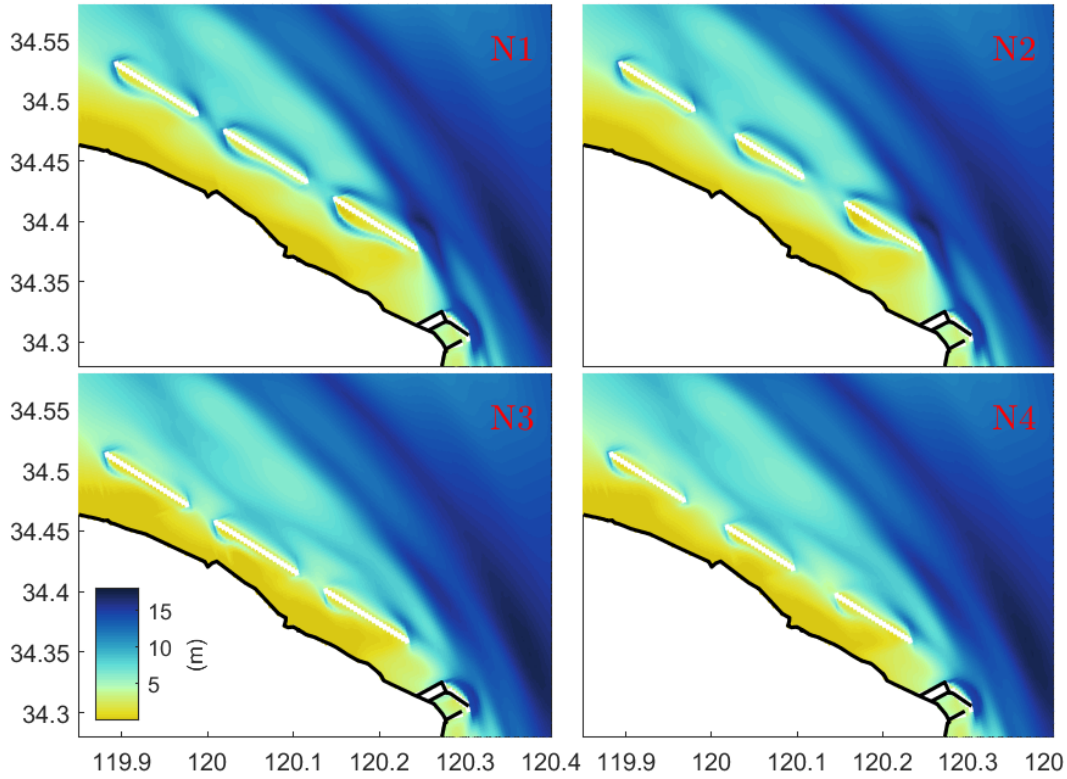

Figure 5.1: Basic series. Small islands at the Northern Abandoned Yellow River Delta. The results comprehend a ten year morphological development

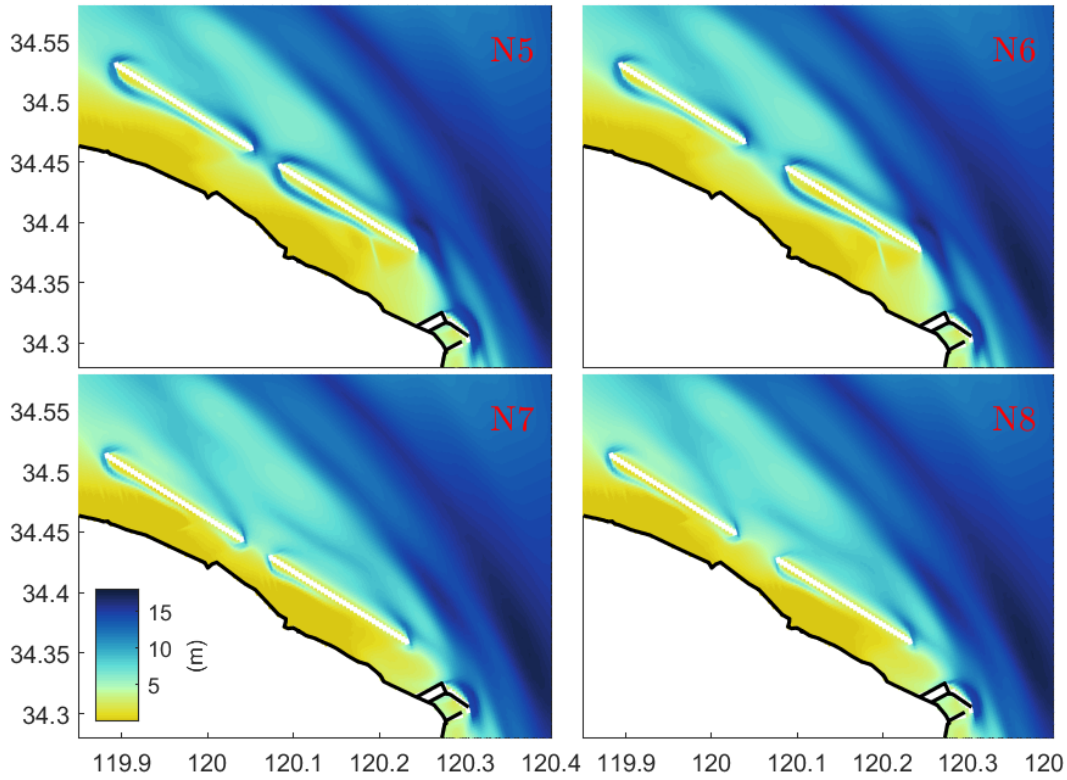

Figure 5.2: Basic series. Large Islands at the Northern Abandoned Yellow River Delta. The results comprehend a ten year morphological development

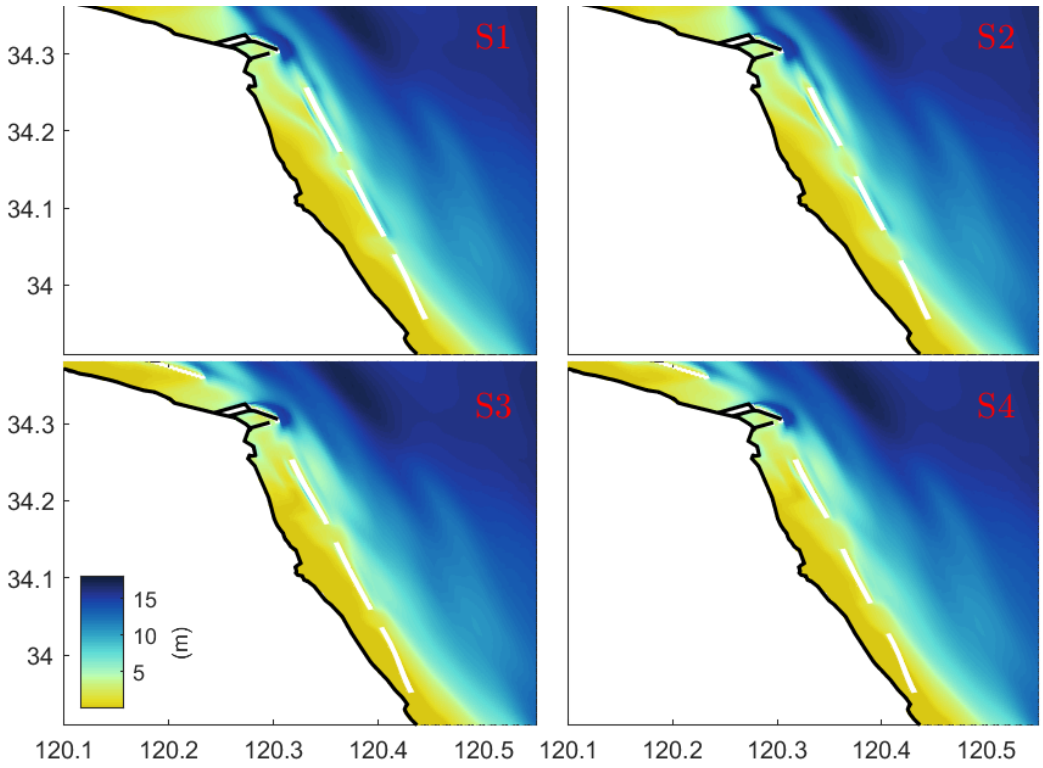

Figure 5.3: Basic series. Small islands at the southern Abandoned Yellow River Delta. The results comprehend a ten year morphological development

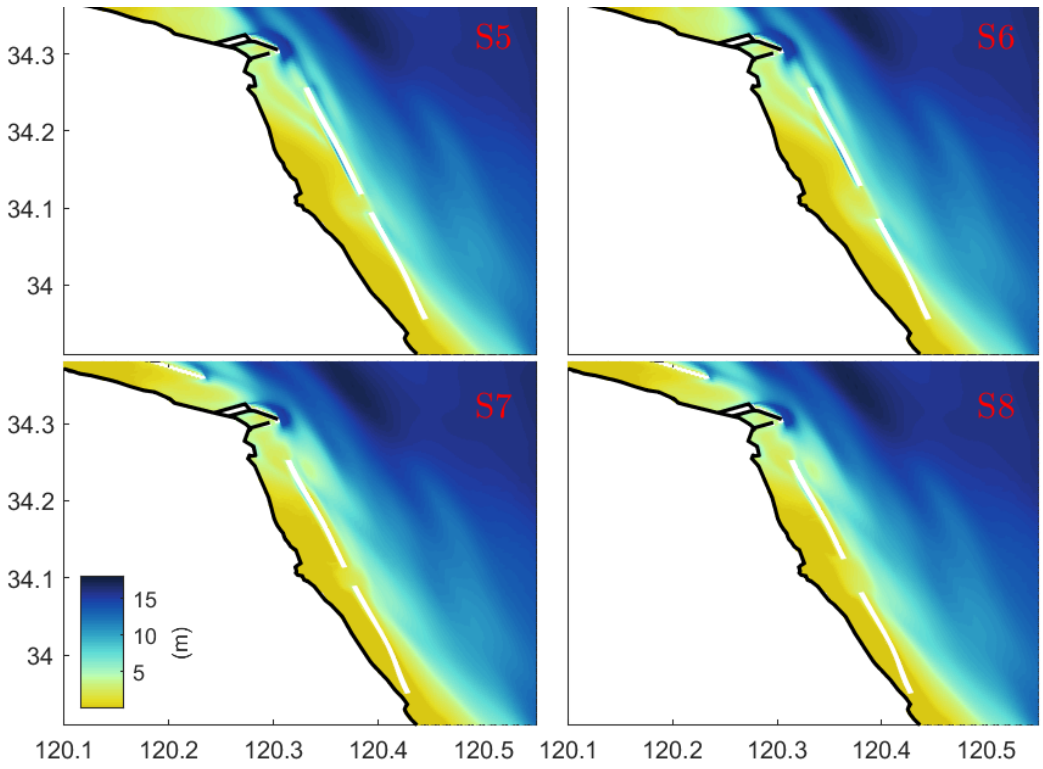

Figure 5.4: Basic series. Large Islands at the southern Abandoned Yellow River Delta. The results comprehend a ten year morphological development

5.2.2 Exploratory design

The Exploratory series comprehend seven designs based on observed sediment transport mechanisms. The mean suspended sediment transport (depth-averaged) is directed south. This suggests the trapping of sediments at the southern ends, NAYRD and SAYRD respectively. The trapping of sediment enhances sediment accumulation alongshore over time. Groynes perpendicular to shore will however not attenuate waves. Hence, it is suggested to implement islands which will attenuate waves. The shoal in the northern NAYRD shows natural accretion. From a 'Building with Nature' perspective it might be interesting to stimulate island growth at that specific area. The shoal will naturally attenuate waves and therefore protect the NAYRD.

The models results are elaborated in Table 5.3 and can be seen in Figures 5.5, 5.6, 5.6, 5.8.
In general, it can be observed that the relative mudflat area increase is significant lower in comparison with the Basic series. The total island surface area is again significant lower. Direct comparison between the two series is possible through the MI-ratio, concluding that these islands configurations have significant less effect on mudflat growth. The best island configuration regarding the MI-ratio is G6+V6. The islands are implemented at approximately seven to eight meter depth contour. The most mudflat development is found at the SAYRD behind the longest island. The southern most island is set as a groyne, however has little effect on sediment accumulation. The shallow area where it is implemented might be the reason. The island which is attached to Binhai Port induces siltation at both sides. The siltation occurring seaward ensures breakwater stability and is limited in growth due to the strong tidal currents. The larger islands in the NAYRD induce significant siltation. The middle island reduces wave penetration, however does not affect mudflat growth to a large extent.
All island configurations are illustrated in Appendix C.4 in which the contours of the initial mudflat and the newly obtained mudflat are illustrated. The mudflat contour of the reference simulation after ten years is illustrated as well in order to gain a better understanding of the effectiveness of islands.

Simulation results	Increase (km^2) relative to reference	Increase (km^2) relative to initial	Total mudflat (km^2)	Islands (km^2)	MI - ratio (-)
Reference	-	44.46	197.46	-	-
G1+V1	0.81	45.27	242.73	6.48	0.13
G2+V2	12.78	57.24	254.70	9.45	1.35
G3+V3	10.53	54.99	252.45	8.64	1.22
G4+V4	10.53	54.99	252.45	9.90	1.06
G5+V5	6.39	50.85	248.31	8.37	0.76
G6+V6	12.69	57.15	254.61	8.82	1.44
G7+V7	18.00	62.46	259.92	13.32	1.35

Table 5.3: Exploratory design results after ten morphological years

Within Appendix C.5 a quantitative analysis is elaborated on the morphological development differences between the NAYRD and SAYRD. Within the Exploratory series the NAYRD is denoted as 'G', while the SAYRD is denoted as 'V'. The division between the NAYRD and SAYRD is set at Binhai Port. The results of the NAYRD are shown in Table C.4, whereas the results of the SAYRD are shown in Table C.5.
It must be noted that the island configurations are not equal on both sides of the AYRD. The

residual sediment transport is directed south, hence some dependency should be expected between the NAYRD and SAYRD. Preliminary results did not show a correlation when sediment was retained in the NAYRD. The effect is probably due to the abundant sediment supply originating from Binhai Port. In general, larger MI-ratio's are seen in the SAYRD from which V3 is highest (0.78) and followed by V6 (0.78). G6 shows however the largest MI-ratio within the NAYRD, followed by G2 (0.59).

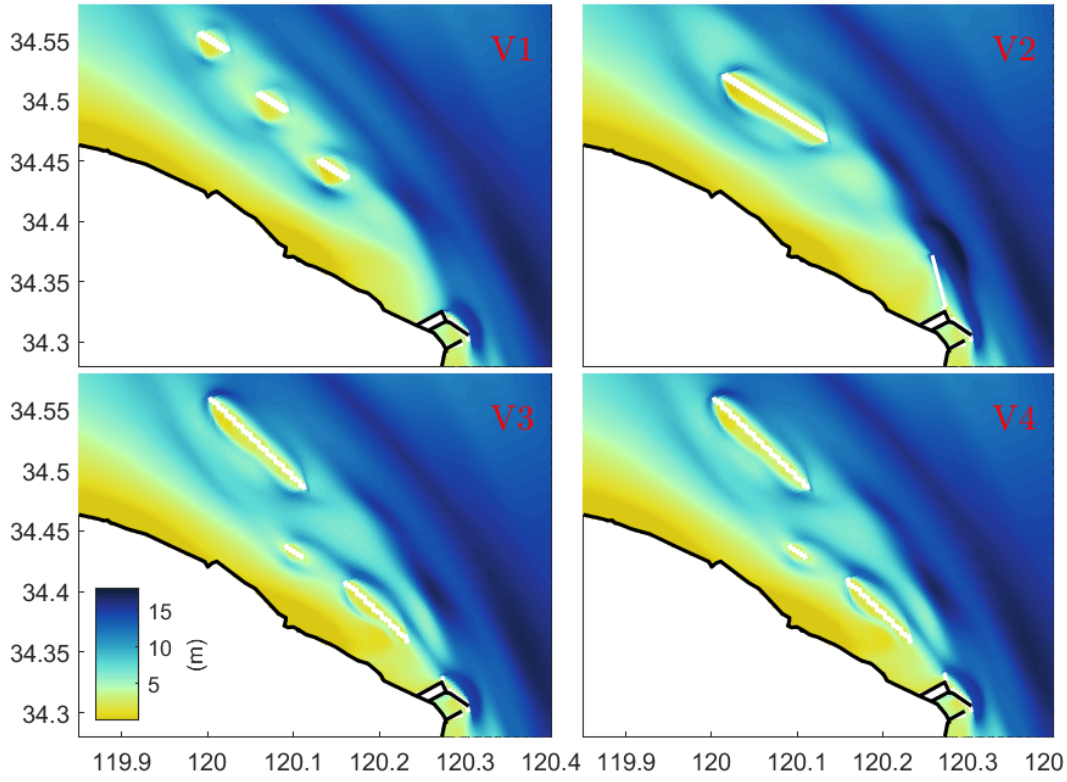

Figure 5.5: Exploratory series. Small Islands at the northern Abandoned Yellow River Delta. The results comprehend a ten year morphological development

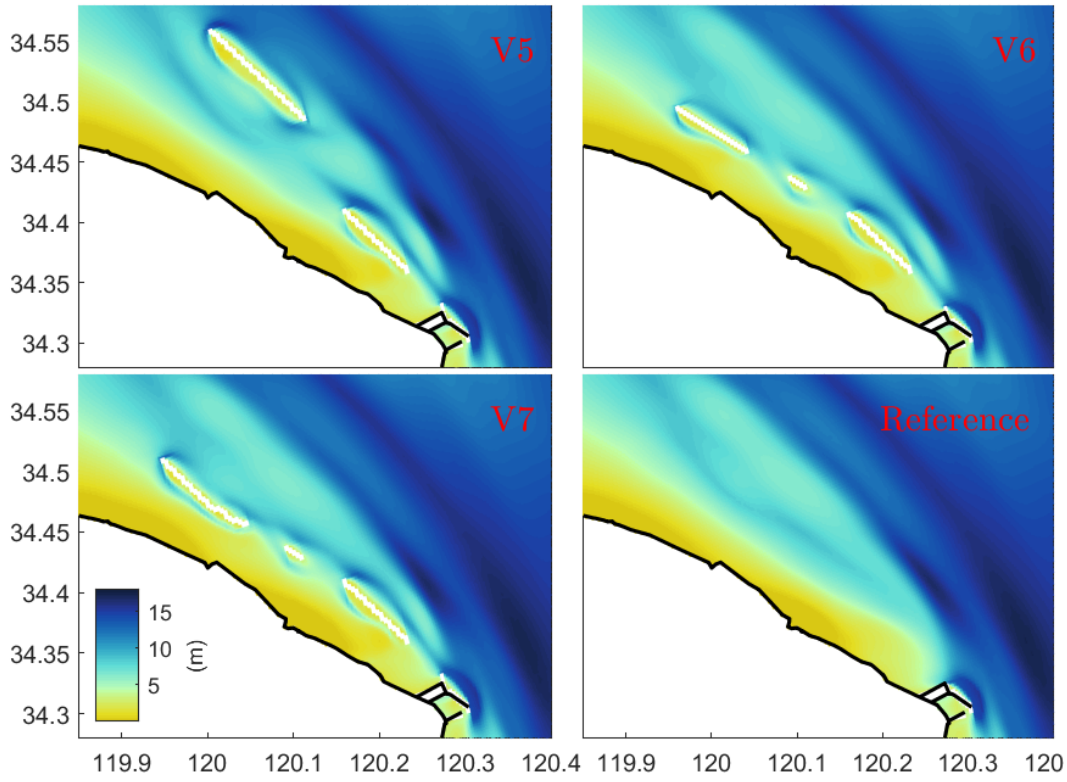

Figure 5.6: Exploratory series. Large Islands at the northern Abandoned Yellow River Delta. The results comprehend a ten year morphological development

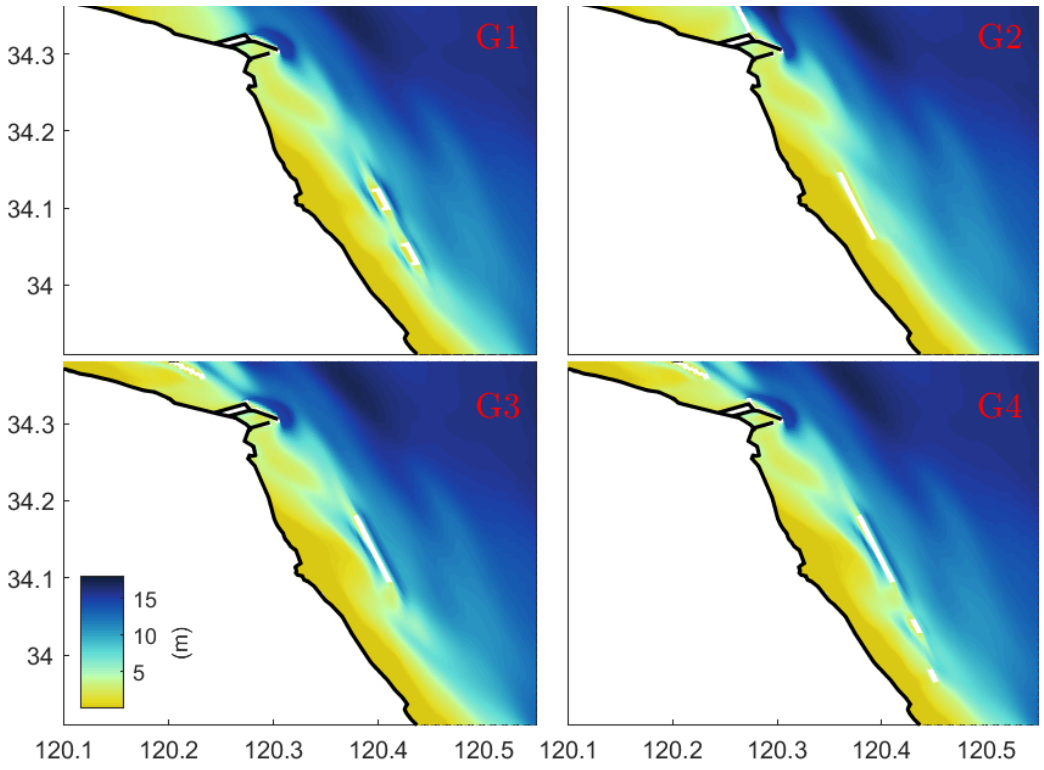

Figure 5.7: Exploratory series. Small Islands at the southern Abandoned Yellow River Delta. The results comprehend a ten year morphological development

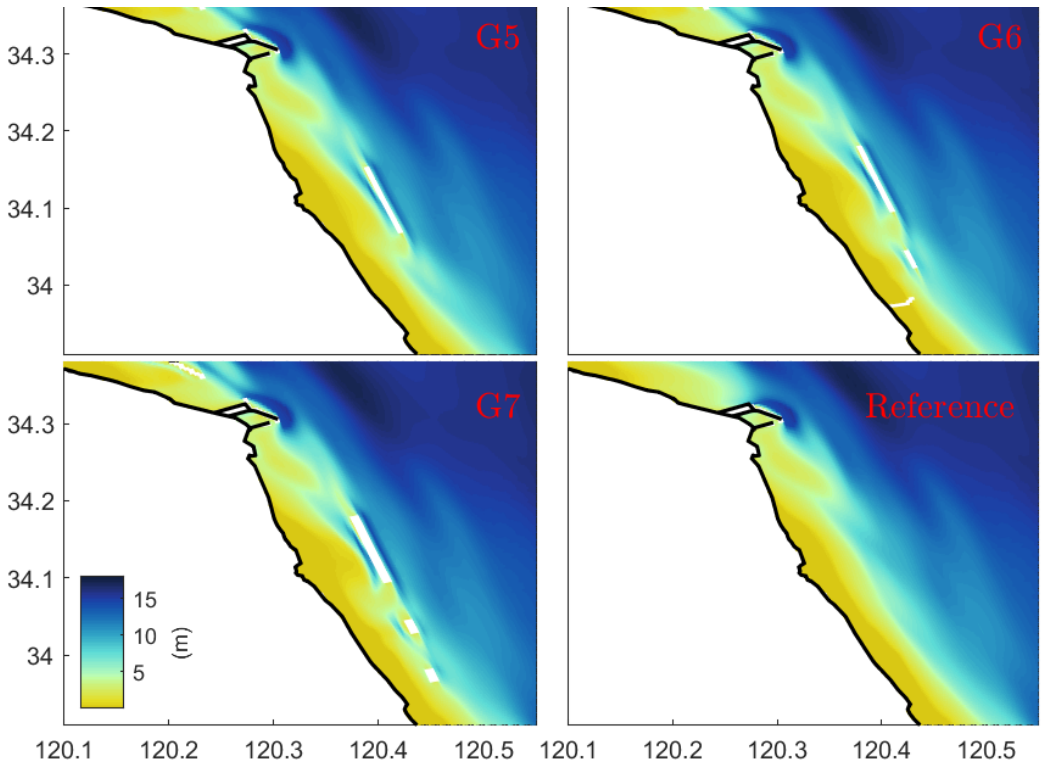

Figure 5.8: Exploratory series. Large Islands at the southern Abandoned Yellow River Delta. The results comprehend a ten year morphological development

5.3 Optimal design

The N5+S5 island configuration induces the largest mudflat area growth and shoreline protection. After ten morphological years the design induces a mudflat growth of 59.76 km^2 relative to the reference production simulation by implementing 16.02 km^2 of islands. The concerning island configuration has been designated as the optimal island configuration within this research.

The island configuration in question contains four islands with lengths of 15 km each. These islands are approximately implemented at the 7 - 8 m depth contour at the NAYRD and SAYRD. The NAYRD shows the presence of several distinct channels, which are less obviously present in the SAYRD. The latter may be explained by the steep bed slope at the SAYRD (see Figure 4.16). Figure 5.9 shows the model results after ten years including the contours of the newly developed mudflat, the initial mudflat and the mudflat contour of the reference simulation result. The mudflat contour in the NAYRD deflects to the south-east as these approach the islands. This effect is due to the flood dominant character of the coast, which is south-east directed in the NAYRD. The 15 km length islands let the flow pass by over similar length in shallow water. Large friction is observed here and therefore smaller tidal velocities are seen behind the islands over distance. Deep water is present seaward of the islands which allows faster tidal movement due to less friction. Hence, large tidal velocities are observed around the islands ends as these catch up the delayed flow. As such, clear channels are seen around the island ends.
The waves are blocked by the islands and can only penetrate through the inlets. These inlet widths are small and thus little wave penetration occurs. The relatively long islands cover large parts of the AYRD coast, hence significant area is protected from erosion.

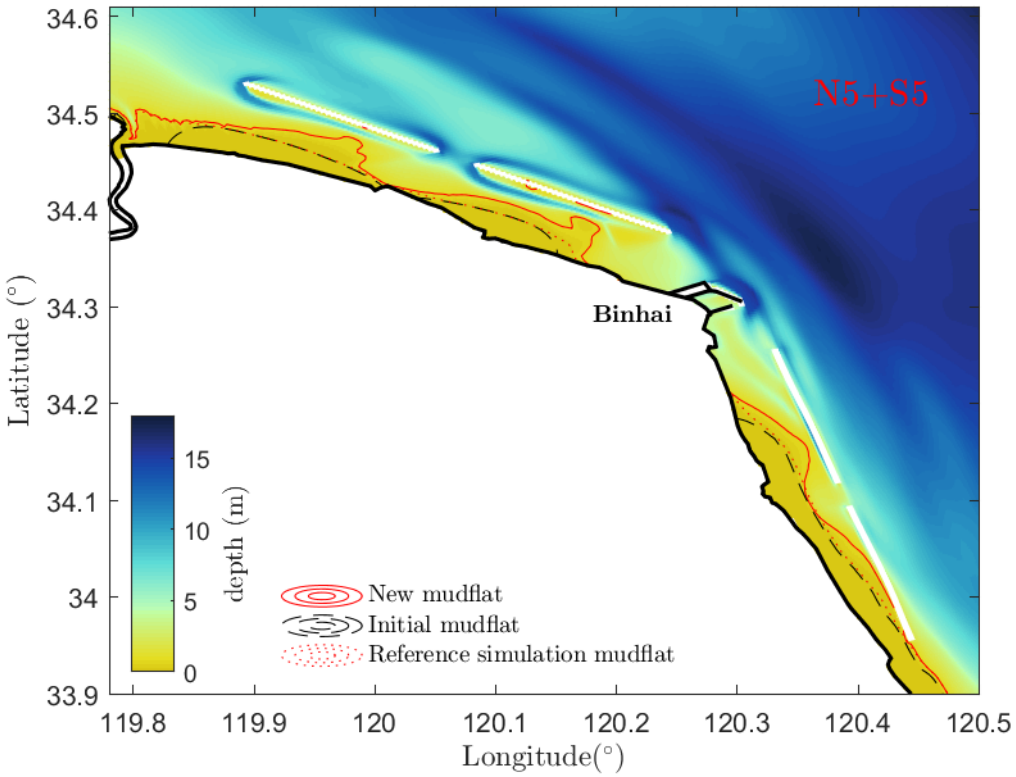

Figure 5.9: N5+S5 simulation after ten morphological years: initial- and newly developed mudflat

Figure 5.10 shows an overview of the erosion and siltation patterns in both the reference simulation (left) and the island configuration N5+S5 (right).
The reference simulation shows slight siltation patterns in the NAYRD, however an erosional trend is observed in general. The islands induce strong siltation. The deflection to the south-east is clearly visible behind these islands. The mechanism can be traced to the mean current velocity (depth-averaged). The current magnitude decreases towards the south-east ends of the islands, which is shown in Figure 5.11. Furthermore, the channel formation behind the northern island near Binhai Port can be clearly observed.
The reference simulation shows a siltation trend in the SAYRD. As discussed earlier, the significant siltation here may be due to the significant erosion at Binhai Port. Hence, these sediments were entrained and deposited further south. Literature pointed an erosional trend, which is not clearly visible within the model results. The implementation of islands show strong siltation and protection of the entire coast. The current is exactly parallel to the islands, hence the magnitude of the velocity is small at the islands ends for which siltation is observed.

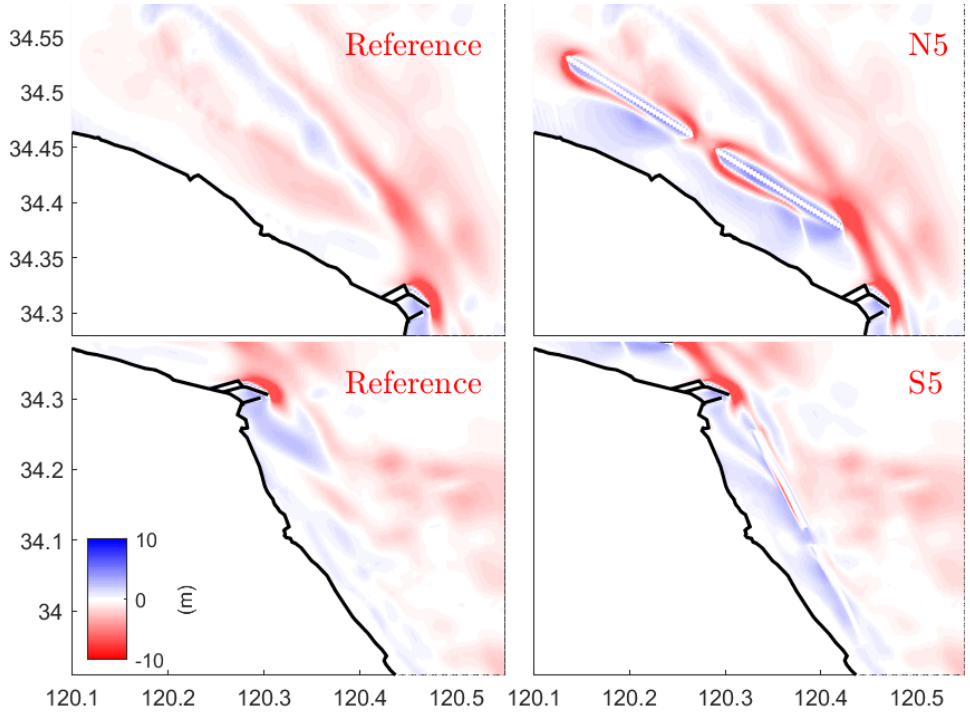

Figure 5.10: Comparison siltation (blue) and erosion (red) patterns; reference- (left) and island configuration (right) after ten morphological years

An additional simulation has been set in determination of the mean current velocity (depth-averaged) for island configuration N5+S5. The simulation has been set-up from 15/05/07 - 17/06/06, considering a four consecutive spring - neap tidal cycle on an hourly interval. The results are shown in Figure 5.11. The NAYRD shows a decreasing mean current velocity south-eastward, which is believed to be the main cause of the occurring siltation pattern. The decrease in current velocity induces a decrease in transport capacity and then siltation features might be present. The latter is observed in Figure 5.10. The Binhai Port induces an eddy, which is clearly visible just south of the port. The SAYRD does not show any irregularities due to the parallel flow along the islands.

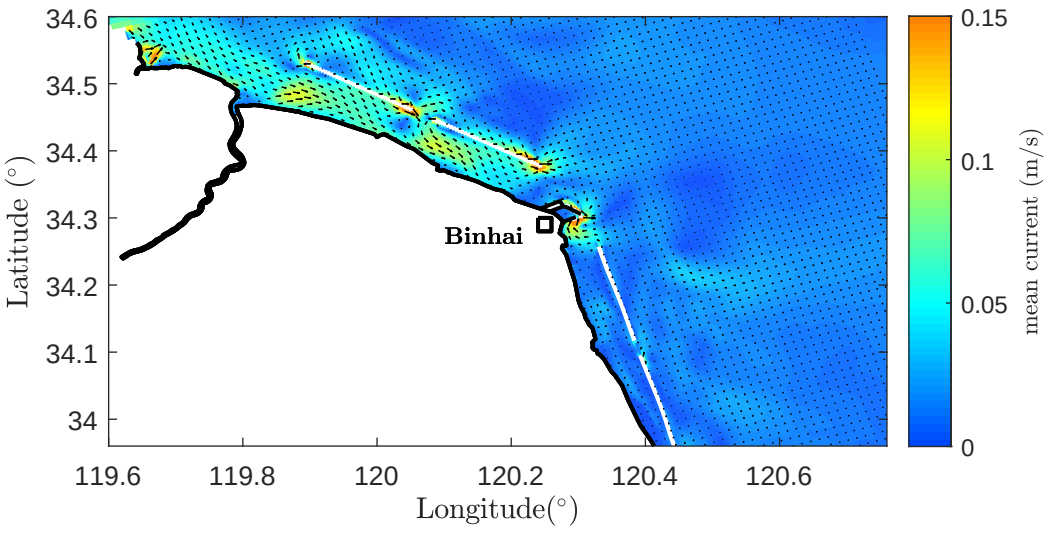

Figure 5.11: Mean tidal current (depth-averaged) observed for island configuration N5+S5

6 Discussion

A good understanding has been gained by extensive literature review and data analysis. The model used within this research originates from Yao (2016) and has been further modified. These modifications have effect on the overall results, which is upon reflected and further elaborated in this chapter.

6.1 Hydrodynamic forcing and suspended sediment

During the start-up of this thesis it was observed that the locations of the measurement stations were not overlapped by the original grid as set by Yao (2016). Aside the refinement of the original grid, additional grid extension had to be done in order to connect with the updated land boundary. Further detailed elaboration on the grid extension can be found in Appendix B.1.2. The bathymetry of the newly added grid was yet to be determined, which has been done by extensive calibration. The results shown in Section 4.1.1 show good resemblance regarding water levels, however deviation in the magnitude of the current velocities is observed (Figure 4.4). These deviations are significant with respect to the ebb-tidal velocities and thus in transport capacity. Therefore, the sediment transport northward is slightly underestimated within the model.

The bathymetry has been extensively calibrated for the extended grid. The results were shown in Figure 4.1. A 2016 survey has been made available for this research. The survey covers the AYRD partially and includes Binhai Port. Due to presence of the port and large abrupt depth differences at the transitions, it was decided to validate the model for the original bathymetry. The implementation of the 2016 survey is shown in Figure 6.1. The calibrated bathymetry has been validated by literature. It could be concluded for stations B, D and F that these were approximately correct. The bathymetry of stations A, C and E were approximately somewhat too deep. A smaller bed slope is needed and therefore the grid should be refined to a larger extent. The latter is however not attainable regarding the relatively large model domain and computational limitations.

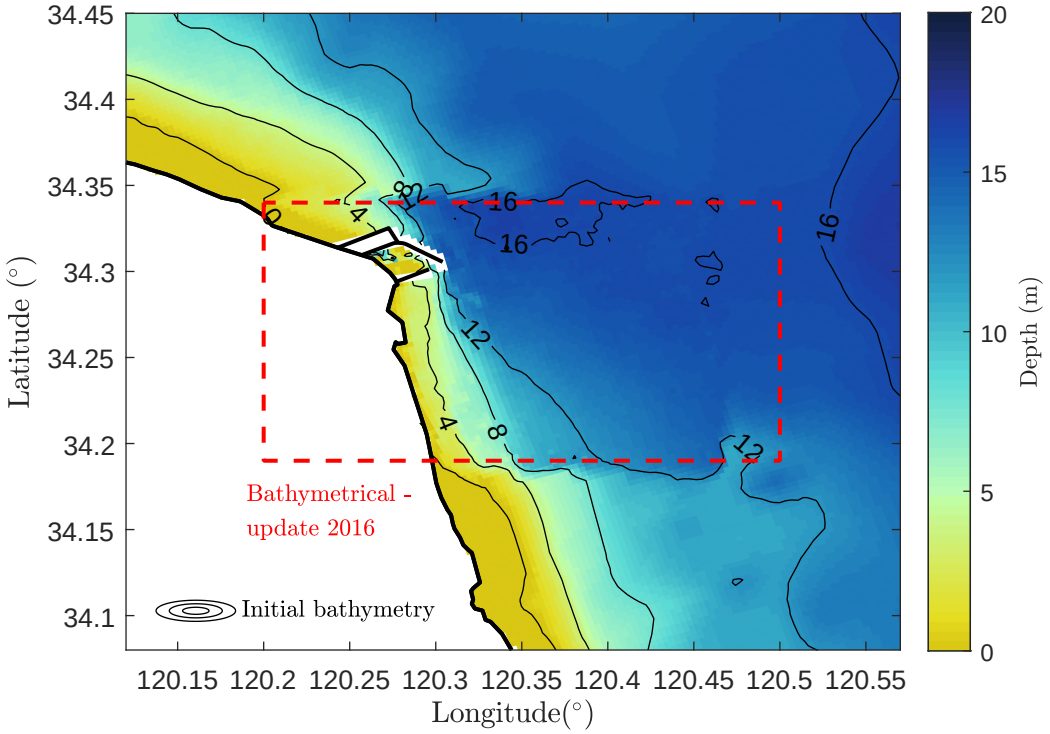

Figure 6.1: Update bathymetry from 2016 survey - not used within this research

6.2 Wave inclusion

Within this research waves have been included. The boundary conditions were set-up by implementing an adjusted time-series on the two open boundaries of the JRM. The dataset comprehends a one-year measurement time-series conducted at Xiangshui station (Figure 4.1). The results are visualised by means of a wave rose shown in Figure 6.2. The conducted measurements show the presence of waves directed from the north-west, which can only be induced by local winds. Wind is however not taken into account within this research due to the lack of data. The dataset has been calibrated in a pragmatic way, which deemed to be sufficient regarding the exploratory motive. More on the calibration of waves can be found in Appendix B.3.1.

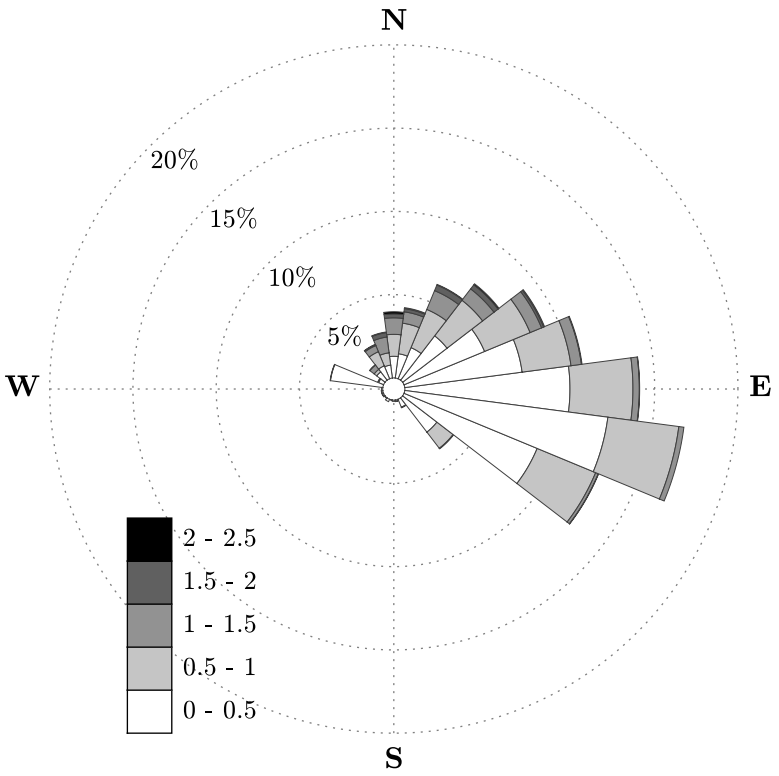

Figure 6.2: Wave rose of measured waves at Xiangshui station. The directional rose shows the frequency of incoming waves from multiple directions

The dataset has been filtered for wave directions ranging between 30° - 180°. The filtered wave data without further modifications, has been visualised as a wave rose on the measurement location. The result is shown in Figure 6.4. The wave data has been calibrated accordingly to Appendix B.3.1 and implemented onto the wave grids its boundaries. The reference simulation, comprehending ten year morphological development, predicts waves as shown in Figure 6.3.

In general, it can be observed that the model under-predicts the waves from the south-east. Furthermore, the frequency of occurrence for large wave heights do not correspond either. The effect of the under-predictions from the south-east, will have effect on the sediment transport. Hence, it may be concluded that the wave-induced sediment transport in north-west direction is under-estimated within the model.

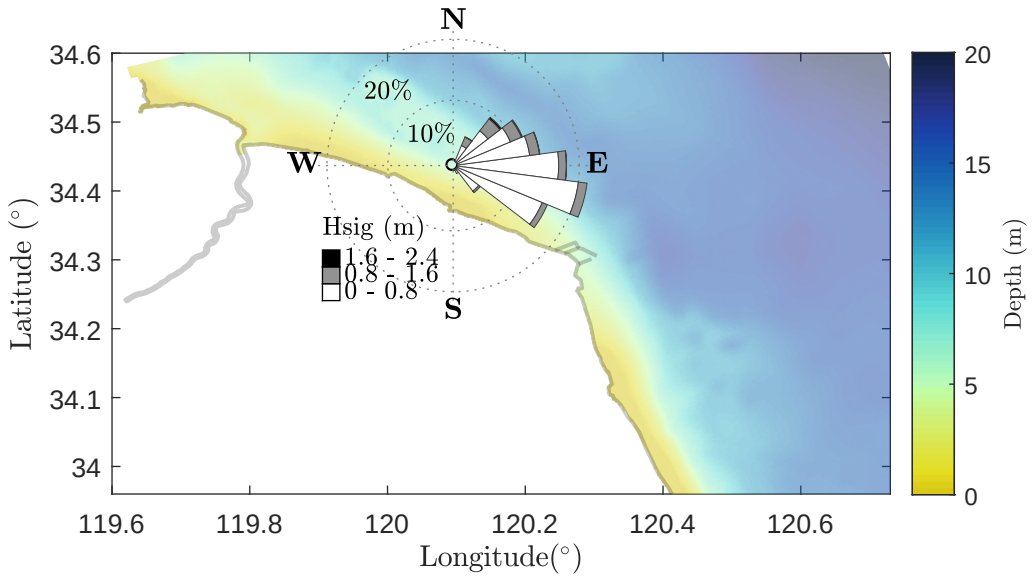

Figure 6.3: Visual representation of wave measurement at Xiangshui station after filtering for wave directions between 30° - 180°

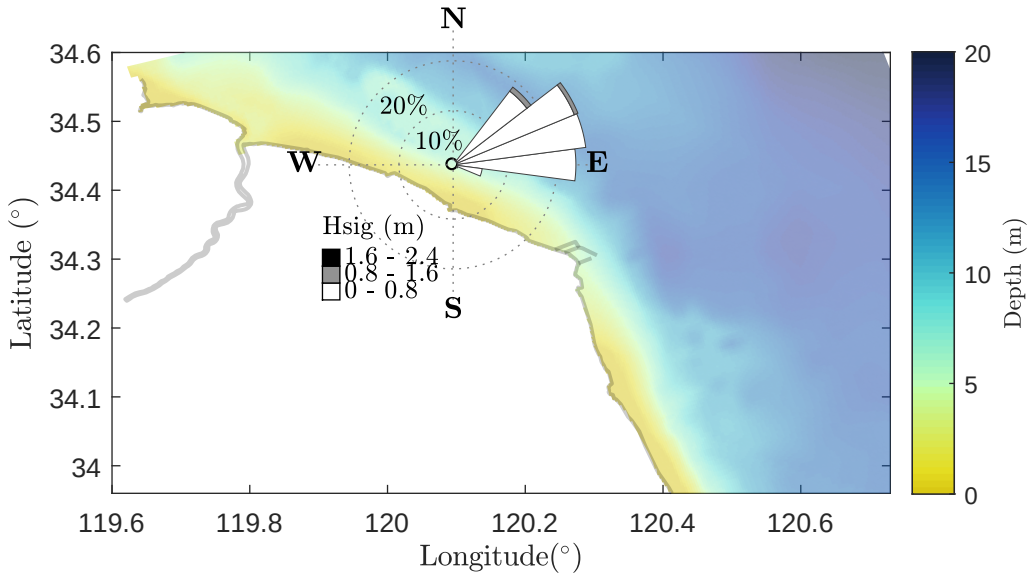

Figure 6.4: Visual representation of wave model results at Xiangshui station

6.3 Sorting of bed sediments

The morphological development after ten years is further investigated for both forcing scenario's. The siltation - erosion pattern along the AYRD induces sorting of bed sediments. Hence, the bed composition is looked into in order to gain a better understanding of the siltation process. The initial bed composition is set with 3.4 m thickness for both the 16 μm and 90 μm fraction. The cohesive fraction has been set with a 0.2 m initial bed thickness. Hence, an average grain size of approximately 51.48 μm is set as for the initial bed composition. After ten morphological years the bed composition has been examined of the top sub-layer. The results are shown in Figure 6.5 for tidal forcing only. The depositional areas show the presence of mainly fine sediment. The results of the inclusion of waves can be seen in Figure 6.6. The addition of waves have significant influence on the average grain size. Under tidal forcing only the average grain size ranges between 16 - 26 μm at depositional areas. The addition of waves induce sediment stirring and displacement at these regions. Hence, the average grain sizes increases to 42 - 52 μm.

6.4 Results Island configuration

The island configuration judgment is mainly based on mudflat growth within the Abandoned Yellow River Delta area. The mudflat definition is set to the MLW at Xiangshui station, from 0.88 m to -∞ (positive depths are considered). The disadvantage of a single value definition in a spatial varying tidal range, induces an under-estimation of the intertidal mudflat area. If a more detailed approximation is favoured, then it is advised to calculate the MLW of all individual cells.

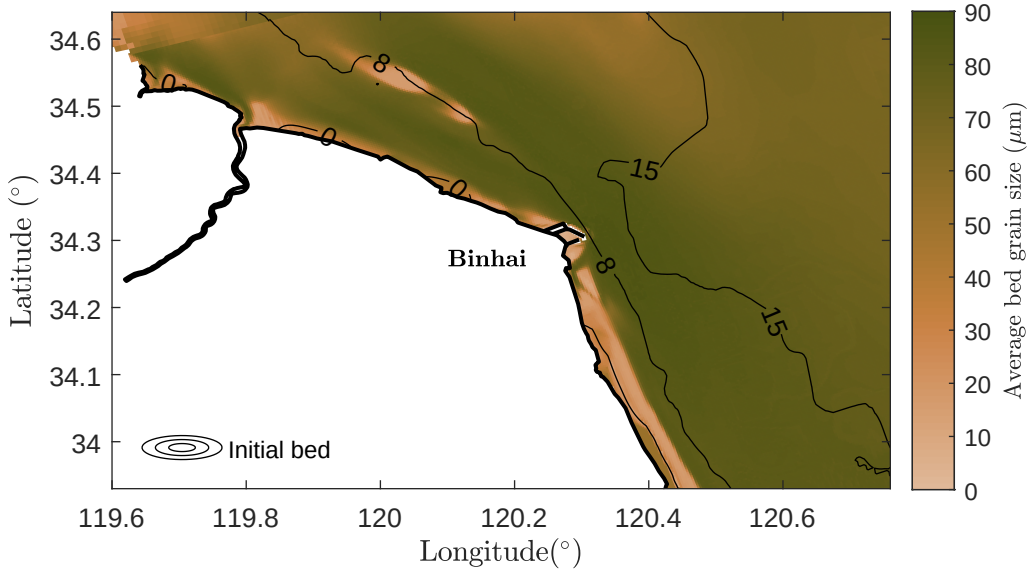

Figure 6.5: Average grain size found in the top layer after ten morphological years. Wave forcing has not been applied

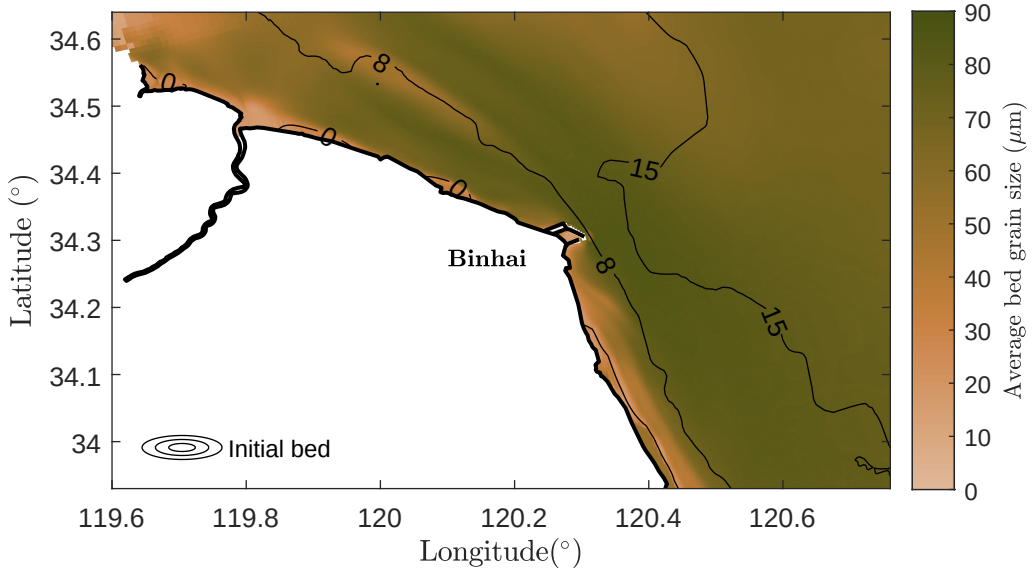

Figure 6.6: Average grain size found in the top layer after ten morphological years. Including wave forcing

7 Conclusion

The final conclusion will be drawn within this chapter. In order to do so, the main- and sub questions will be mentioned again.

7.1 Conclusion

What are the governing processes for flow and sediment transport at the Abandoned Yellow River Delta?

After extensive literature review a good understanding has been gained of the driving processes along the Abandoned Yellow River Delta. However, the use of the Jiangsu Regional Model (Yao, 2016) has given the opportunity to further investigate the driving processes in more detail. Within this research the hydrodynamic forcing has been expanded. Aside tidal forcing, waves were included in order to better represent the hydrodynamics along the AYRD.
The model validation process showed good results in water level and direction. The current velocities showed however little deviations. The ebb tidal velocities were under-estimated by the model, whereas the flood tidal velocities show good resemblance. The flood dominant environment enhances southward transport of sediment, which is clearly visible in the mean suspended sediment transport. Residual currents are found to be southward directed along the Northern Abandoned Yellow River Delta and mostly offshore in the shallows nearshore.
The dominant tidal forcing has large influence in the overall erosion and siltation patterns along the AYRD. The inclusion of Binhai Port causes flow contraction around the breakwater. Hence, local current velocities are increased and sediment is entrained herewith. The largest erosion is observed here. Large siltation is seen just south of Binhai Port due to the lower current velocities and hence transport capacity.
Waves have shown of great importance in the stirring- and transport of sediment. The inclusion of waves resulted in an additive $2.2{\cdot}10^7$ ton/year residual transport going out the AYRDM model domain. The overall reference simulations of tide-only and wave-current forcing show large differences. The tide-only results showed significant siltation at the northern shoal and at the SAYRD coast. These siltation patterns were completely smoothed due to cross-shore transport. Furthermore, the inclusion of waves increased the mean grain size from 16 - 26 μm to 42 - 52 μm at these siltation areas.

Secondary flow has contributed significant to siltation along the islands. More siltation is seen in the NAYRD than in the SAYRD, due to the distinctive angle of incidence of the islands within the flow field. The current divergence around the island ends causes local water level differences through which streaming occurs. This streaming, which is called secondary flow, induces sediment transport towards the islands.

What is the impact of large-scale islands on the hydrodynamic- and morphological dynamics?

The implementation of large-scale islands have significant effect on the flow field along the Abandoned Yellow River Delta. The islands are abrupt barriers implemented within a near morphological equilibrium state. The flow is diverged around the islands ends and induce rapids due to flow contraction. The increased velocity induces sediment transport and hence erosion. As a result, tidal channels are formed around the island ends. The flow's disability to abruptly adjust in direction causes local water level differences behind the islands ends. Hence, secondary flow is induced forming an eddy-type current. The secondary flow initiates sediment transport towards the islands, which settle when current velocities are small enough.
Multiple islands are implemented in the suggested configurations. Due to their large length, significant disturbances are applied along the AYRD coast. These disturbances are visible in the modelling results. However, these have positive effect on overall siltation patterns along the AYRD.

Which configuration of islands is favourable?

In order to suggest favourable island configuration, it is of importance to understand the impact of each individual configuration.
In general, it is noticed that for larger island lengths, the mean current becomes smaller near the southern island ends. The shallows induce larger friction on tidal movement for which current velocities and herewith transport capacity is reduced over distance. Hence, depositional areas are found to be radially deflected to the south. The relative short islands do not induce current velocities to lessen significantly. Hence, less siltation is observed.
The distance relative to shore is important in the intensity of diverging flow. The tidal currents are stronger further offshore, which increases the length behind the island for the flow to adjust. Therefore, a larger eddy is created behind the islands ends for which larger siltation patterns are observed. Another feature is the angle of incidence of the islands on the flow pattern which may induce secondary flow.
Furthermore, the inlet width is adjusted for the near- and offshore islands. It can be concluded that smaller inlet widths induce more local erosion due to the high flow contraction and hence increase of the current velocity.
The most favourable design configuration comprehend elongated islands with relatively large lengths. The distance between the islands and the shoreline can be as large as possible for small bed slopes, since the current will be slowed down by the shallows. As a result, the transport capacity of the flow is reduced for which siltation occurs. The islands ends can be designed with somewhat extra width or the island's angle of incidence on the flow field can be adjusted for which secondary flow occurs. The secondary flow induces sediment transport towards the islands, through which these naturally enlarge. In order to increase siltation along the AYRD

inlet widths need to be kept small. The most favourable configuration in this thesis is N5+S5. After ten morphological years the design induces 59.76 km^2 of mudflat growth relative to the reference production simulation by implementing 16.02 km^2 of islands.

Could large-scale Islands enhance coastal protection and encourage the development of large-scale tidal mudflats along the Abandoned Yellow River Delta?

Large-scale islands are an effective measure in encountering the erosive features found along the Abandoned Yellow River Delta. The islands attenuate wave penetration and tidal flow in front of the delta. Significant siltation is induced subsequently for which expansion of the mudflat area has been observed. The acquired foreland is providing in additional coastal safety and hence decreasing the pressure on existing sea defence structures. The latter will reduce maintenance works and future extension (e.g. due to sea level rise).
The implementation of islands increases ecological value and may induce socio-economic benefits. The developed mudflat area is part of the East Asian–Australasian Flyway and hence may serve as roosting- and nourishing sites for multiple (endangered) shorebirds. The shallows will increase habitat for multiple fish and biodiversity in general. Local fisheries can take advantage and eco-tourism may be exploited.
It can be concluded that the islands increase coastal safety by mudflat development and furthermore ecological value of the local environment.

7.2 Recommendations

The conclusions give raise to certain recommendations for further research. The recommendations are elaborated within this section.

The first recommendation is to improve the calibration of waves including wind. The effect of wind has turned to be of significant importance in such a large model domain.

The AYRDM is nested within the JRM. Due to the overall size of the JRM, herewith included processes and multi-fraction approach, large amount of computational time is necessary in order to perform the simulations. Within this research it is tried to minimise computational time by reducing sediment fractions after careful selection. However, when more fractions need to be included and/or more processes, the model is somewhat inefficient. An efficient model would lead to less computational time which is highly favourable.

The JRM does not include the effect of large-scale currents which exist along the Jiangsu coast. Literature pointed northward sediment transport due to these seasonal varying coastal currents, which is now neglected.

The AYRD is major sediment supplier to the RSRF, since the residual sediment transport is directed south. The islands have proven to be effective in the trapping of sediment and hence less southward transport is expected. Further research needs to be done to what extend the islands will affect southward transport and consequently the Jiangsu coast.

Bibliography

Allen, J., Somerfield, P., and Gilbert, F. (2007). Quantifying uncertainty in high-resolution coupled hydrodynamic-ecosystem models. *Journal of Marine Systems*, 64(1):3 – 14. Contributions from Advances in Marine Ecosystem Modelling Research, 27-29 June, 2005, Plymouth, UK. 27

Bao, J. (2016). Jiangsu coastal salt making geography and changes of human-land relationship in the fifteenth to twentieth centuries. Fudan University Press, Shanghai. 1

Bao, J., Gao, S., and Ge, J. (2019a). Centralization and decentralization: Coastal management pattern changes since the late 19th century, Jiangsu Province, China. *Marine Policy*, 109:103705. 2, 4

Bao, J., Gao, S., and Ge, J. (2019b). Dynamic land use and its policy in response to environmental and social-economic changes in China: A case study of the Jiangsu coast (1750–2015). *Land Use Policy*, 82:169 – 180. 1, 2

Barter, M.A. (2002). Shorebirds of the Yellow Sea: Importance, threats and conservation status. *International Wader Studies 12, Canberra, Australia.*, 12. 4, 14

Battley, P., McCaffery, B., Rogers, D., Hong, J. S., Moores, N., Yung-Ki, J., Lewis, J., Piersma, T., and vd Kam, J. (2010). Invisible Connections: Why migrating shorebirds need the Yellow Sea . *The Wilson Journal of Ornithology*, 122:816–817. 14

Bennett, M. T., Gong, Y., and Scarpa, R. (2018). Hungry Birds and Angry Farmers: Using Choice Experiments to Assess "Eco-compensation" for Coastal Wetlands Protection in China. *Ecological Economic*, 154:71 – 87. 15

Binhai China Merchants Oganisation (2013). Jiangsu Binhai Economic Development Zone Coastal Industry Park. 2

BirdLife International (2018). Great news for shorebirds! China to halt coastal land reclamation. https://www.birdlife.org/worldwide/news/great-news-shorebirds-china-halt-coastal-land-reclamation.
4

Bouws, E. and Komen, G. (1983). On the Balance Between Growth and Dissipation in an Extreme Depth-Limited Wind-Sea in the Southern North Sea. *Journal of Physical Oceanography*, 13:1653–1658. 22

Chan, Y.-C., Peng, H.-B., Han, Y.-X., Chung, S.-H., Li, J., Zhang, L., and Piersma, T. (2019). Conserving unprotected important coastal habitats in the Yellow Sea: Shorebird occurrence, distribution and food resources at Lianyungang. *Global Ecology and Conservation*, 20. 14, 15

Chen, K., Zheng, J., Zhang, C., Nairui, W., and Zhou, C. (2016). The evolution characteristics of main waterways and their control mechanism in the radial sand ridges of the southern Yellow Sea. *Acta Oceanologica Sinica*, 36:91–98. 12

Chen, K., Zheng, J., Zhang, C., Wang, N., and Zhou, C. (2017). The evolution characteristics of main waterways and their control mechanism in the radial sand ridges of the southern Yellow Sea. *Acta Oceanologica Sinica*, 36(3):91–98. 9

Chen, K.-F., Wang, Y.-H., Lu, P.-D., and Zheng, J.-H. (2009). Effects of Coastline Changes on Tide System of Yellow Sea off Jiangsu Coast, China. *China Ocean Engineering*, 23:741–750. 12

China Daily (2018). Reclaiming land to be restricted. http://english.www.gov.cn/news/top-news/2018/01/18/content-281476017712430.htm. 4

Chu, Z., Sun, X., Zhai, S., and Xu, K. (2006). Changing pattern of accretion/erosion of the modern Yellow River (Huanghe) subaerial delta, China: Based on remote sensing images. *Marine Geology*, 227(1):13 – 30. 11

Cong, X., Wenjin, Z., Mingdong, L., Anguo, T., Jiangpei, G., and Xinxin, G. (2017). Research on the Influence of Reclamation on Water and Sediment Environment Offshore. *Journal of Water Resources and Ocean Science*, 6(4):55–60. 3

Cui, B., He, Q., Gu, B., Bai, J., and Liu, X. (2016). China's Coastal Wetlands: Understanding Environmental Changes and Human Impacts for Management and Conservation. *Wetlands*, 36. 3

Dai, Z., Liu, J., Wei, W., and Chen, J. (2014). Detection of the Three Gorges Dam influence on the Changjiang (Yangtze River) submerged delta. *Scientific Reports*, 4. 11

Dan, S., Walstra, D.-J., Stive, M., and Panin, N. (2011). Processes controlling the development of a river mouth spit. *Marine Geology*, 280(1):116 – 129. 17

de Vriend, H., van Koningsveld, M., and Aarninkhof, S. (2014). 'Building with nature': the new Dutch approach to coastal and river works. *Civil Engineering*, 167:18–24. 4, 48

de Vriend, H., van Koningsveld, M., Aarninkhof, S., de Vries, M., and Baptist, M. (2015). Sustainable hydraulic engineering through building with nature. *Journal of Hydro-environment Research*, 9(2):159 – 171. Special Issue on Environmental Hydraulics. 4

Deltares (2018). Delft3D-WAVE - User Manual - Simulation of short-crested waves with SWAN. Technical report, Deltares. 22, 24, 25, 101

Deltares (2019). Delft3D-FLOW User Manual. Technical Report 3.15. 17, 19, 21, 22, 25

Du, J., Shi, B., Li, J., and Wang, Y. P. (2019). Muddy Coast Off Jiangsu, China: Physical, Ecological, and Anthropogenic Processes. In Wang, X. H., editor, *Sediment Dynamics of Chinese Muddy Coasts and Estuaries*, chapter 3, pages 25 – 49. Academic Press. ix, 1, 2, 4, 8, 9, 11, 15, 23

Ecoshape (2020). Building with Nature Guidelines. https://www.ecoshape.org/nl/design-guidelines/. 48

Fredsoe, J. (1984). Turbulent Boundary Layer in Wave-current Motion. *Journal of Hydraulic Engineering*, 110:1103–1120. 18, 22

Gao, S. (2009). Modeling the preservation potential of tidal flat sedimentary records, Jiangsu coast, eastern China. *Continental Shelf Research*, 29(16):1927 – 1936. Special issue in honour of Michael Collins. 12

Gu, J., Luo, M., Zhang, X., Christakos, G., Agusti, S., Duarte, C. M., and Wu, J. (2018). Losses of salt marsh in China: Trends, threats and management. *Estuarine, Coastal and Shelf Science*, 214:98 – 109. 3

Hasselmann, K., Barnett, T., Bouws, E., Carlson, H., Cartwright, D., Enke, K., Ewing, J., Gienapp, H., Hasselmann, D., Kruseman, P., Meerburg, A., Muller, P., Olbers, D., Richter, K., Sell, W., and Walden, H. (1973). Measurements of wind-wave growth and swell decay during the joint north sea wave project (jonswap). *Deut. Hydrogr. Z.*, 8:1–95. 22

He, X., Hu, T., Wang, Y., Zou, X., and Shi, X. (2010). Seasonal distributions of hydrometeor parameters in the offshore sea of Jiangsu. *Marine Science*, 34:44–54. 11

Holthuijsen, L., Booij, N., and Ris, R., editors (1993). *A spectral wave model for the coastal zone*, volume Proceedings of the 2nd International Symposium on Ocean Wave Measurement and Analysis, New Orleans. 17

Huang, C., Zhang, M., Zou, J., Zhu, A., Chen, X., Mi, Y., Wang, Y., Yang, H., and Li, Y. (2015). Changes in land use, climate and the environment during a period of rapid economic development in Jiangsu Province, China. *Science of The Total Environment*, 536:173 – 181. 2

Huo, W., Zhang, W., and Chen, P. S. C. (2018). Recent development of Chinese port cooperation strategies. *Research in Transportation Business & Management*, 26:67 – 75. Port co-operation: types, drivers and impediments. 2

Janssen-Stelder, B. (2000). The effect of different hydrodynamic conditions on the morphodynamics of a tidal mudflat in the Dutch Wadden Sea. *Continental Shelf Research*, 20(12):1461 – 1478. 3

Kaji, A., Luijendijk, A., van Thiel de Vries, J., de Schipper, M., and Stive, M. (2014). Effect of different forcing processes on the longshore sediment transport at the Sand Motor, The Netherlands. volume 1. 17

Larsen, L., Cannon, G., and Choi, B. (1985). East China Sea tide currents. *Continental Shelf Research*, 4(1):77 – 103. Sediment Dynamics of the Changjiang Estuary and the Adjacent East China Sea. 7, 9

Lee, H. and Chough, S. (1989). Sediment distribution, dispersal and budget in the Yellow Sea. *Marine Geology*, 87(2):195 – 205. 11, 12

Lesser, G., Roelvink, J., van Kester, J., and Stelling, G. (2004). Development and validation of a three-dimensional morphological model. *Coastal Engineering*, 51(8):883 – 915. 17

Li, C. X., Zhang, J. Q., Fan, D. D., and Deng, B. (2001). Holocene regression and the tidal radial sand ridge system formation in the Jiangsu coastal zone, east China. *Marine Geology*, 173(1):97 – 120. 8, 13

Li, R., Yu, Q., Wang, Y., Wang, Z. B., Gao, S., and Flemming, B. (2018). The relationship between inundation duration and Spartina alterniflora growth along the Jiangsu coast, China. *Estuarine, Coastal and Shelf Science*, 213:305 – 313. 3

Liu, J., Kong, X., Saito, Y., Liu, J., Yang, Z., and Wen, C. (2013). Subaqueous deltaic formation of the Old Yellow River (AD 1128–1855) on the western South Yellow Sea. *Marine Geology*, 344:19 – 33. 9, 11, 12

Liu, J. P., Xu, K. H., Li, A. C., Milliman, J. D., Velozzi, D. M., Xiao, S. B., and Yang, Z. S. (2007). Flux and fate of Yangtze River sediment delivered to the East China Sea. *Geomorphology*, 85(3-4):208–224. 12, 22, 27

Liu, Q., Yan, Y.-R., Xiang, L.-H., Zhang, X.-F., and Peng, X.-Q. (2016). The influence of breakwater construction on the underwater terrain in the Binhai Port, Yancheng City. *Institute of Geochemical Exploration and Marine Geological Survey, East China Mineral Exploration and Development Bureau, Nanjing, China.* x, 25, 45, 46

Liu, X. (2011). The coastal erosion of the abandoned Yellow River Delta in northern Jiangsu province, China: Based on analysis of remote sensing images. In *19th International Conference on Geoinformatics*, pages 1–5. 9, 38

Liu, X., Gao, S., and Wang, Y. (2011). Modeling profile shape evolution for accreting tidal flats composed of mud and sand: A case study of the central Jiangsu coast, China. *Continental Shelf Research*, 31(16):1750 – 1760. 12

Lu, J., Li, A., Huang, P., and Li, Y. (2015). Mineral distributions in surface sediments of the western South Yellow Sea: implications for sediment provenance and transportation. *Chinese Journal of Oceanology and Limnology*, 33:510–524. 11

Lu, Q. and Chen, S. L. (2011). Distribution of Surface Sediments on the Subaqueous Delta of the Abandoned Yellow River Delta. *Shanghai Land and Resources*. 13

Luan, H., Ding, P., Wang, Z., Yang, S., and Lu, J. (2018). Morphodynamic impacts of large-scale engineering projects in the Yangtze River delta. *Coastal Engineering*, 141:1 – 11. 12

Maren, D., Winterwerp, J., and Vroom, J. (2015). Fine sediment transport into the hyper-turbid lower Ems River: the role of channel deepening and sediment-induced drag reduction. *Ocean Dynamics*, 65. 22, 23, 98

Melville, D. (2018). Perspective: China's coasts – a time for cautious optimism? *Wader Study*, 125(1):1–3. 4

Melville, D., Chen, Y., and Ma, Z. (2016). Shorebirds along the Yellow Sea coast of China face an uncertain future - A review of threats. *Emu*, 116. 14, 15

Meng, L., Huang, J., and Dong, J. (2018). Assessment of rural ecosystem health and type classification in Jiangsu province, China. *Science of The Total Environment*, 615:1218 – 1228. 2

Meng, W., Hu, B., He, M., Liu, B., Mo, X., Li, H., Wang, Z., and Zhang, Y. (2017). Temporal-spatial variations and driving factors analysis of coastal reclamation in China. *Estuarine, Coastal and Shelf Science*, 191:39 – 49. 1, 2

Muller, J. (2018). Sustainable alternative designs for the Tongzhou Bay Port: A design study at the potential of alternative reclamation configurations through a 'Building-with-Nature' approach, in preserving and creating valuable habitat based on two specialised coastal shorebird species at the Jiangsu coast. Master's thesis, Delft University of Technology. 18, 21, 23, 26

Murray, N., Clemens, R., Phinn, S., Possingham, H., and Fuller, R. (2014). Tracking the rapid loss of tidal wetlands in the Yellow Sea. *Frontiers in Ecology and the Environment*, 12. 15

Nash, J. and Sutcliffe, J. (1970). River flow forecasting through conceptual models part I — A discussion of principles. *Journal of Hydrology*, 10(3):282 – 290. 27

National Bureau of Statistics (2018). China Statistical Yearbook 2018. http://www.stats.gov.cn/tjsj/ndsj/2018/indexeh.htm. 1

Partheniades, E. (1965). Erosion and Deposition of Cohesive Soils. *Journal of the Hydraulics Division*, 91(1):105 – 139. 18, 26, 94, 97

Piersma, T., Chan, Y. C., Mu, T., Hassell, C. J., Melville, D. S., Peng, H. B., Ma, Z., Zhang, Z., and Wilcove, D. S. (2017). Loss of habitat leads to loss of birds: reflections on the Jiangsu, China, coastal development plans. *Wader Study*, page 93–98. ix, 4, 15, 16

Pritchard, D. and Hogg, A. J. (2003). Cross-shore sediment transport and the equilibrium morphology of mudflats under tidal currents. *Journal of Geophysical Research: Oceans*, 108(C10). 3

Qingguang, Z., Wang, Y. P., Ni, W., Gao, J., Li, M., Yang, L., Gong, X., and Gao, S. (2016). Effects of intertidal reclamation on tides and potential environmental risks: a numerical study for the southern Yellow Sea. *Environmental Earth Sciences*, 75. 3

Ren, M. E. (1986). Coastal and tidal flat resources investigation of Jiangsu province. *Peking, China: Maritime Press*. 9, 11

Roberts, W., Le Hir, P., and Whitehouse, R. (2000). Investigation using simple mathematical models of the effect of tidal currents and waves on the profile shape of intertidal mudflats. *Continental Shelf Research*, 20(10):1079 – 1097. 3

Roelvink, J. (2006). Coastal morphodynamic evolution techniques. *Coastal Engineering*, 53(2):277 – 287. Coastal Hydrodynamics and Morphodynamics. 23

Roos, P., Schuttelaars, H., and Brouwer, R. (2013). Observations of barrier island length explained using an exploratory morphodynamic model. *Geophysical Research Letters*, 40(16):4338–4343. 49

Shepard, F. P. (1954). Nomenclature based on sand-silt-clay ratios. *Journal of Sedimentary Research*, 24(3):151–158. 96

Shi, B., Cooper, J., Pratolongo, P., Gao, S., Bouma, T. J., Li, G., Li, C., Yang, S., and Wang, Y. (2017). Erosion and Accretion on a Mudflat: The Importance of Very Shallow-Water Effects. *Journal of Geophysical Research: Oceans*, 122(12):9476–9499. 3, 26, 100

Shi, B., Wang, Y., Wang, L., Li, P., Gao, J., Xing, F., and Chen, J. D. (2018). Great differences in the critical erosion threshold between surface and subsurface sediments: A field investigation of an intertidal mudflat, Jiangsu, China. *Estuarine, Coastal and Shelf Science*, 206:76 – 86. 26, 94

Shi, Z. and Chen, J. (1996). Morphodynamics and sediment dynamics on intertidal mudflats in China (1961–1994). *Continental Shelf Research*, 16(15):1909 – 1926. 3

Song, D., Wang, X. H., Zhu, X., and Bao, X. (2013). Modeling studies of the far-field effects of tidal flat reclamation on tidal dynamics in the East China Seas. *Estuarine, Coastal and Shelf Science*, 133:147 – 160. 3

Studds, C. E., Kendall, B. E., Murray, N. J., Wilson, H. B., Rogers, D. I., Clemens, R. S., Gosbell, K., Hassell, C. J., Jessop, R., Melville, D. S., Milton, D. A., Minton, C. D. T., Possingham, H. P., Riegen, A. C., Straw, P., Woehler, E. J., and Fuller, R. A. (2017). Rapid population decline in migratory shorebirds relying on Yellow Sea tidal mudflats as stopover sites. *Nature Communications*, 8:14895. 4

Su, M., Stive, M., Zhang, C., Yao, P., Chen, Y., and Wang, Z. (2013). The tidal wave system in the Chinese marginal seas. 9

Su, M., Yao, P., Wang, Z., Zhang, C., and Stive, M. (2015). Tidal Wave Propagation in the Yellow Sea. *Coastal Engineering Journal*, 57. 9, 11, 19, 21

Su, M., Yao, P., Wang, Z. B., Zhang, C. K., and Stive, M. J. F. (2017a). Exploratory morphodynamic hindcast of the evolution of the abandoned Yellow River delta, 1578–1855CE. *Marine Geology*, 383:99 – 119. 10, 12, 19, 23

Su, M., Yao, P., Wang, Z. B., Zhang, C. K., and Stive, M. J. F. (2017b). Exploratory morphodynamic modeling of the evolution of the Jiangsu coast, China, since 1855: Contributions of old Yellow River-derived sediment. *Marine Geology*, 390:306 – 320. 4, 7, 12, 24

Tao, J., Wang, Z., Zhou, Z., Xu, F., Zhang, C., and Stive, M. (2019). A Morphodynamic Modeling Study on the Formation of the Large-Scale Radial Sand Ridges in the Southern Yellow Sea. *Journal of Geophysical Research: Earth Surface*. 9

Tao, J., Yang, T., xu, F., and Yao, J. (2011). Effect of Large Scale Tidal Flat Reclamation on Hydrodynamic Circulation in Jiangsu Coastal Areas. pages 662–669. 3

Temmerman, S., Meire, P., Bouma, T., Herman, P., Ysebaert, T., and de Vriend, H. (2013). Ecosystem-based coastal defence in the face of global change. *Nature*, 504:79–83. 4

To, W. M. and Lee, P. K. C. (2018). China's Maritime Economic Development: A Review, the Future Trend, and Sustainability Implications. *Sustainability*, 10(12):1–13. 1, 2

van Rijn, L. (1993). Principles of sediment transport in rivers, estuaries and coastal seas. Aqua Publications, Amsterdam. 18, 97

van Rijn, L. C. (2007a). Unified View of Sediment Transport by Currents and Waves. I: Initiation of Motion, Bed Roughness, and Bed-Load Transport. *Journal of Hydraulic Engineering*, 133(6):649–667. 18, 97

van Rijn, L. C. (2007b). Unified View of Sediment Transport by Currents and Waves. II: Suspended Transport. *Journal of Hydraulic Engineering*, 133(6):668–689. 18, 97

van Rijn, L. C. (2007c). Unified View of Sediment Transport by Currents and Waves. III: Graded Beds. *Journal of Hydraulic Engineering*, 133(7):761–775. 18

Vledder, G., Zijlema, M., and Holthuijsen, L. (2011). Revisiting the JONSWAP bottom friction formulation. volume 1. 22

Wang, B. C. (1980). The change of coasts and beaches and the movement of longshore sediments of Haizhou bay. *Acta Oceanologica Sinica* , 2(1):79–96. 12

Wang, F. and Wall, G. (2010). Mudflat development in Jiangsu Province, China: Practices and experiences. *Ocean & Coastal Management*, 53(11):691 – 699. 1, 2, 7, 15

Wang, L., Fang, Z., and Huang, H. (2008). Influence of reclamation on suspended sediment field in Wenzhou estuarine and offshore waters. *Journal of Waterway and Harbor*, 29(6):383–393. 3

Wang, W., Liu, H., Li, Y., and Su, J. (2014). Development and management of land reclamation in China. *Ocean & Coastal Management*, 102:415 – 425. The Korean Tidal Flat Systems: Ecosystem, land reclamation and struggle for protection. 1

Wang, X. and Ke, X. (1997). Grain-size characteristics of the extant tidal flat sediments along the Jiangsu coast, China. *Sedimentary Geology*, 112(1):105 – 122. xv, 7, 8, 9, 12, 13, 14

Wang, X., Qiao, F., Lu, J., and Gong, F. (2011). The turbidity maxima of the northern Jiangsu shoal-water in the Yellow Sea, China. *Estuarine, Coastal and Shelf Science*, 93(3):202 – 211. 13, 24, 26

Wang, Y. (2002). Radiative Sandy Ridge Field on Continental Shelf of the Yellow Sea. In *Beijing: ChinaEnvironmentalSciencePress,1stedition*. 22, 104

Wang, Y., Gao, S., Jia, J., Thompson, C., Gao, J., and Yang, Y. (2012a). Sediment transport over an accretional intertidal flat with influences of reclamation, Jiangsu coast, China. *Marine Geology*, 291-294:147 – 161. 23

Wang, Y., Ren, M., and Zhu, D. (1986). Sediment supply to the continental shelf by the major rivers of China. *Journal of the Geological Society*, 143(6):935–944. 7

Wang, Y., Zhang, W., Huang, H., and Chen, C. (2015). Review of studies on sources and transport of sediment in radial sand ridges. 35:59–67 and 88. 22

Wang, Y., Zhang, Y., Zou, X., Zhu, D., and Piper, D. (2012b). The sand ridge field of the South Yellow Sea: Origin by river–sea interaction. *Marine Geology*, 291-294:132 – 146. 1, 7, 8, 9

Wei, Y. and Fan, C. (2000). Regional inequality in China: A case study of Jiangsu province. *The Professional Geographer*, 52(3):455–469. 2

Winterwerp, J. C., Lely, M., and He, Q. (2009). Sediment-induced buoyancy destruction and drag reduction in estuaries. *Ocean Dynamics*, 59(5):781–791. 97

World Bank (2018). Belt and Road Initiative. https://www.worldbank.org/en/topic/regional-integration/brief/belt-and-road-initiative. 2

World Bank (2019). Gross domestic product 2018. World Development Indicators database. 1

Wu, H., Deng, B., Yuan, R.and Hu, J., Gu, J., Shen, F., Zhu, J., and Zhang, J. (2013). Detiding Measurement on Transport of the Changjiang-Derived Buoyant Coastal Current. *Journal of Physical Oceanography*, 43(11):2388–2399. 11, 12

Wu, H., Shen, J., Zhu, J., Zhang, J., and Li, L. (2014). Characteristics of the Changjiang plume and its extension along the Jiangsu Coast. *Continental Shelf Research*, 76:108 – 123. 11, 12

Xie, F., Pang, Y., and Zhuang, W. (2008). Study on regularity of matter transportation in the nearshore area of the Haizhou Bay. *Advances in Marine Science*, 26(3):347–353. In Chinese. 14

Xing, F., Wang, Y., and Gao, J. (2010). Seasonal distributions of the concentrations of suspended sediment along Jiangsu coastal sea. *Oceanologia Et Limnologia Sinica*, 41:459–468. 13

Xing, F., Wang, Y. P., and Wang, H. V. (2012). Tidal hydrodynamics and fine-grained sediment transport on the radial sand ridge system in the southern Yellow Sea. *Marine Geology*, 291-294:192 – 210. ix, 8, 9, 10, 23

Xingjian, L. (2011). The coastal erosion of the abandoned Yellow River Delta in northern Jiangsu province, China: Based on analysis of remote sensing images. *Proceedings - 2011 19th International Conference on Geoinformatics, Geoinformatics*, pages 1–5. 4, 13, 14

Xinhua (2018). China determined to advance ecological civilization. http://www.chinadaily.com.cn/a/201805/21/WS5b021145a3103f6866ee9826.html. 4

Xinhua (2018). China Focus: China introduces toughest ever regulation on land reclamation. http://www.xinhuanet.com/english/2018-01/18/136903321.htm. 4

Xinhua Finance Agency (2017). Jiangsu Port Group established consolidation of two listed port companies. http://en.xfafinance.com/html/Companies/2017/332694.shtml. 2

Xu, F., Tao, J., Zhou, Z., Coco, G., and Zhang, C. (2016). Mechanisms underlying the regional morphological differences between the northern and southern radial sand ridges along the Jiangsu Coast, China. *Marine Geology*, 371:1 – 17. 1, 8, 9, 11

Yao, P. (2016). *Tidal and Sediment Dynamics in a Fine-Grained Coastal Region: A Case Study of the Jiangsu Coast*. PhD thesis, Delft University of Technology, Delft. i, 6, 9, 13, 17, 18, 20, 21, 22, 23, 25, 26, 27, 31, 32, 61, 67, 81, 87, 92, 94, 96, 97, 104

Yao, P., Su, M., Wang, Z., van Rijn, L., Zhang, C., Chen, Y., and Stive, M. (2015). Experiment inspired numerical modeling of sediment concentration over sand–silt mixtures. *Coastal Engineering*, 105:75 – 89. 18, 97

Yao, P., Su, M., Wang, Z. B., Van Rijn, L. C., Zhang, C., and Stive, M. J. F. (2018). Modelling tidal-induced sediment transport in a sand-silt mixed environment from days to years: Application to the Jiangsu coastal water, China. *Coastal Engineering*, 141:86 – 106. 9, 10, 11, 12, 13, 14, 18, 19

Yao, P., Wang, Z., Zhang, C., Su, M., Chen, Y., and Stive, M. (2013). The genesis of the radial tidal current off the Central Jiangsu Coast. Number 7th International Conference on Coastal Dynamics, Arcachon, France. Bordeaux University. 7, 9

Yu, Z., Zhang, Y., and Liu, J. (1994). The erosion process of open mud beach and its protection along the coast of northern Jiangsu. *Acta Geographica Sinica*, 49(2). 4

Yu, Z.-Y., Zhang, Y., Jin, L., and Bao, S. (2002). Evolution prediction of the Abandoned Yellow River Submerged Delta under Wave and Current. *Oceanologica et Limnologia Sinica*, (33):583–590. Chinese. 4

Yuan, D., Li, Y., Wang, B., He, L., and Hirose, N. (2017). Coastal circulation in the southwestern Yellow Sea in the summers of 2008 and 2009. *Continental Shelf Research*, 143:101 – 117. 11

Yuan, R., Wu, H., Zhu, J., and Li, L. (2016). The response time of the Changjiang plume to river discharge in summer. *Journal of Marine Systems*, 154:82 – 92. Changjiang (Yangtze River) Estuary and Adjacent Marine Environment. 11

Zhai, F. (2018). China's belt and road initiative: A preliminary quantitative assessment. *Journal of Asian Economics*, 55:84 – 92. Trade, Industrialization, and Structural Reform in Southeast Asia. 2

Zhang, C. (2012). Suspended Sediment Transport in Lianyungang Nearshore Area. *Applied Mechanics and Materials*, pages 170–173. 14

Zhang, C. and Chen, J. (2011). Master plan of tidal flat reclamation along Jiangsu coastal zone. pages 139–146. Proceedings of the 6th International Conference on Asian and Pacific Coasts, Hong Kong, China. 2

Zhang, C. K. and Ed. (2012). The Comprehensive Survey and Evaluation Report on Coastal Zone of Jiangsu Province. Beijing: Science Press. 20

Zhang, C.and Zhang, D., Zhang, J., and Wang, Z. (1999). Tidal current-induced formation—storm-induced change—tidal current-induced recovery. *Science in China Series D: Earth Sciences*, 42:1–12. 9

Zhang, L., Chen, S., Pan, S., Yi, L., and Jiang, C. (2014). Sediment variability and transport in the littoral area of the abandoned Yellow River Delta, northern Jiangsu. *Journal of Geographical Systems*, 24:717–730. ix, 9, 11, 12, 13, 14, 15, 23, 101

Zhang, L., Chen, S., and Yi, L. (2015). The Sediment Source and Transport Trends around the Abandoned Yellow River Delta, China. *Marine Georesources and Geotechnology*, 34. 4, 9, 10, 11, 12, 13, 101

Zhang, Q., Gong, Z., Zhang, C. K., Townend, I., Jin, C., and Li, H. (2016). Velocity and sediment surge: What do we see at times of very shallow water on intertidal mudflats. *Continental Shelf Research*, (113):10–20. 26

Zhang, R. (1992). Suspended sediment transport processes on tidal mud flat in Jiangsu Province, China. *Estuarine, Coastal and Shelf Science*, 35(3):225 – 233. 9

Zhang, R., Lu, L., and Wang, Y. (2002). The mechanism and trend of coastal erosion of Jiangsu Province in China. *Geographical research*, 21(4):469. 4, 9, 12

Zhou, L., Liu, J., Saito, Y., Zhang, Z., Chu, H., and Hu, G. (2014). Coastal erosion as a major sediment supplier to continental shelves: example from the abandoned Old Huanghe (Yellow River) delta. *Continental Shelf Research*, 82:43 – 59. 4, 7, 9, 10, 11, 12, 13, 14, 38

Zhu, D., Martini, I. P., and Brookfield, M. E. (1998). Morphology and Land-Use of the Coastal Zone of the North Jiangsu Plain Jiangsu Province, Eastern China. *Journal of Coastal Research*, 14(2):591–599. 1, 2, 7, 8, 9, 11, 12, 23

Zhu, Q., van Prooijen, B., Wang, Z., and Yang, S. (2017). Bed-level changes on intertidal wetland in response to waves and tides: A case study from the Yangtze River Delta. *Marine Geology*, 385:160 – 172. 11

Zhu, Q., Wang, Y., Ni, W., and Gao, J. (2016). Effects of intertidal reclamation on tides and potential environmental risks: a numerical study for the southern Yellow Sea. *Environmental Earth Sciences*, 75:1. 3

Zhu, Y. and Chen, Q. (2005). On the Origin of the Radial Sand Ridges in the Southern Yellow Sea: Results from the Modeling of the Paleoradial Tidal Current Fields off the Paleo-Yangtze River Estuary and Northern Jiangsu Coast. *Journal of Coastal Research*, pages 1245–1256. 7, 9

A
Data Analysis

The Jiangsu Regional Model (JRM) has been calibrated and verified as described by Yao (2016). The refined Abandoned Yellow River Delta Model is an outcrop of the JRM which has been set-up, calibrated and verified for available data within the mentioned region. The datasets used within this research will be further elaborated in this section.

A.1 Tidal datum

The tidal levels along the Abandoned Yellow River Delta are examined by traditional water level measurement interpretation. Tidal levels include Mean Sea Level (MSL), Mean High Water (MHW) and Mean Low Water (MLW). The MHW is defined as the average of all high tides and the MLW as the average of all low tides. Furthermore, the Mean High Water Spring (MHWS) and Mean Low Water Spring (MLWS) are defined as the highest and lowest tidal levels respectively of two consecutive high- and low waters during spring- and neap tide. The reference level is an important feature and can be set to MSL or a specific coordinate system (e.g. Beijing 54 Chart Datum). The reference level within the model is set to MSL. An overview of tidal levels at Xiangshui station can be seen in Table A.1.

Tide w.r.t. mean sea level	Xiangshui station
Mean tidal range (m)	2.78
MLW (m)	-1.31
MHW (m)	1.47
1985 National Elevation Benchmark	-0.044

Table A.1: Tidal datum - Xiangshui station

A.2 Measurements

This research makes use of two datasets which originate from seven stations along the Abandoned Yellow River Delta. An overview of their locations can be seen in Figure A.1.

The first dataset is retrieved from six temporary stations which were placed prior to the Binhai Port construction. The purpose of these stations were to gain insight in the hydrodynamical environment before port development. The dataset contains water levels, current velocities, current direction and suspended sediment concentrations (SSC) from (10/06/07 - 11/06/07) and (15/06/07 - 16/06/07) corresponding to neap- and spring tide respectively.

The second dataset is retrieved from a station located at Xiangshui County. Tidal levels are made available from (10/06/07 - 16/06/07), however both current- and SSC measurements lack. Furthermore, one-year wave data has been made available. The data spans from Dec-2014 till Aug-2015 over an hourly measurement interval. An overview of all data can be found in Table A.2.

Data	Binhai - Six stations		Xiangshui - One station	
	Neap	Spring	Neap	Spring
Water level	Yes	Yes	Yes	Yes
Velocity	Yes	Yes	x	x
Direction	Yes	Yes	x	x
Suspended - Sediment Concentration	Yes	Yes	x	x
Wave	x	x	2014-2015	
Wind	x	x	x	x
Salinity	x	x	x	x

Table A.2: Overview of available datasets

A.2.1 Water level

The water level measurements at Binhai and Xiangshui are shown in Figure A.2. The water level at Binhai's stations show the same values within a neap- and spring tidal cycle, since their spacing is much smaller than the tidal wavelength in order to observe level differences. The water levels are measured at an hourly interval at Binhai and a ten minute interval at Xiangshui station.

In general, it can be seen that the tidal asymmetry is larger at spring tide (15/06/07 - 16/06/07) than at neap tide (10/06/07 - 11/06/07). Furthermore, the tidal range is slightly larger at Xiangshui. The mean tidal range during spring ranges at 2.27 - 3.45 m at Binhai and Xiangshui respectively. The ebb phases are slightly longer and flood phases shorter, which indicates a flood dominant environment.

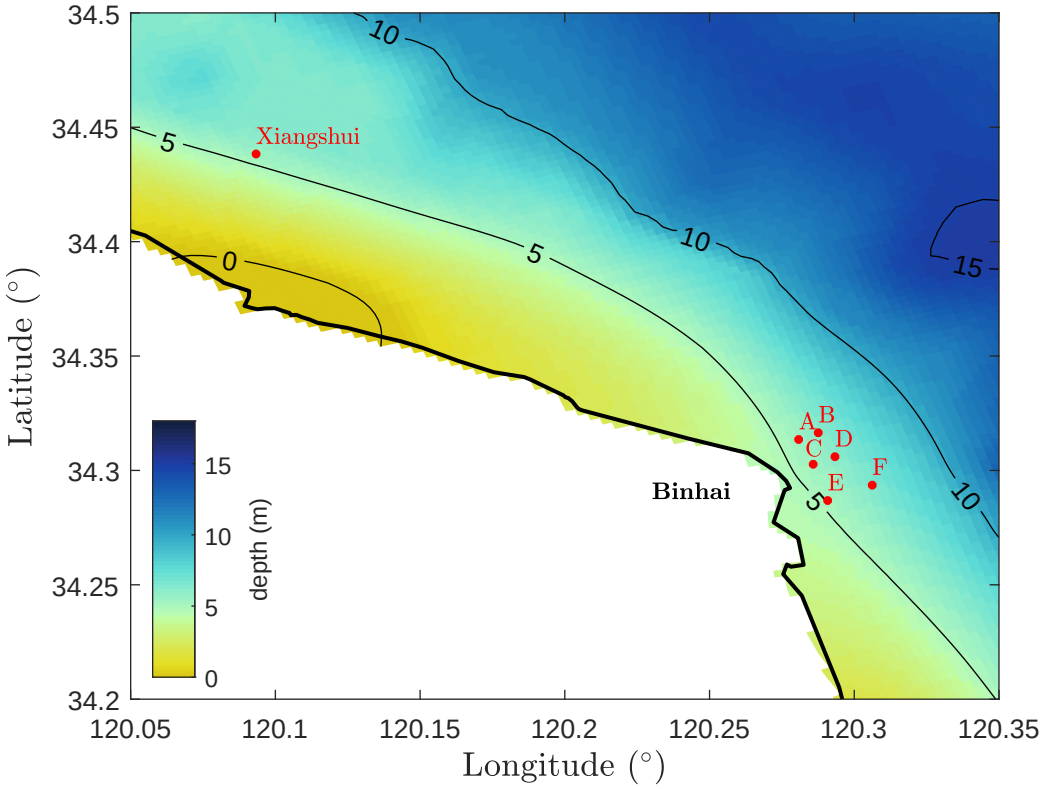

Figure A.1: Overview of measurement stations at the Abandoned Yellow River Delta

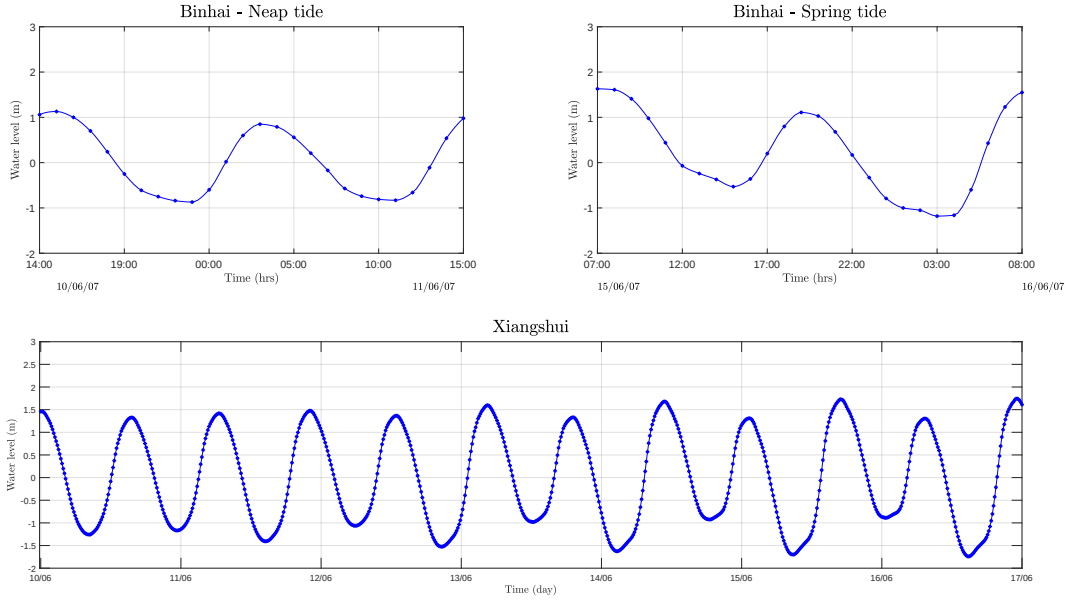

Figure A.2: Water level measurements at Binhai and Xiangshui

A.2.2 Current velocity

Measurements of current velocities and directions are only available at the stations of Binhai. These measurements were performed during neap- (10 - 11) and spring tide (15 - 16) in June 2007 on an hourly interval. The results are shown in Figure A.3 for stations B, D and F at neap tide (left) and spring tide (right). The flood direction is south-east at approximately 140° - 150° and ebb direction is north-northeast at approximately 340° - 350°. The ebb- and flood velocities are in the same order of magnitude and do not differ significantly. In general, flood velocities are slightly larger at both spring- and neap tide. Exceptional is station F at neap tide, where the ebb tidal velocities are slightly larger. It can be concluded that at the Binhai area both ebb- and flood velocities are significant. Flood velocities are overall larger and therefore Binhai can be seen as a flood dominant environment.

A.2.3 Suspended sediment concentration

The suspended sediment concentrations (SSC) have been measured at the stations of Binhai. These measurements were performed during neap- (10 - 11) and spring tide (15 - 16) in June 2007 on an hourly interval. The results are shown in Figure A.4 for stations B, D and F at neap tide (left) and spring tide (right). In general, it can be seen that higher values for SSC are observed at spring tide. Furthermore, higher values for SSC are observed during flood which is the result from higher flood velocities. During spring tide SSC ranges between 0.82 - 1.87 kg/m^3, while during neap tide SSC ranges between 0.48 - 1.44 kg/m^3. It must be noted that the wave conditions are not known at time of the measurements.

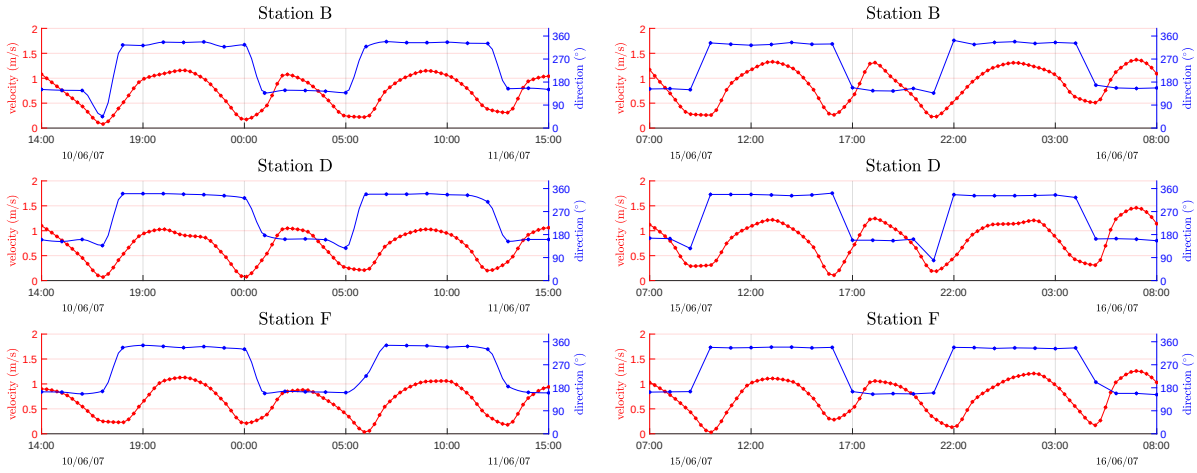

Figure A.3: Velocity and direction measurements at Binhai for stations B, D and F. Neap- and spring tide are illustrated left and right respectively

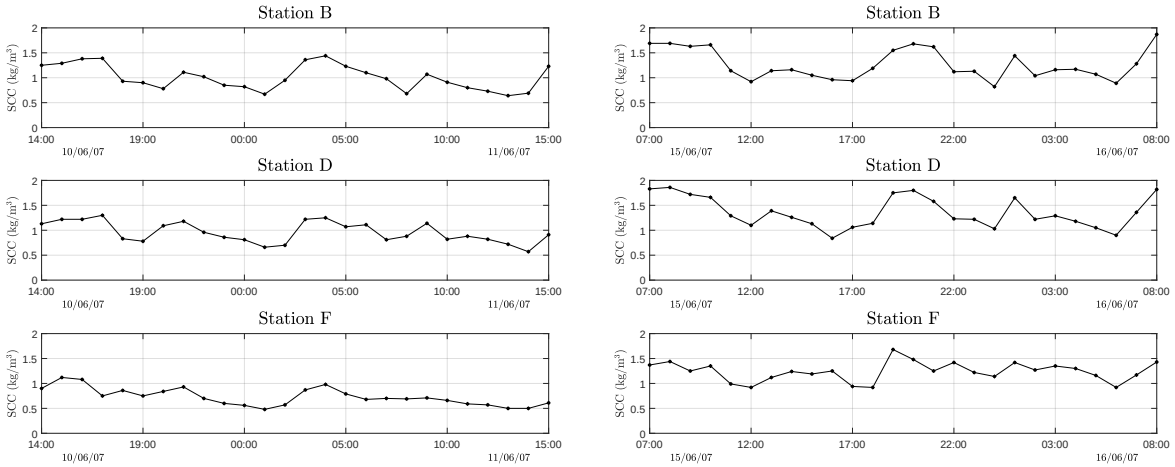

Figure A.4: Total suspended sediment concentrations at Binhai for stations B, D and F. Neap- and spring tide are illustrated left and right respectively

A.2.4 Wave

Wave measurements have been performed at Xiangshui station from December 2014 until August 2015. Measurements have been performed on an hourly interval. In Figure A.5 a wave rose can be seen of the collected data for the significant wave height (H_s) and the wave direction. Small waves from the south-east are dominating the Abandoned Yellow River Delta, while larger waves are observed from the north-east. The wave data shows the importance of wind, since waves from the north-west tend to be quite significant in height. This is remarkable due to the limited fetch length regarding the Shandong Peninsula and shallow sea increasing bed friction. Furthermore, waves are measured from west and south-west direction who can only be induced by local wind. Wind data is however not available within this research. Closer examination of the H_s shows an equal distribution pattern of high and low waves throughout the year.

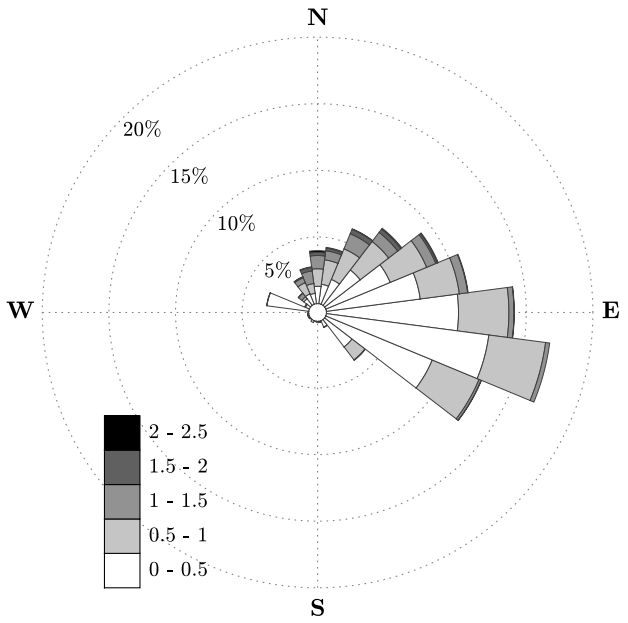

Figure A.5: Wave rose of measured waves at Xiangshui station. The directional rose shows the frequency of incoming waves from multiple directions

B
Model Calibration

B.1 Model development

B.1.1 Jiangsu Regional Model

Within this research use has been made of the Jiangsu Regional Model (JRM) set-up by Yao (2016). In order to obtain insight in the model's performance on the new obtained data, the stations of Binhai and Xiangshui were included in the original grid. However, not all stations were overlapped by the coarse grid. By updating the land boundary within the model it became clear that the land boundary had moved landward. The grid has therefore been extended to the updated boundary. A clear overview of the described situation can be seen in Figure B.4. As a first step to introduce bathymetry to the added grid, the original bathymetry has been converted into point data. The data has been interpolated consequently using the Delft3D 'Triangular Interpolation' option. Preliminary results showed the local bathymetry was too shallow. The incorrect water levels at stations C and E can be seen for neap- and spring tide in Figure B.1 and Figure B.2 respectively. The bathymetry has been adjusted in numerous iterations in order to obtain the most favourable bathymetry while minimise changes in the original. The correctness of the initial obtained bathymetry were compared with a bathymetry contour figure. This figure was found in literature and describes the situation prior to construction of Binhai Port. The bed roughness has been modified in a later stage. More on this in Section B.2.3.

For this research a 2016 bathymetry has been made available at the Binhai region. The survey includes Binhai port (constructed in 2010-2011), and shows significant and abrupt depth change at the intersection of the original- and survey bathymetry. The Abandoned Yellow River Delta (AYRD) is a severe eroding coastline. Since the calibration data is dated nine years, it was decided to not implement the 2016 survey.

B.1.2 Abandoned Yellow River Delta Model

This research focusses at the Abandoned Yellow River Delta. The goal is to protect the delta against erosion by means of island implementation and along to enhance mudflat growth. Islands will enhance less energetic conditions which is beneficial for mudflat growth. These mudflats affect the ecological system positively. In order to obtain a higher resolution. The Abandoned Yellow River Delta Model (AYRDM) has been cropped from the JRM. The grid has been refined at 3:1 relative to the original JRM grid, shown in Figure B.4. An overview of

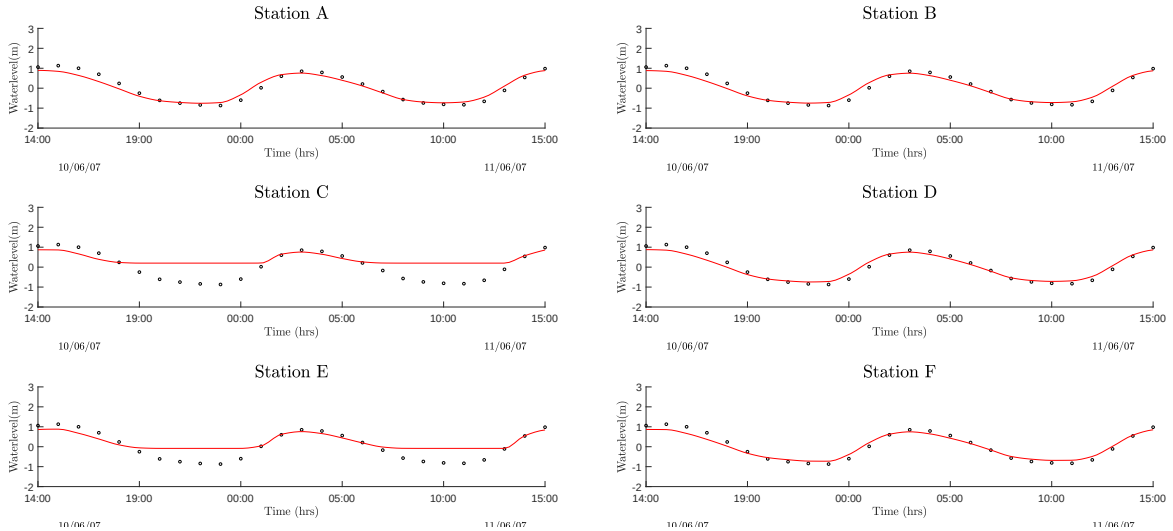

Figure B.1: Water level model results from the original Jiangsu Regional Model at neap tide (10 - 11 June 2007). The depth is not sufficient in station C and E

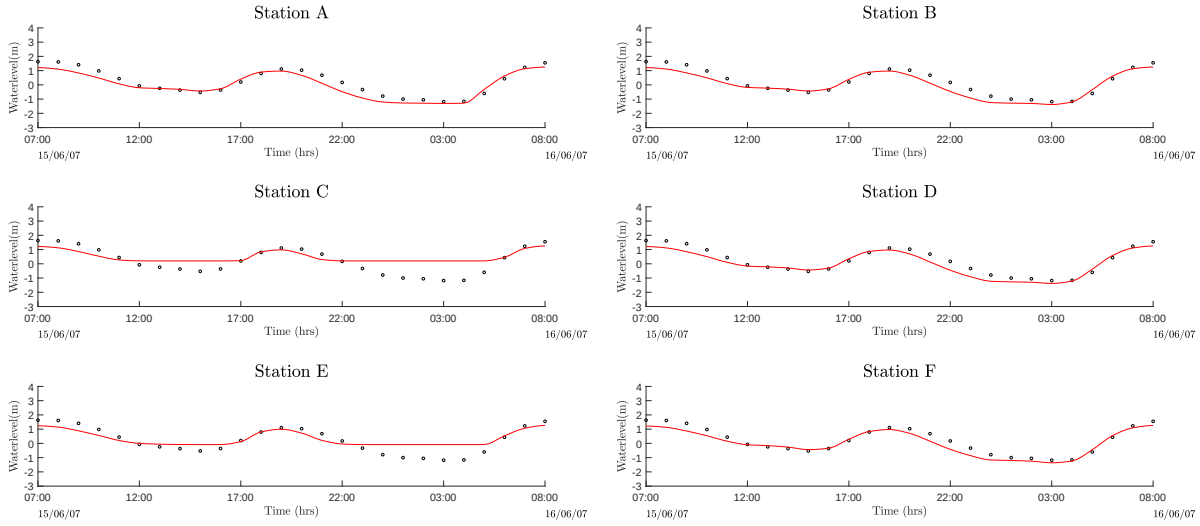

Figure B.2: Water level model results from the original Jiangsu Regional Model at spring tide (15-1 6 June 2007). The depth is not sufficient in station C and E

the AYRDM and JRM can be seen in Figure B.3

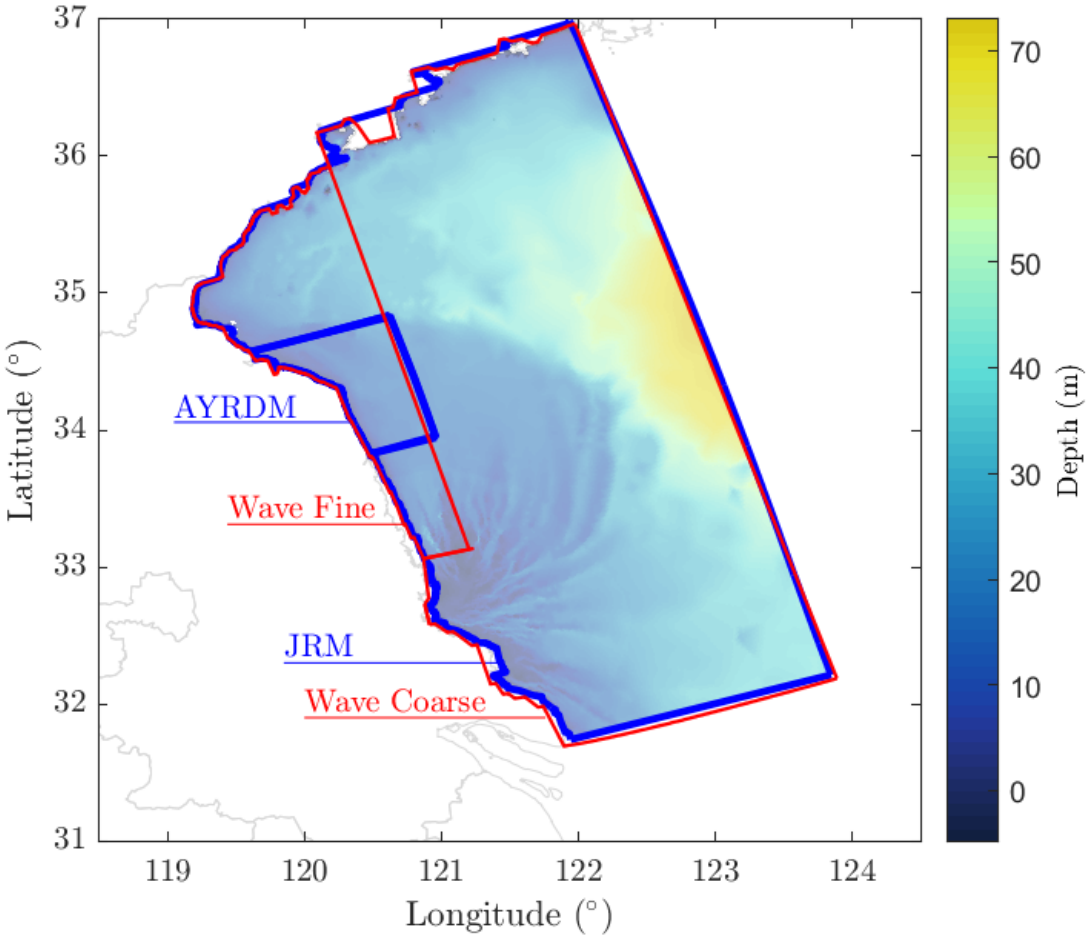

Figure B.3: Overview of the Flow and Wave computational grids. The grids from the AYRDM and JRM are depicted in blue, whereas coarse and fine wave grids are depicted in red

Preliminary results of the AYRDM show a somewhat lower amplitude of the water level after implementation of the higher resolution grid. The effect on water level can be seen in Figure B.5 for stations B, D and F. The water level is slightly under-estimated. The results on current velocity and current direction are visible in Figure B.6 for stations B, D and F. The JRM slightly overestimated the flood velocities, however was accurate on the ebb velocities. The AYRDM shows a slight under-estimation of the ebb velocities and accurate results on flood velocities. The current direction is well predicted in both models. The JRM shows slight bumps, which are not visible within the AYRDM. The AYRDM shows a slight over-prediction at 09:00 during spring tide, where the JRM strongly under-estimates the direction.

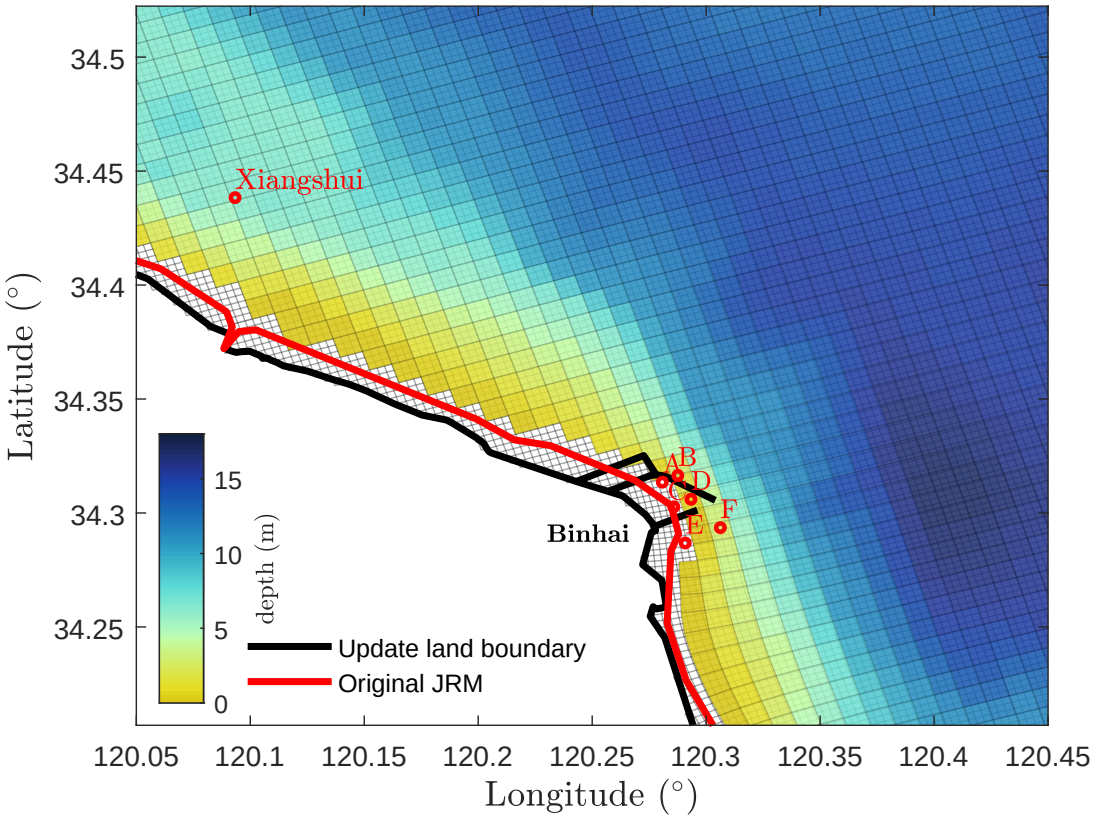

Figure B.4: The bathymetry and grid are shown of the original Jiangsu Regional Model. The red line represents the original land boundary. The black line represent the updated land boundary. The grid of the Abandoned Yellow River Delta model has been refined and is shown partially, to clearly visualise the extension of the grid.

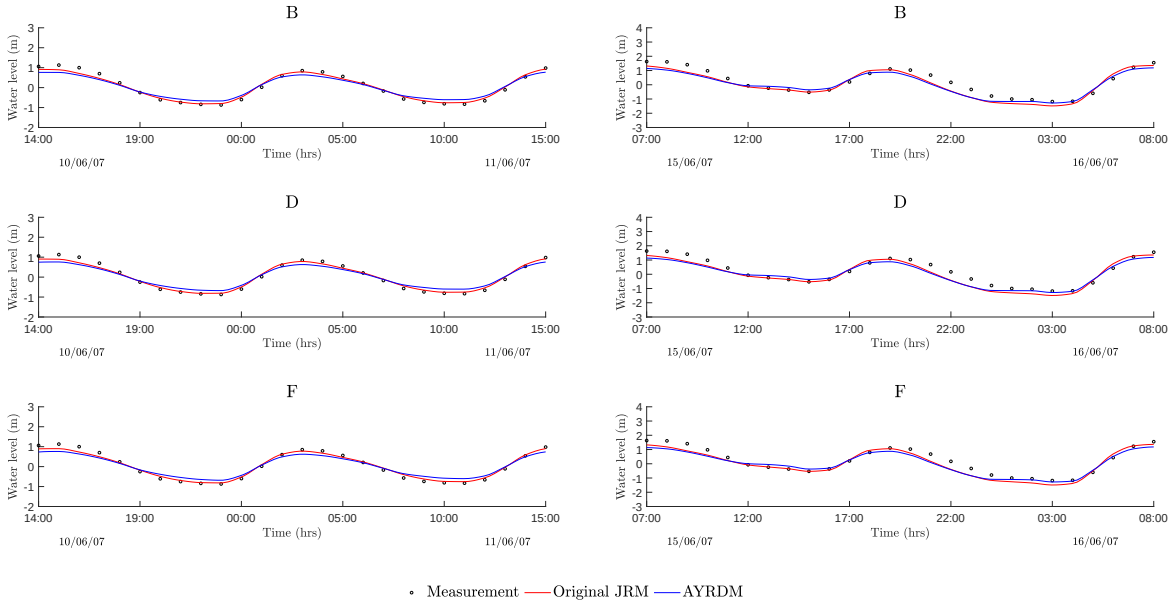

Figure B.5: Water level comparison after refinement between original Jiangsu Regional Model and Abandoned Yellow River Model

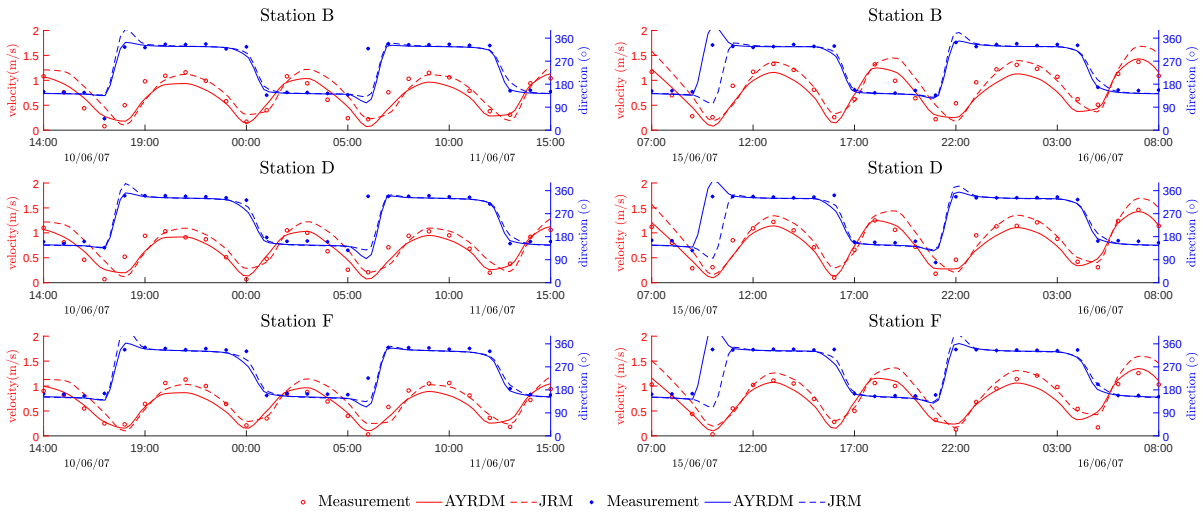

Figure B.6: Velocity and direction comparison after refinement between original Jiangsu Regional Model and Abandoned Yellow River Model

B.2 Model improvement

The AYRDM has been adjusted to the updated land boundary by grid extension and bathymetry calibration. The preliminary results on hydrodynamics fit well with the measurement data. This section further elaborates the calibration of the AYRDM with focus on suspended sediment concentrations. The following modifications are discussed:

- Revision of sediment fractions
- Calibration of cohesive fraction
- Simplified bed composition
- No bed roughness modification

All calibration simulations regarding the cohesive sediment are set from 28/05/07 - 17/06/07. All figures within this section represent the results from neap- and spring tide, left and right respectively.

B.2.1 Revision of sediment fractions

The JRM is set-up with a multi-fraction approach. Four fractions are included within the model representing fine silt (16 μm), coarse silt (45 μm), very fine sand (90 μm) and fine sand (180 μm). In order to see the preliminary results with four sediment fractions, the JRM has been set-up from 28/05/07 - 17/06/07 using the initial settings as described by Yao (2016). The model results are compared with the measurements taken during neap- (10-11/06/07) and spring tide (15-16/06/07), shown in Figure B.7. It can be seen that the fine silt (16 μm) reacts instantaneous with the flow and stays in suspension easily. Grain size affects weight and herewith settling velocity. The larger particles need larger current velocities to suspend in the water column. It can be seen that the contribution of the larger particles in general is less. These only contribute to the peak current velocities. Generally, the SSC show large dependency on flow conditions, while the measurements show low dependency. After careful literature review it was found that three sediment fractions dominate the AYRD: fine sand, silt and a cohesive fraction. In order to save computational time and represent the environment at the AYRD it was chosen to reduce the number of non-cohesive fractions and add a cohesive fraction. The cohesive fraction will decrease dependency on flow conditions. Neglecting two non-cohesive fractions will flatten the peaks in SSC. The 45 μm and 180 μm fraction are not taken into account within this research due to their limited contribution or over-representation of the silt fraction. The next section will further elaborate on the calibration of this cohesive fraction.

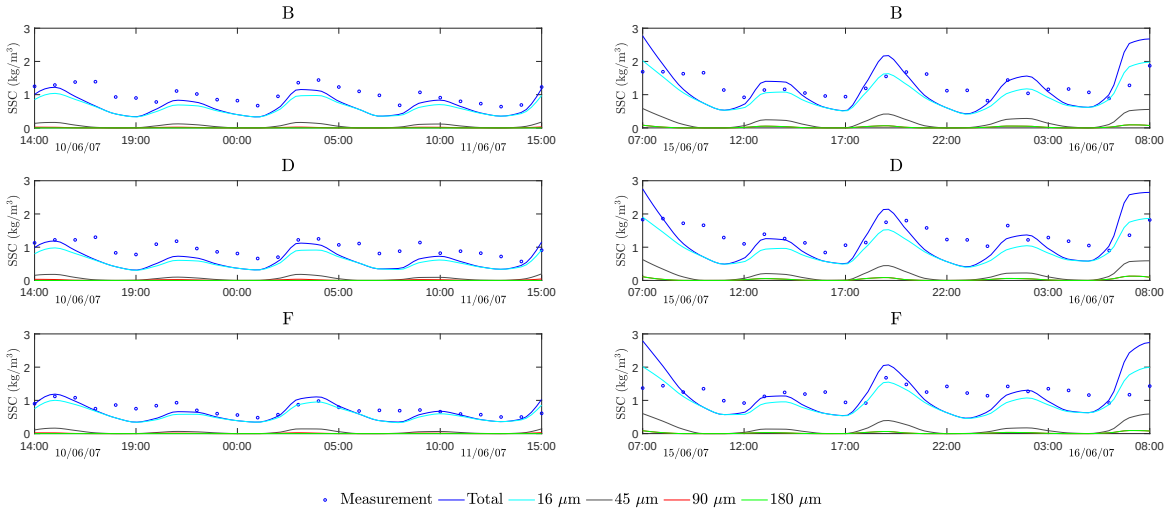

Figure B.7: Original set-up Jiangsu Regional Model; four sediment fractions

B.2.1.1 Calibration of cohesive fraction

Within this research a cohesive fraction has been added as described by Partheniades (1965). The sediment properties need to be carefully investigated since it is not clear what properties could represent the cohesive fraction. A sensitivity analysis is performed for several sediment properties through which a better behavioural understanding is obtained. Aside, a sensitivity analysis has been performed on initial- and boundary conditions, as well as initial bed layer thickness. A sensitivity analysis is performed for the parameters shown in Table B.1

	Symbol	Unit
Erosion parameter	M	($kg/m^2/s$)
Critical bed shear stress for erosion	τ_{ce}	(N/m^2)
Settling velocity	W_s	(m/s)
Boundary conditions SSC	-	-
Initial concentration	c_0	(mg/l)
Initial bed layer thickness	d_0	(m)

Table B.1: Calibration parameters

The sensitivity simulations are set with a critical erosion parameter of $\tau_{ce} = 0.29$ N/m^2. Shi et al. (2018) suggests the use of $\tau_{ce} = 0.18$ N/m^2 for the uppermost 0.02 m of the bed within fluid mud layers. The sub-surface layers are set to $\tau_{ce} = 0.29$ N/m^2 due to their increased stability. Both values are the result of wave-current measurements. The critical erosion parameter is therefore set to 0.29 N/m^2.
The bed composition within the JRM is spatial varying. The effect of a uniform- and spatial varying bed is investigated together with the erosion parameter. The total bed thickness within the calibration runs is set to six meter, as it originates from the initial thickness set by Yao (2016). The cohesive fraction is set at 0.2 m. The spatial varying bed is scaled up to a total bed thickness of 5.8 m. The uniform bed is made up of 2.9 m for each sediment fraction.

The **erosion parameter** regulates the amount of erosion when the critical erosion threshold is exceeded; $\tau > \tau_{ce}$, in which τ is the bed shear stress (N/m^2). The classical approach of Partheniades (1965) has been used for erosion (E) and deposition (D):

$$E = M(\frac{\tau - \tau_{ce}}{\tau_{ce}}), \quad (kg/m2/s) \tag{B.1}$$

The erosion parameter has been elaborately tested for three values and for both a uniform- (Figure B.8) and spatial varying bed composition (Figure B.9). The erosion parameter values are set to M = 10^{-3}, M = $0.5{\cdot}10^{-4}$ and M = 10^{-4} ($kg/m^2/s$), since high current velocities govern the AYRD. Higher erosion parameter values lead to higher erosion rates, which could lead to over predictions of SSC.
The results of the uniform bed composition show better resemblance (Figure B.8) compared to the spatial varying bed (Figure B.9). As from here, the uniform bed composition will be used within the following sensitivity simulations. The bed composition is further elaborated in B.2.2. The erosion parameter M = 10^{-4} ($kg/m^2/s$) is chosen.

The **critical shear stress for erosion** is the critical value of the bed shear stress for which erosion starts. Earlier research denoted the use of τ_{ce} = 0.11 - 0.29 N/m^2 in muddy environments under different forcing (Shi et al., 2018). The critical shear stress for erosion has

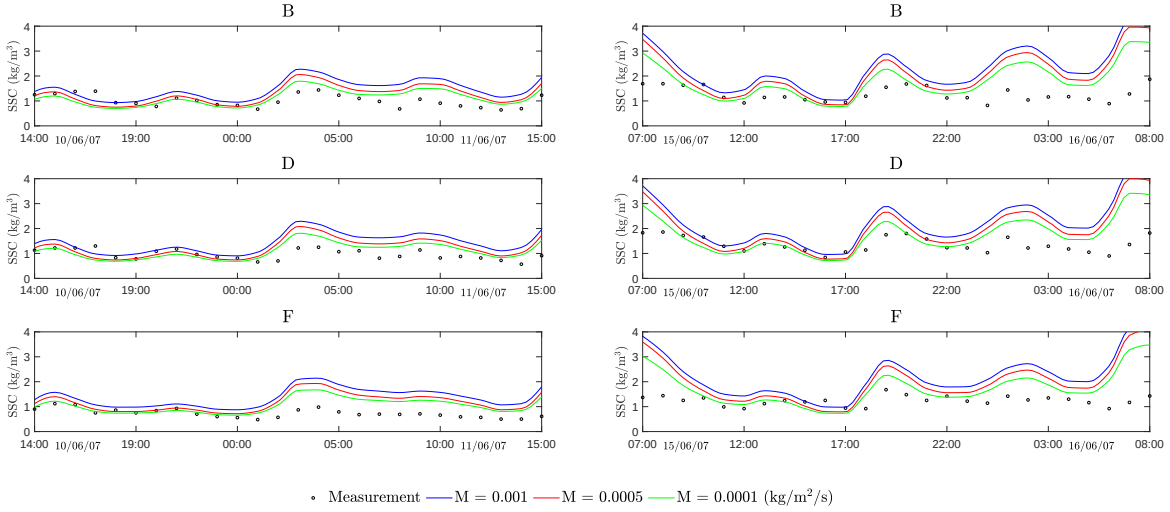

Figure B.8: Calibration of the cohesive fraction with an uniform bed composition. Varying erosion parameter (M) with $\tau_{ce} = 0.29$ N/m^2

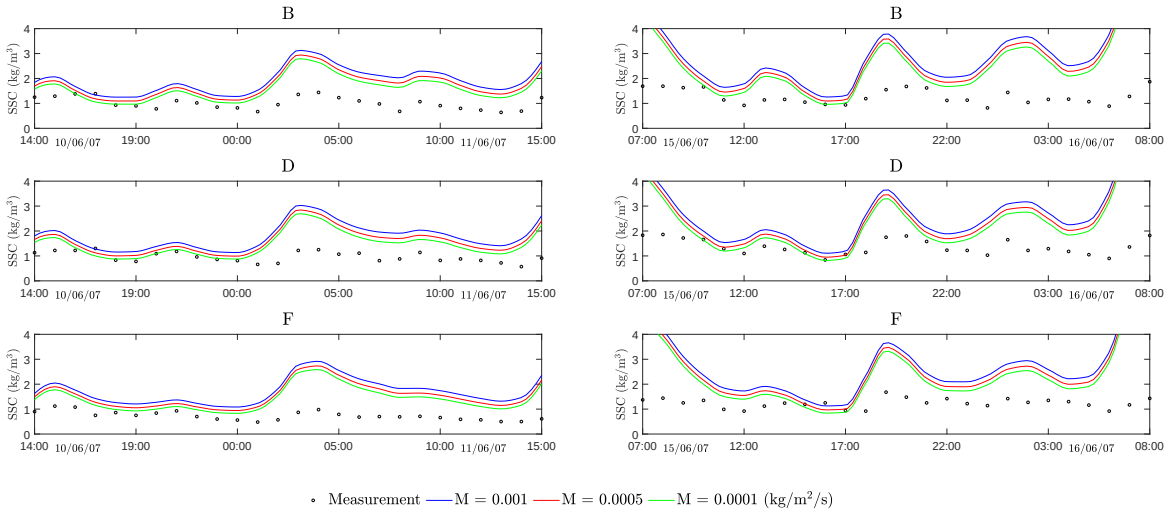

Figure B.9: Calibration of the cohesive fraction with the original spatially varying bed composition from the Jiangsu Regional Model. Varying erosion parameter (M) with $\tau_{ce} = 0.29$ N/m^2

been tested for three values; $\tau_{ce} = 0.11$ (N/m^2), $\tau_{ce} = 0.19$ (N/m^2) and $\tau_{ce} = 0.29$ (N/m^2). The results are shown in Figure B.10. When current velocities induce a bed shear stress below the critical bed shear stress, no erosion and increase of SSC will occur.

The **settling velocity** defines the velocity at which particles settle and thus the time for which particles remain in suspension. The settling velocity has been tested for two values; W$_s$ = 10^{-5} m/s and W$_s$ = 10^{-4} m/s. The results are shown in Figure B.11. It can be seen that the sediment with the lowest settling velocity maintains a higher SSC throughout the domain.

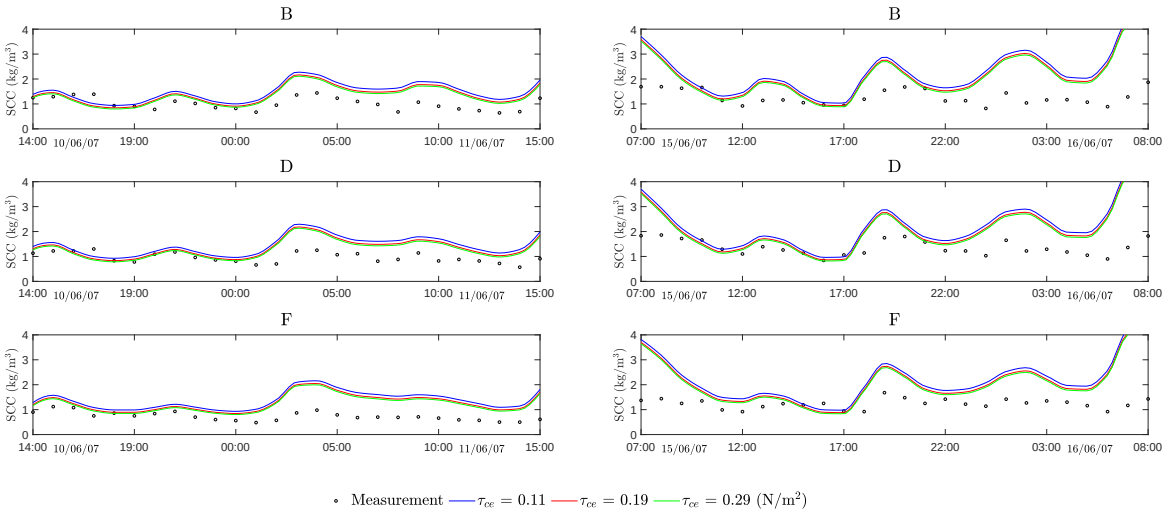

Figure B.10: Calibration of the cohesive fraction; varying the critical bed shear stress for erosion (τ_{ce})

B.2.2 Bed composition

The JRM is set-up with a spatial varying bed composition. The bed stratigraphy is a layered and vertically homogeneous. The stratigraphy system comprises a total thickness of six meter from which the topmost layer (i.e. transport layer) is active. The transport layer has a fixed thickness and interacts with the water column. When erosion occurs the active layer can be replenished by the sub-layers. Sediments mix within the active layer when siltation occurs and subsequently blend in the sub-layers. The chosen bed stratigraphy system mixes sediment on the topmost layer throughout the simulation. Correspondingly, the median grain size is changed, which would result in changes of the critical bed shear stress. Hence, sediment transport and consequently the SSC (Yao, 2016).

Yao (2016) states a better approximation of the initial bed composition is crucial for sediment transport and corresponding bed level changes. A conceptual approach has been applied in order to reconstruct the bed composition. Bed samples have been taken in 2006 along the Jiangsu coast. Together with analysing scientific reports on bed composition, the first step was to classify the bed sample data according to the method of Shepard (1954). Hereafter, Yao (2016) translated his findings into compositions of sediment fractions. The distribution is determined arbitrarily, however qualitatively consistent with the present understanding of sediment distribution along the Jiangsu coast.

The bed composition within the AYRDM has been tested for an uniform bed and the original spatial varying bed composition. The results are shown in Figure B.8 and B.9 respectively for a varying Erosion parameter. It can be seen that the spatial varying bed shows higher peak SSC. Due to the spatial differences in sediment fraction availability it is challenging to asses the contribution of each fraction to the SSC. Since the calibration data dates from 2007 and differs one year with 2006 bed sample data, it is chosen to use a uniform bed composition within this research. The uniform bed uses the same layered stratigraphy as described by Yao (2016). Ten sub-layers of 0.5 m are defined on a base-layer of 0.75 m. Hence, the active layer contributes to 0.25 m. The initial sediment thickness for each fraction are set to 0.2 m, 2.9 m and 2.9 m for

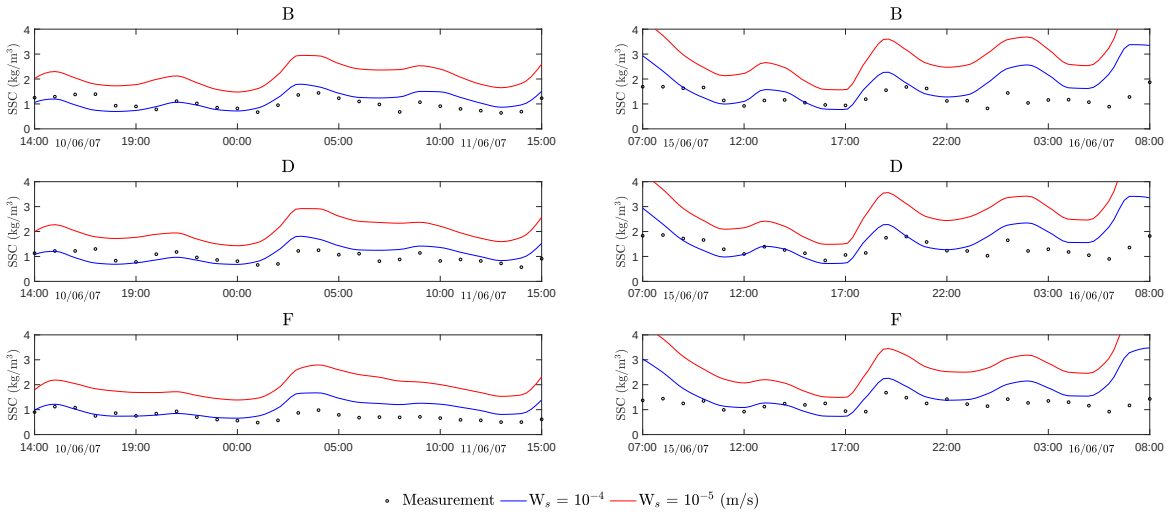

Figure B.11: Calibration of the cohesive fraction; varying the settling velocity (W_s)

the cohesive-, 16 μm- and 90 μm fraction respectively.

B.2.3 Bed roughness

The bed roughness within the JRM is calculated via the modified Van Rijn transport formulations (van Rijn, 2007a,b) as described by Yao et al. (2015); Yao (2016). Yao (2016) proofed by experimental research that the Van Rijn formulations could be extended by additional calibrations, to sand-silt mixtures in which grain sizes range from 8 μm to 125 μm. The sediment transport is calculated separately from the flow results. Bed- and suspended transport are calculated separately based on the van Rijn (1993) reference height. The modified formulations implement individual solvers for several transport parameters as for example the settling velocity, suspended- and bed load transport and equilibrium concentrations. The bottom friction has been determined by $n = 0.015 + 0.1/\mathrm{H}$, where H is the initial water depth. The depth-averaged SSC remains high at the AYRD, which can reduce hydraulic drag as suggested by Winterwerp et al. (2009). Consequently, the manning coefficient has been set to a constant value of 0.015 at the AYRD region. Due to the complex bathymetry found along the Jiangsu coast, Yao (2016) introduced a tuning parameter applied to the bed friction. This parameter changes local bed friction and therefore local current velocities.

The additive cohesive fraction requires different sediment transport formulations as described by Partheniades (1965). These formulations calculate sediment transport directly from the flow results. Therefore, the flow calibration approach of the JRM is not applicable since the flow and transport are separately calculated. For example; in certain regions where the current velocity was found to be too low, the tuning parameter lowers the manning coefficient in order to increase the current velocity. However, the sediment transport formulations as for cohesive sediment describe siltation for very low bed shear stresses. Therefore, the tuning parameter is not taken into account since siltation processes might have different causes.

The exclusion of the calibration factor has been carefully investigated by a sensitivity analysis on the bed roughness. Preliminary results showed model inaccuracies at the boundaries reflecting through the model domain. Therefore it was chosen to modify the extended grid cells

only.
The manning coefficient has been set to $n = 0.011$ s/m$^{1/3}$, $n = 0.014$ s/m$^{1/3}$, $n = 0.016$ s/m$^{1/3}$ and $n = 0.020$ s/m$^{1/3}$. The lowest two values are typical for a muddy bed, whereas the highest two values are typical for a sand bed (Maren et al., 2015). The environment is dominated by silt however. The muddy beds are smooth duo their small grain size. Aside their grain size, no large-scale sand dunes are found in muddy environments. Therefore the environment can be considered hydraulically smooth.
The results can be seen in Figure B.12. Generally, the lowest value of $n = 0.011$ s/m$^{1/3}$ fits the water level best. The highest value of the bed roughness dampens the wave amplitude. The effect on current velocity can be seen in Figure B.13. The lowest value of $n = 0.011$ s/m$^{1/3}$ induces over-estimations of the current velocity. Since the velocities are already high, it is chosen to use a constant value of $n = 0.014$ s/m$^{1/3}$ within the AYRDM. Then, the flood current velocities are well predicted. The ebb current velocities are however slightly under-estimated. The direction of flow can be seen in Figure B.6.

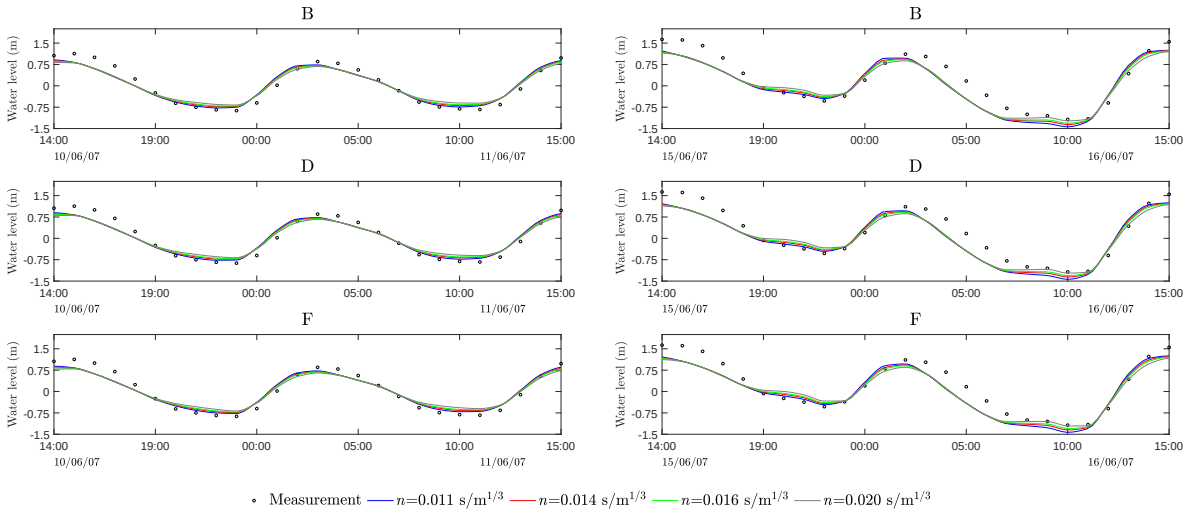

Figure B.12: Water level sensitivity analysis on bed roughness (Manning coefficient) at stations B, D and F. For both neap- and spring tide, left and right respectively

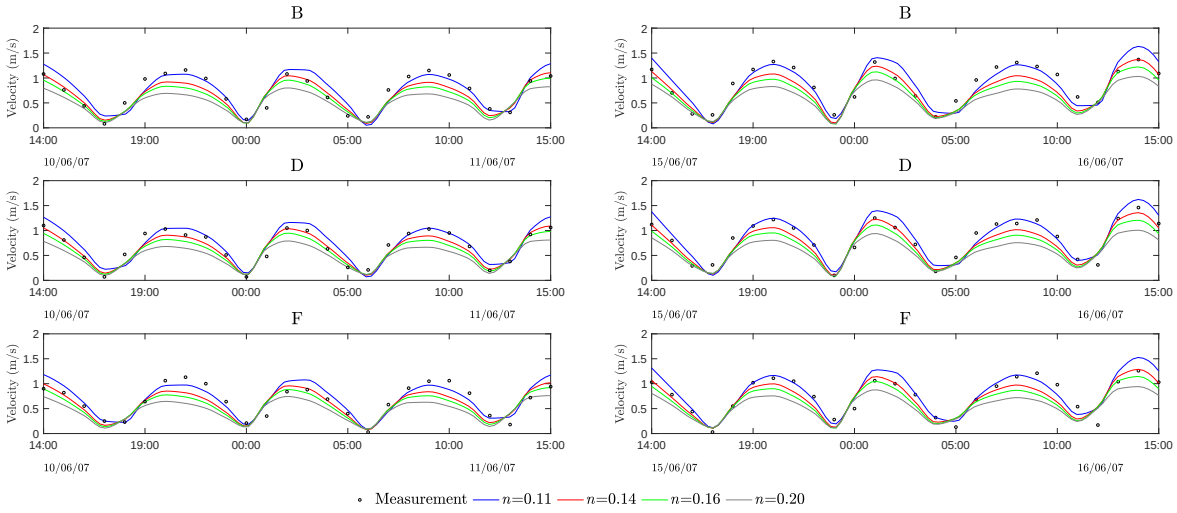

Figure B.13: Velocity sensitivity analysis on bed roughness (Manning coefficient) at stations B, D and F. For both neap- and spring tide, left and right respectively

B.3 Additional calibration

The preceding sections describe the alterations applied to the AYRDM (grid extension, bathymetry implementation, revision of sediment fractions and inclusion and calibration of a cohesive fraction). An extensive sensitivity analysis of several sediment characteristic parameters has brought a better understanding of the cohesive fraction's behaviour under current conditions. The calibration of the cohesive sediment has been done by simulations from 28/05/05 - 17/06/07.
In order to obtain similar sediment concentrations as seen in the measurements, several combinations of settings can be chosen. These settings include boundary conditions, initial sediment concentration and bed composition in terms of sediment volume. The inclusion of waves will lead to higher SSC values, since the bed shear stress will increase under wave-current conditions τ_{cw}.

Within this section sensitivity analyses are elaborated on the aforementioned variables. Both the boundary conditions and initial sediment concentrations are looked into for over a hydraulic period of six months. The volume fraction of each sediment fraction is elaborated for 28/05/07 - 17/05/07. The model results are from both wave and current forcing.

B.3.1 Wave forcing

B.3.1.1 General description

This research includes the effect of waves. Wave measurements have been obtained from one station at the Northern Abandoned Yellow River Delta (NARYD), just off the coast of Xiangshui. The waves are coupled to the flow simulations on a 20 minute interval (Section 3.2.2).

The wave computations are done on two separate grids, which are 'offline' coupled. A coarse grid exist which transfers the waves towards the AYRDM. The AYRDM's offshore boundary is where the coarse grid turns into the fine grid. The coarse grid counts 145 x 64 cells and has a resolution varying between 3000 - 4800 m. The fine grid contains 353 x 141 cells with a resolution varying between 800 - 1000 m. An overview can be seen in Figure B.3.

B.3.1.2 Wave calibration

The calibration of waves has been straightforward due to the lack of available data. Wave data is at hand from Dec-2014 till Aug-2015 over an hourly measurement interval. No wave data is available near the boundaries of the JRM. Furthermore, no wind- and tidal data is available during this period. As such, the wave data has been calibrated in a pragmatic way by multiple iterations of data editing and implementation at the open boundaries.

The **wave direction** (dir) has been filtered for directions between 30° and 180°. Wave directions smaller or larger are not achievable within the model at Xiangshui station. The main suggested reason is the lack of wind within the model. In Figure A.5 it can be seen that waves are measured from the north-west, west and south-west direction who can only be induced by local wind. Comparison of the peak wave period showed 3 - 4 seconds for this direction, which is related to short wind-waves (Shi et al., 2017). Wind data is not available for a similar period and therefore not taken into account. Another reason could be the effect of sheltering due to land boundaries.

The best results on **significant wave height** (H_s) were obtained by multiplication of the significant wave height by factor 1.2 and subsequently by 1.7 for wave heights larger than 0.65 m. The latter is to ensure large wave heights can be observed at Xiangshui station. The heightened waves set at the open boundary reach maximum wave heights up to five meter; a common value found in earlier research (Zhang et al., 2014, 2015).

The edited wave data has been translated into a Wavecon-file as described in Deltares (2018). The individual wave conditions within the Wavecon-file are set at a 20 minute interval. Stationary wave computations are performed and are exchanged on a 20 minute interval with Delft3D Flow. The boundary conditions are uniformly set at both open boundaries. The JONSWAP bottom friction coefficient has been set to 0.038 m^2/s^{-3}. Furthermore, a directional spread has been assumed of 10°. Other settings are held original as described by Deltares (2018).
The calibration- and production simulations differ in time span. The calibration simulations cover four consecutive spring-neap tidal cycles, whereas the production simulations cover a longer hydraulic period. The 20 minute time interval between each wave condition is set in both cases. Therefore, the calibration simulation only runs part of the total year wave data, while the production simulations include a full year wave representation. Different from all other calibration simulations is the physical presence of Binhai Port within the model. Binhai Port's breakwaters were constructed during 2010 - 2011, hence present during the wave measurements in 2014 - 2015.

B.3.1.3 Wave results

Within this section a comparison is done of the wave measurements and model predictions for the first 460 wave conditions. The results of the significant wave height (H_s), wave direction (dir) and peak wave direction (T_p) are shown in Figure B.14, Figure B.15 and Figure B.16 respectively. The significant wave heights show good results in comparison with the measurements. The model's predictions on wave directions show less agreement with the measurements. It can be seen that waves from the south-east are under-estimated by the model, which is further elaborated in Section 4.1.2.2. The waves from the north-east are slightly under-estimated, however show good agreement. The peak wave period show generally good resemblance with the measurements.

The effect of waves on the SSC is shown in Figure B.21. Here, the final calibration results are shown of the total SSC after a four consecutive spring-neap tidal cycle. The initial sediment bed thickness of the cohesive fraction is shown for both 0.1 and 0.2 m inclusion. The 0.2 m inclusion induces the best fit to the measured depth-averaged SSC values. Furthermore. the 0.2 m initial bed thickness has been modelled for tide-only and wave-current forcing in order to show the effect of waves on the SSC.

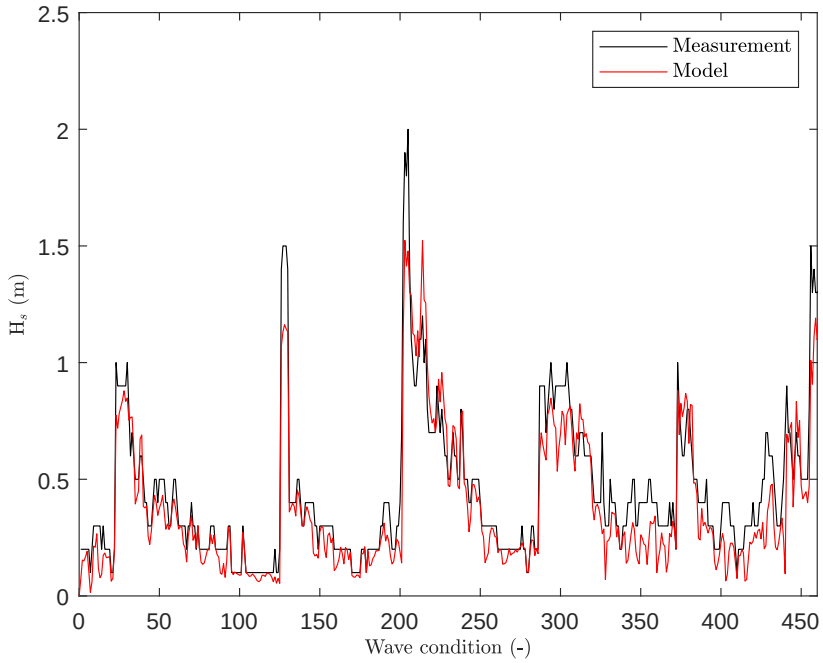

Figure B.14: Comparison of measurements with model results on the significant wave height (H_s). Measurements and model results from Xiangshui station

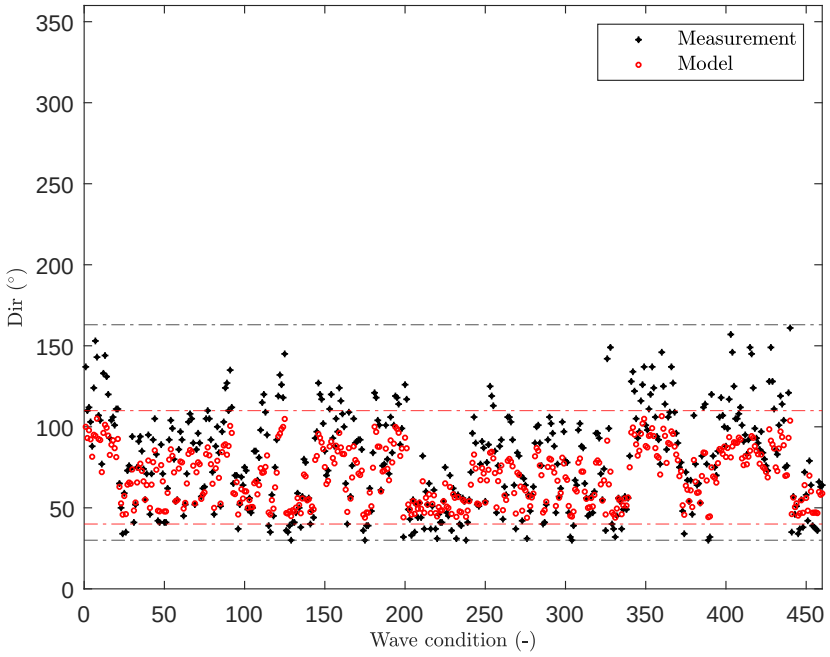

Figure B.15: Comparison of measurements with model results on the wave direction (°). Measurements and model results from Xiangshui station

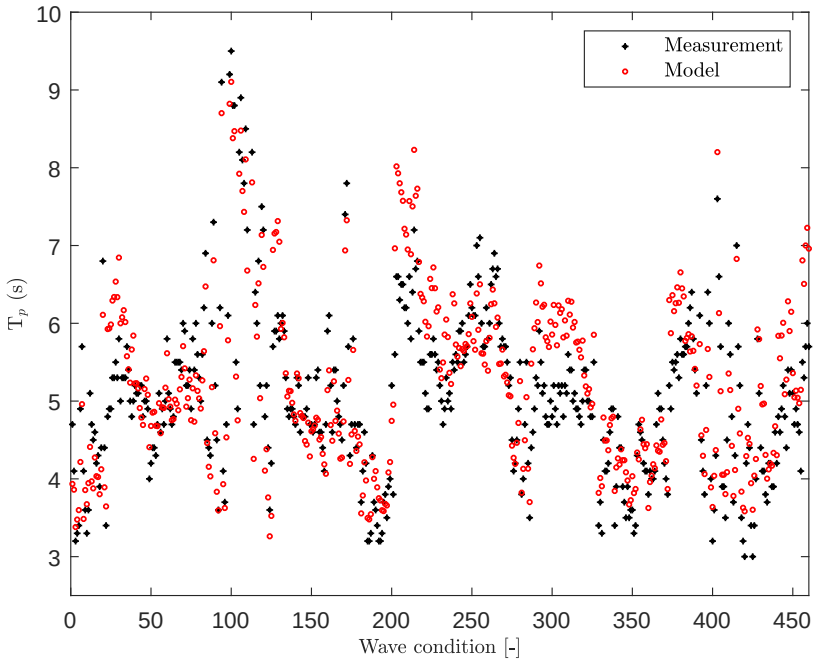

Figure B.16: Comparison of measurements with model results on the wave period (T_p). Measurements and model results from Xiangshui station

B.3.2 Boundary conditions

The boundary conditions of the JRM are set identical as described by Yao (2016). The JRM is set-up with a continuous sediment flux entering the domain at its two open boundaries. Yao (2016) assumed that fluxes entering via the eastern boundary are rather small. Yao (2016) has set the inflow of 16 μm fraction to 0.5 mg/l, while retaining the other fractions at zero. The sediment concentration inflow of the southern boundary has been argued by (Yao, 2016) due to the close presence of the Yangtze River. Hence, it is assumed that suspended loads enter only at depths smaller than 30 m. The sediment concentration inflow is set at 100 mg/l for the 16 µm fraction (e.g. representative fraction Yangtze River) for depths smaller than 30 m (Wang, 2002). From a depth of 30 m to offshore, the SSC is linearly decreasing to 0.5 mgl/l. Other fractions are set to zero.

A simulation has been set-up in order to see if the open boundaries influence the AYRD region. This simulation is set without bed composition and initial sediment concentration. The simulation period has been set to six months (01/01/07 - 30/06/07). At the two open boundaries of the JRM a uniform sediment influx of 300 mg/l is set for the cohesive fraction. The results at Binhai are shown in Figure B.17 and Xiangshui in Figure B.18. In both cases the green line represents the influence of boundary conditions for the cohesive fraction only. It can be seen that the influence is negligible.

The boundary conditions are retained for an additional sensitivity analysis on the initial sediment concentration. Three values are carefully investigated for the cohesive fraction. These are C_0 = 150 mg/l, C_0 = 250 mg/l and C_0 = 350 mg/l. The results are shown within the same Figures. It can be observed that the amount of SSC is gradually increasing over time for all initial concentrations. No significant difference can be observed in the development of sediment concentration between both stations. At each location a gradual rise in SSC is observed which flattens over time.

As a result, the initial concentration is set to 200 mg/l in further simulations. The boundary conditions are set to 20 mg/l at both the eastern- and southern boundary. The southern boundary is similarly constructed as for the 16 μm fraction. From shore towards a depth of 30 meter is set to a linearly decreasing SSC of 200 mg/l to 20 mg/l.

B.3.3 Bed configuration

A sensitivity analysis has been performed on the initial bed layer thickness of the cohesive fraction. The initial bed layer thickness has been set to three values, while retaining a total bed thickness of six meter. The values considered are 0.02 m, 0.10 m and 0.20 m. The sensitivity analysis has been performed for two forcing scenario's; tide-only and tidal forcing including waves. The latter is in order to clearly visualise the effect of waves. The simulation time has been reduced for this analysis, in order to gain a preliminary insight. The simulations are set from 28/05/07 to 17/06/07, representing three weeks. The results of tidal forcing only are shown in Figure B.19. The results of tidal forcing including waves are shown in Figure B.20. Larger SSC values are observed for the inclusion of waves, since waves have significant effect on the resuspension of fines due to increased bed shear stresses. Furthermore, a larger spread between SSC values of varying bed layer thicknesses can be seen due to the effect of waves.

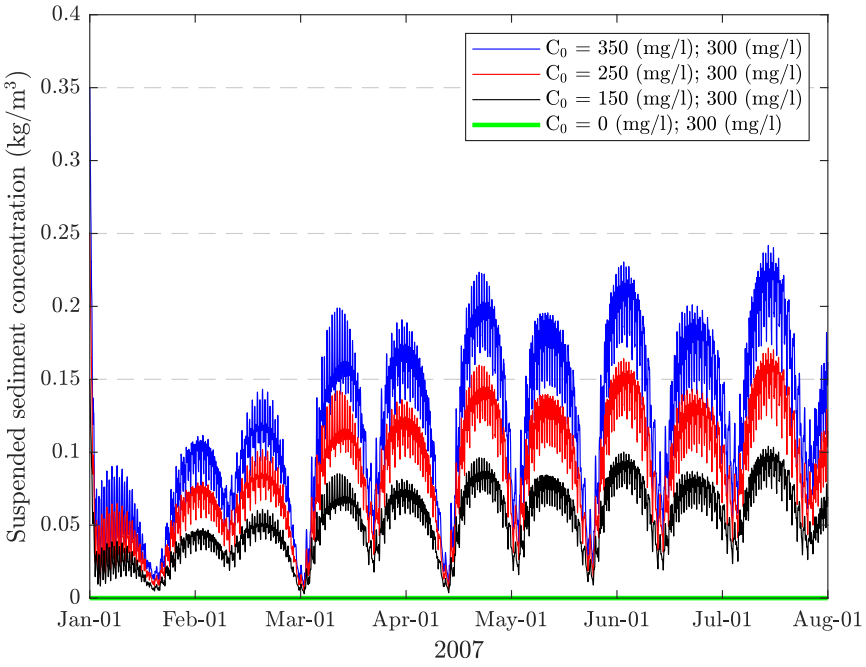

Figure B.17: Determining the boundary condition's influence at Binhai (negligible). Hence, varying the initial suspended sediment concentration for the cohesive fraction only. No sediment was included within the bed

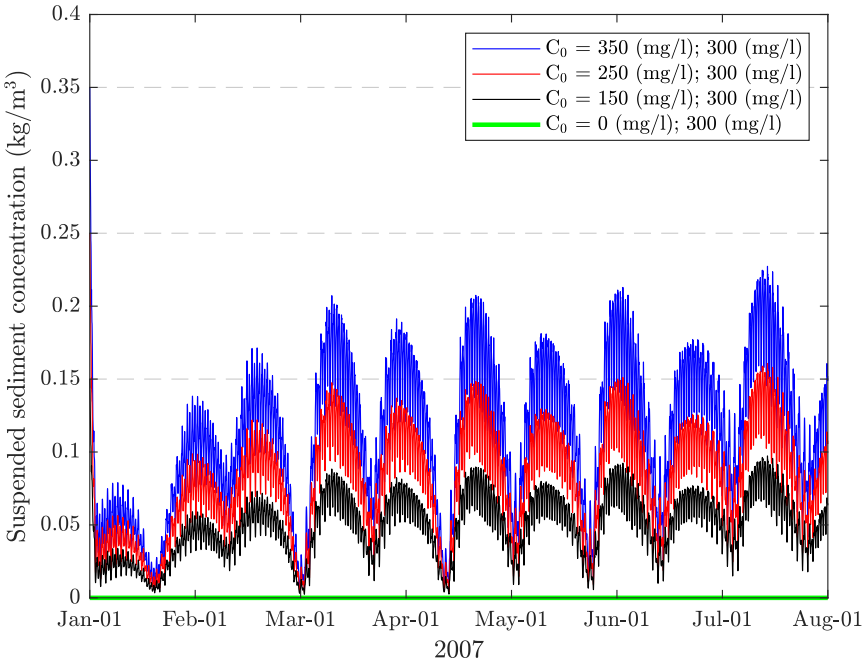

Figure B.18: Determining the boundary condition's influence at Xiangshui (negligible). Hence, varying the initial suspended sediment concentration for the cohesive fraction only. No sediment was included within the bed

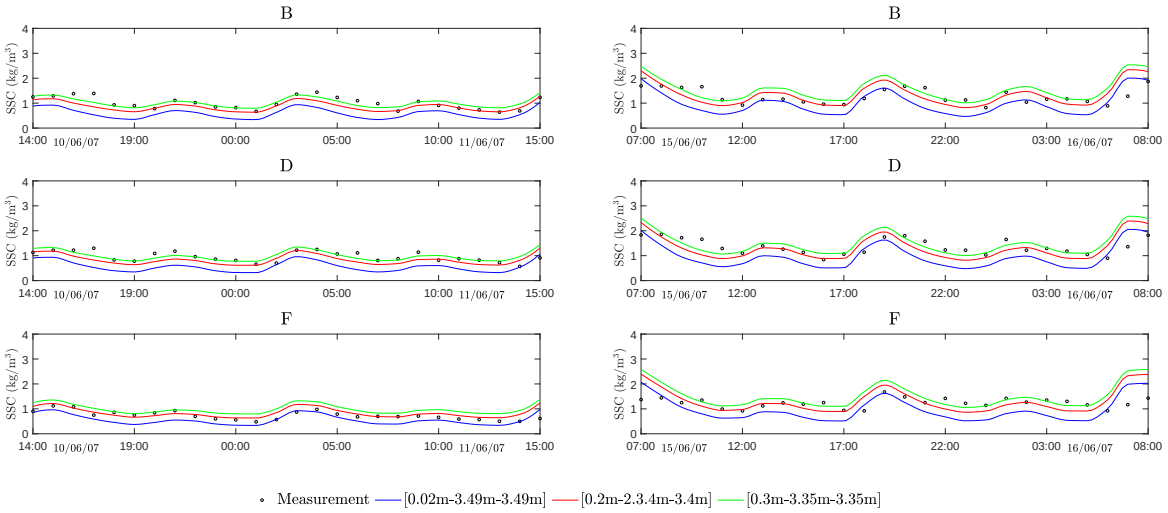

Figure B.19: Varying the cohesive fraction within the bed composition [cohesive fraction, 16μm, 90μm]. Excluding wave forcing

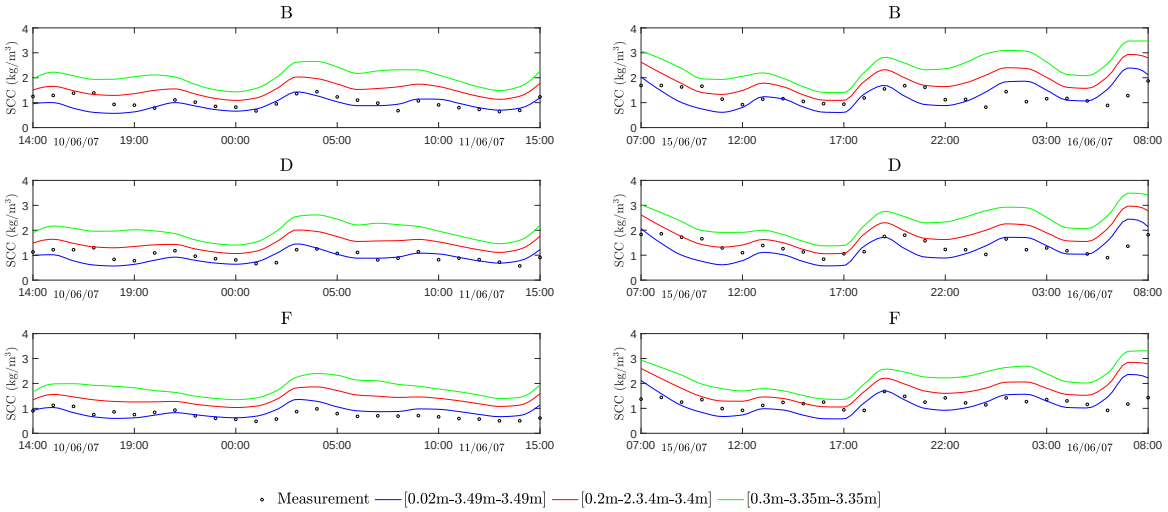

Figure B.20: Varying the cohesive fraction within the bed composition [cohesive fraction, 16μm, 90μm]. Including wave forcing

B.3.4 Suspended sediment concentration after calibration

The latter simulations have given a good understanding of the impact on SSC along the AYRD. The total bed thickness has however been increased with one meter, ensuring sufficient erodible material (of the cohesive fraction) is present in the bed throughout the domain. The bed stratigraphy is again set-up with ten sub-layers of 0.5 m, a base-layer of 1.75 m and an active layer of 0.25 m. Additional sensitivity simulations have been performed for an initial thickness of the cohesive sediment fraction. Furthermore, the initial sediment concentration of the cohesive fraction has been decreased and is set to 20 mg/l. The final obtained result will be elaborated for a four consecutive spring - neap tidal cycle, which is set from 15/05/07 - 17/06/07. The results are shown in Figure B.21. The initial sediment thickness of 0.1 m (blue) and 0.2 m (red) show slight difference in SSC. The effect of waves is clearly visualised by the green line representing 0.2 m inclusion of the cohesive sediment, meaning an overall significant increase in SSC due to waves. The tidal current is however still governing the SSC. The final model settings are set in Table B.2.

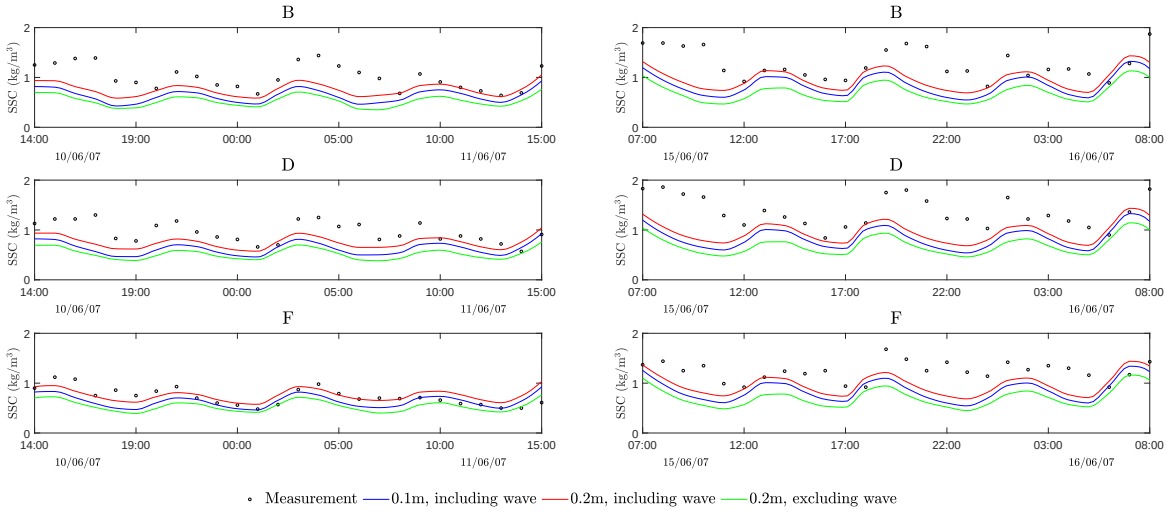

Figure B.21: Final calibration results on the suspended sediment concentration. Comparison initial sediment thickness of 0.1 m and 0.2 m for the cohesive fraction. The green line denotes the value of 0.2 m for tide-only conditions

Final calibration parameter settings	Symbol	Unit	Cohesive	16 μm	90 μm
Erosion parameter	M	($kg/m^2/s$)	$5{\cdot}10^{-4}$	-	-
Critical bed shear stress for erosion	τ_{ce}	(N/m^2)	0.29	-	-
Settling velocity	W_s	(m/s)	10^{-4}	-	-
Boundary conditions (Yangtze influence excluded, see B.3.2)	-	-	20.0	0.5	0.0
Initial concentration	C_0	(mg/l)	20.0	0.0	0.0
Initial bed layer thickness	d_0	(m)	0.2	3.4	3.4

Table B.2: Overview of final calibration parameter settings

C

Island Configuration

This chapter illustrates the spatial mudflat development after ten morphological years for each island configuration. The mudflat is defined as all larger than the mean low water (MLW) at Xiangshui station. The mudflat contour is featured to 0.88 m as discussed in Section 5.1.3. The reference simulation is shown first, wherein the initial- and new resulting mudflat contours are denoted. The following sections show the individual island configurations are considered in which the initial-, new- and reference simulation mudflat contour lines are denoted.

C.1 Reference simulation

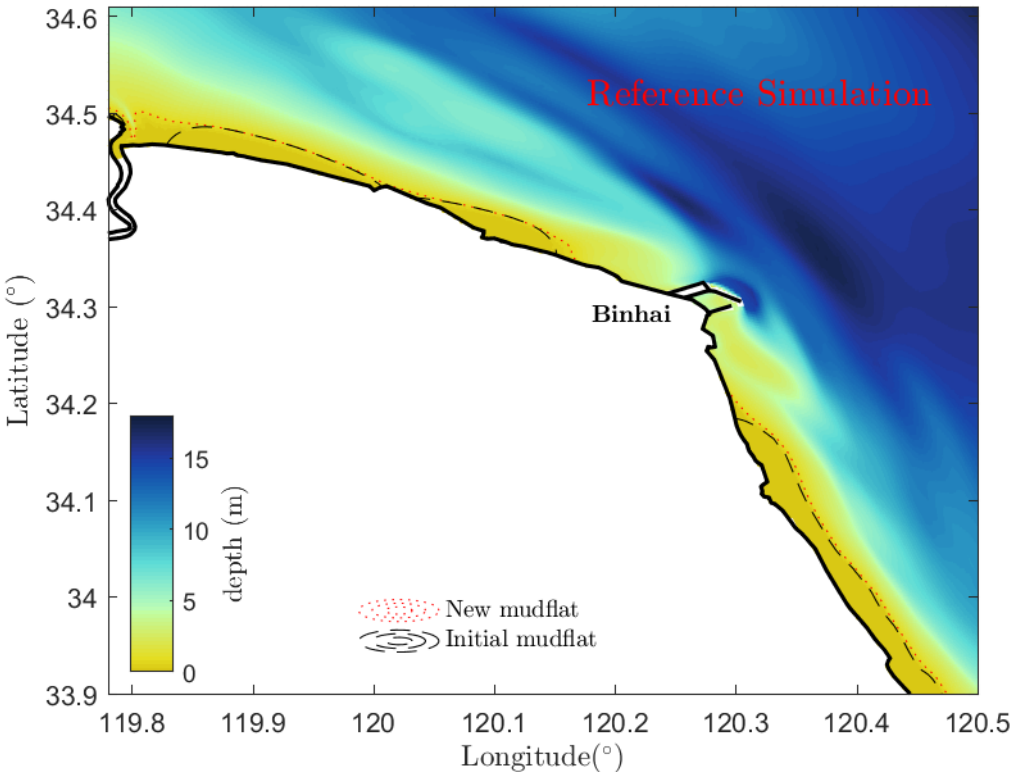

Figure C.1: Reference simulation after ten morphological years: initial- and newly developed mudflat

C.2 Basic Island series

The Basic Island series consist of eight island configurations where several parameters are varying. These parameters are the number of islands, island length, inlet width and distance to shore. Further elaboration on island configuration design can be found in Section 5.2. The parameter settings can be found in Table C.1. The following figures show the modelling result after ten morphological years. The initial- and newly developed mudflat are illustrated. Hence, a comparison can be made with the mudflat development from the reference simulation.

Basic design	Islands (-)	Island length (km)	Island width (km)	Inlet width (km)	Depth contour (m)
N1+S1	3-3	10	0.3	2.5	7-8
N2+S2	3-3	10	0.3	5	7-8
N3+S3	3-3	10	0.3	2.5	4-5
N4+S4	3-3	10	0.3	5	4-5
N5+S5	2-2	15	0.3	2.5	7-8
N6+S6	2-2	15	0.3	5	7-8
N7+S7	2-2	15	0.3	2.5	4-5
N8+S8	2-2	15	0.3	5	4-5

Table C.1: Basic design. Parameter set-up

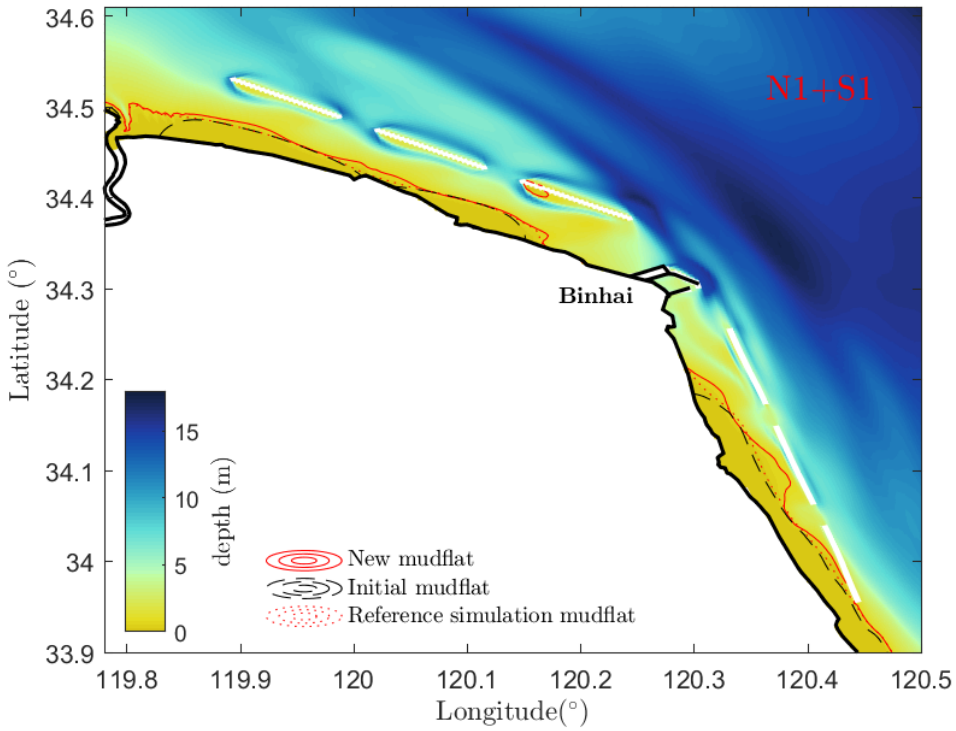

Figure C.2: N1+S1 simulation after ten morphological years: initial- and newly developed mudflat

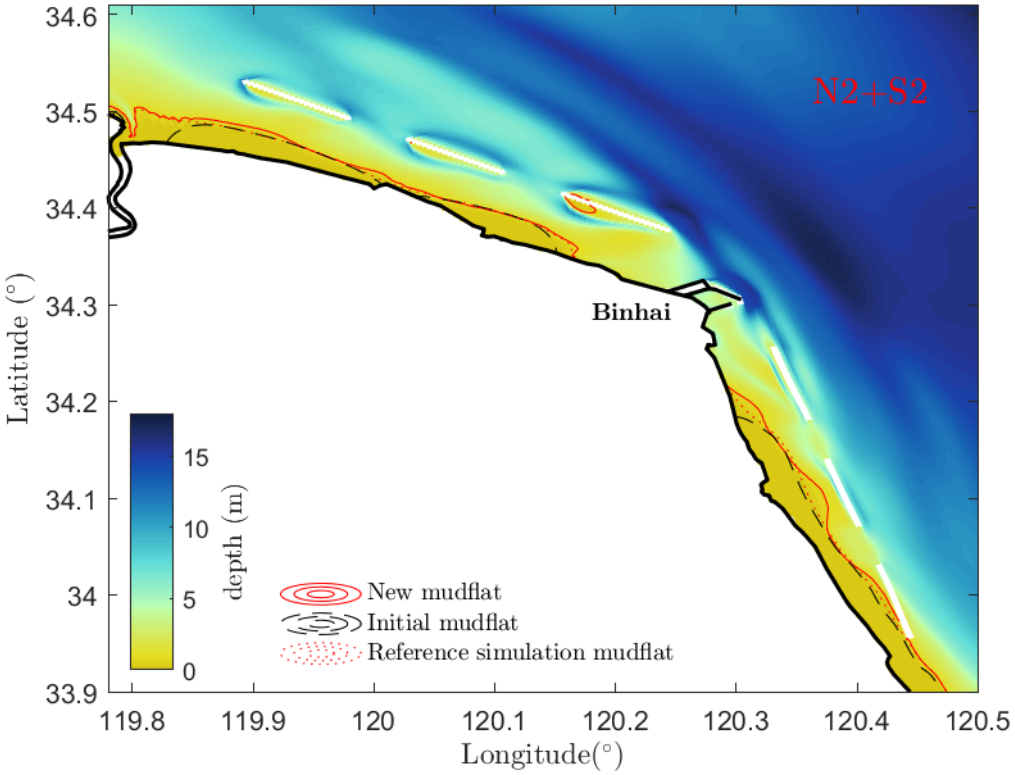

Figure C.3: N2+S2 simulation after ten morphological years: initial- and newly developed mudflat

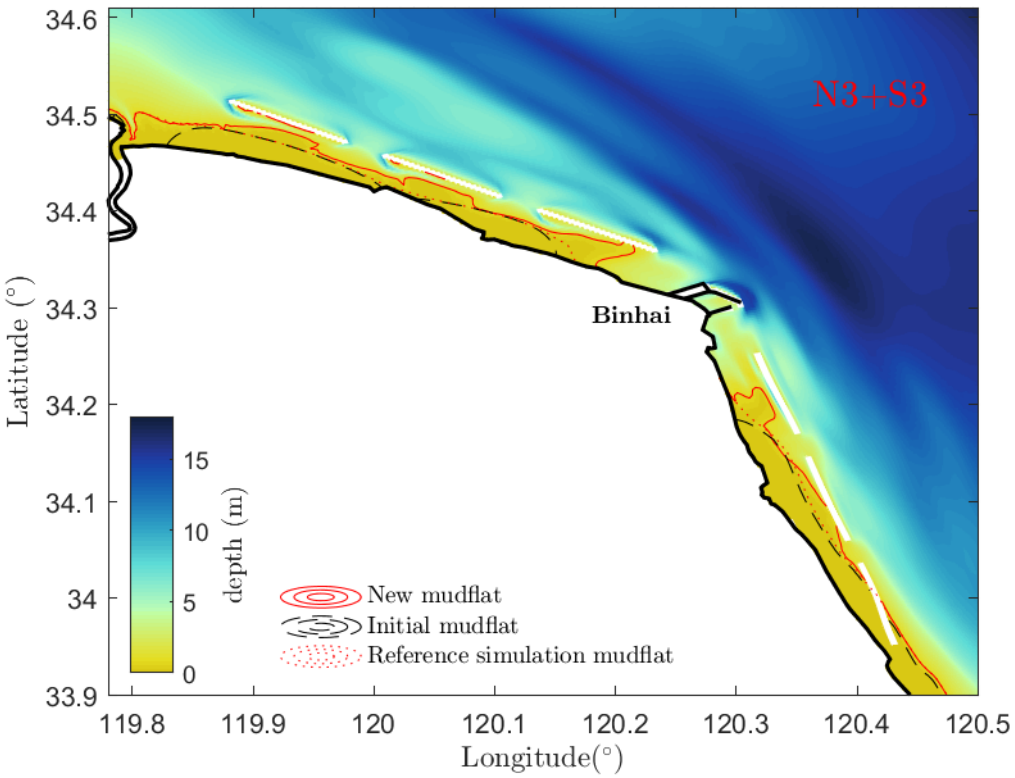

Figure C.4: N3+S3 simulation after ten morphological years: initial- and newly developed mudflat

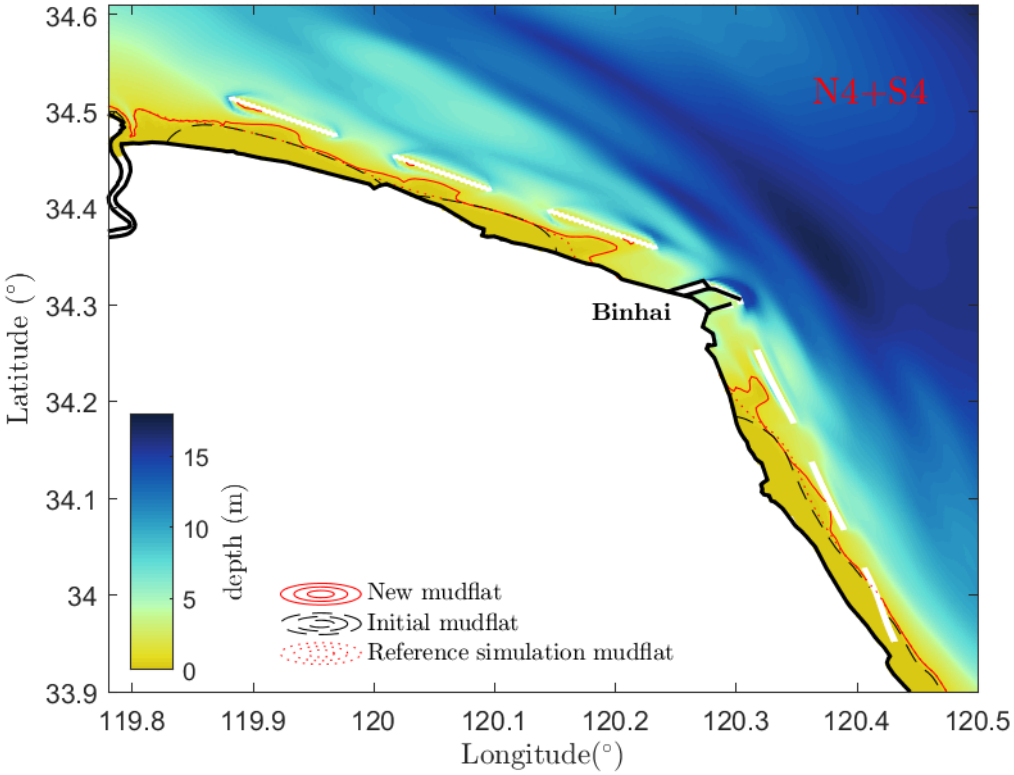

Figure C.5: N4+S4 simulation after ten morphological years: initial- and newly developed mudflat

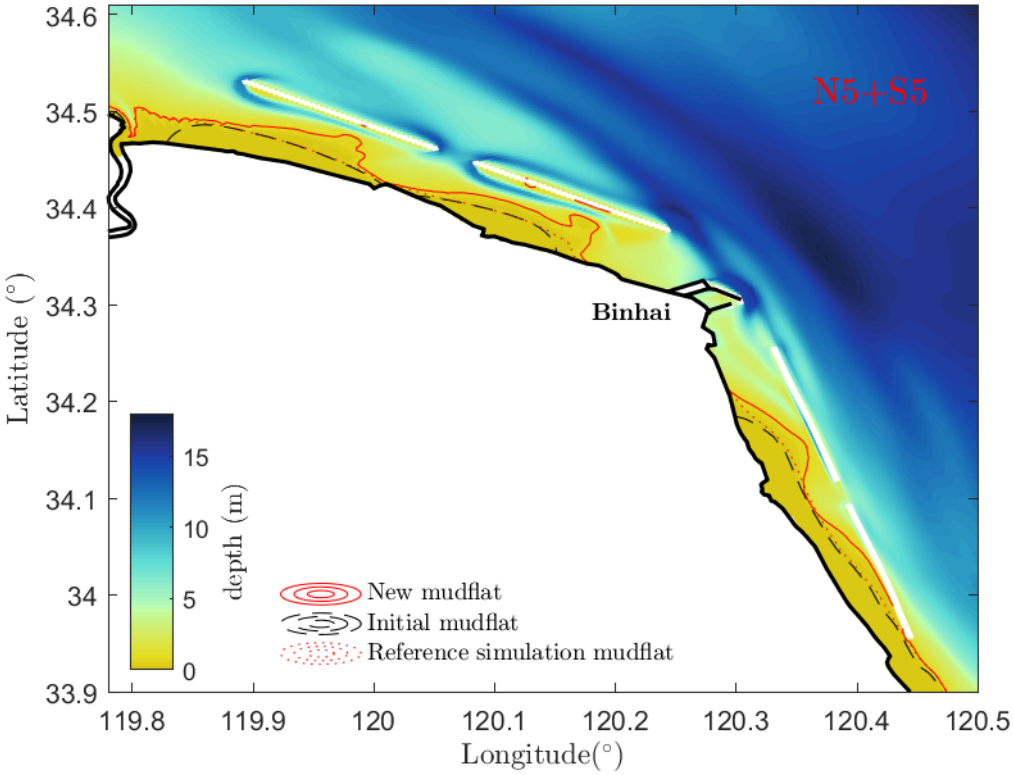

Figure C.6: N5+S5 simulation after ten morphological years: initial- and newly developed mudflat

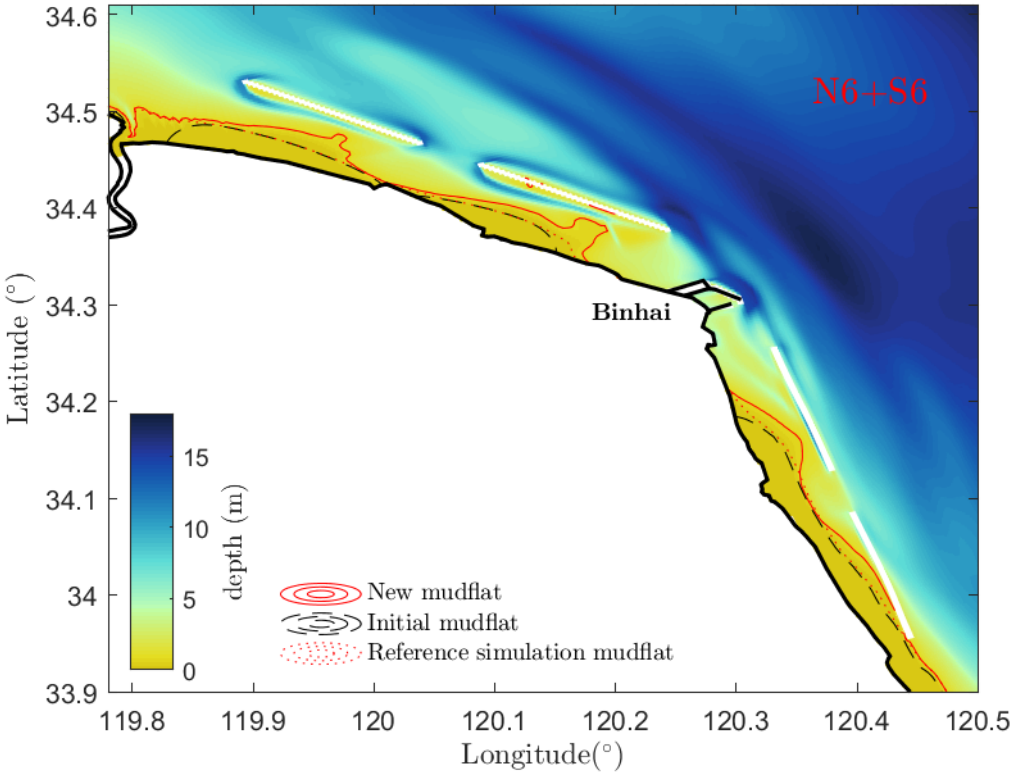

Figure C.7: N6+S6 simulation after ten morphological years: initial- and newly developed mudflat

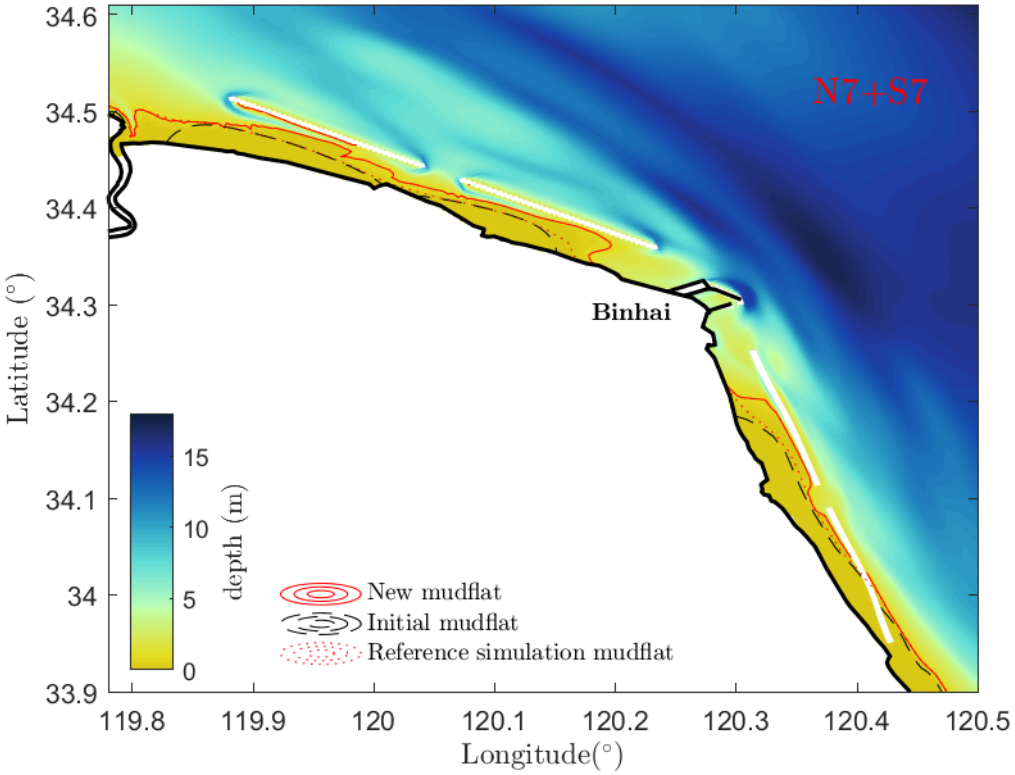

Figure C.8: N7+S7 simulation after ten morphological years: initial- and newly developed mudflat

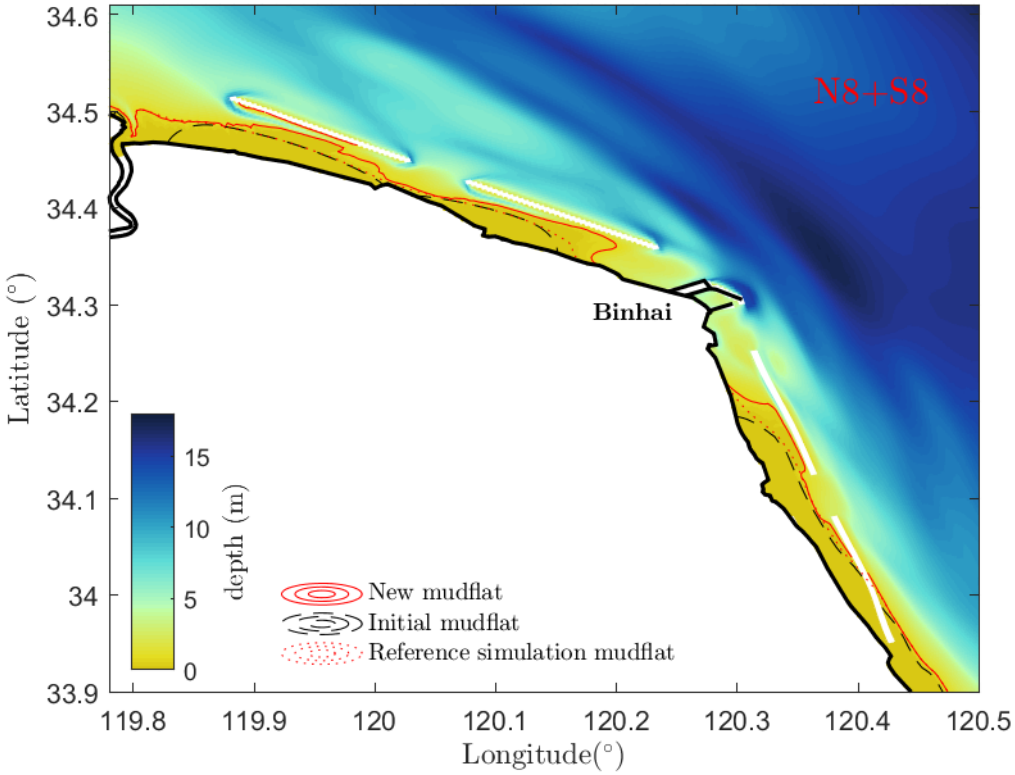

Figure C.9: N8+S8 simulation after ten morphological years: initial- and newly developed mudflat

C.3 Detailed results Basic series

Within this section a quantitative analysis is elaborated on the morphological development differences between the Northern- and Southern Abandoned Yellow River Delta (NAYRD, SAYRD). The island configurations were subjected to a ten year morphological development simulation. Within the Basic series the NAYRD is denoted as 'N', while the SAYRD is denoted as 'S'. The division between the NAYRD and SAYRD is set at Binhai Port. The results of the NAYRD are shown in Table C.2, whereas the results of the SAYRD are shown in Table C.3. From the results it can be seen that the NAYRD shows larger MI-ratio's. The island configurations are equal on both sides of the AYRD. Hence, it can be concluded that the islands on the NAYRD are more effective in mudflat formation. The effect may be due to the smaller bed slope in the NAYRD, for which more sediment can accumulate behind the islands.

Design North	Increase (km^2) relative to reference	Increase (km^2) relative to initial	Total mudflat (km^2)	Islands (km^2)	MI - ratio (-)
Reference	-	27.9000	87.4800	0	0
N1	12.6000	40.5000	127.9800	14.5800	0.8642
N2	7.9200	35.8200	123.3000	12.7800	0.6197
N3	34.2000	62.1000	149.5800	14.5800	2.3457
N4	22.6800	50.5800	138.0600	12.7800	1.7746
N5	38.1600	66.0600	153.5400	16.0200	2.3820
N6	31.6800	59.5800	147.0600	15.0300	2.1078
N7	34.8300	62.7300	150.2100	16.0200	2.1742
N8	30.4200	58.3200	145.8000	15.0300	2.0240

Table C.2: Basic design results after ten morphological years at the Northern Abandoned Yellow River Delta

Design South	Increase (km^2) relative to reference	Increase (km^2) relative to initial	Total mudflat (km^2)	Islands (km^2)	MI - ratio (-)
Reference	-	16.5600	109.9800	0	0
S1	14.2200	30.7800	140.7600	14.5800	0.9753
S2	9.3600	25.9200	135.9000	12.7800	0.7324
S3	14.4000	30.9600	140.9400	14.5800	0.9877
S4	10.1700	26.7300	136.7100	12.7800	0.7958
S5	21.6000	38.1600	148.1400	16.0200	1.3483
S6	18.0900	34.6500	144.6300	15.0300	1.2036
S7	15.4800	32.0400	142.0200	16.0200	0.9663
S8	13.6800	30.2400	140.2200	15.0300	0.9102

Table C.3: Basic design results after ten morphological years at the Southern Abandoned Yellow River Delta

C.4 Exploratory island series

The Exploratory Island series consist of seven island configurations. Further elaboration on island configuration design in Section 5.2. The following figures show the modelling result after ten morphological years. The initial- and newly developed mudflat are illustrated. Hence, a comparison can be made with the mudflat development from the reference simulation.

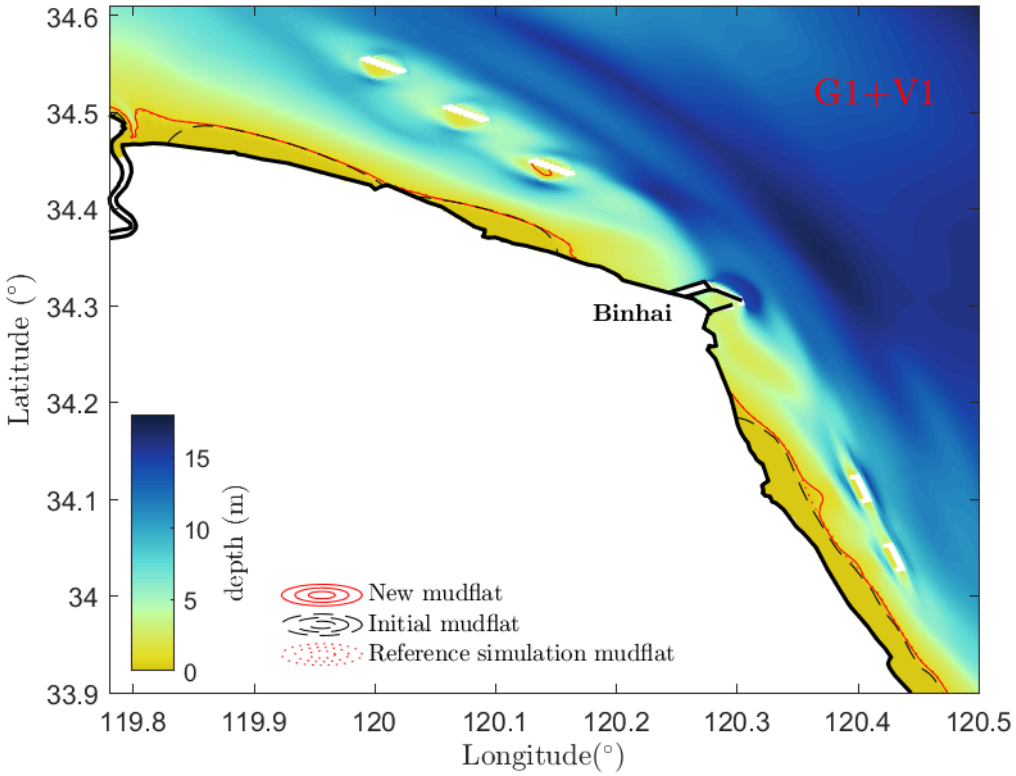

Figure C.10: G1+V1 simulation after ten morphological years: initial- and newly developed mudflat

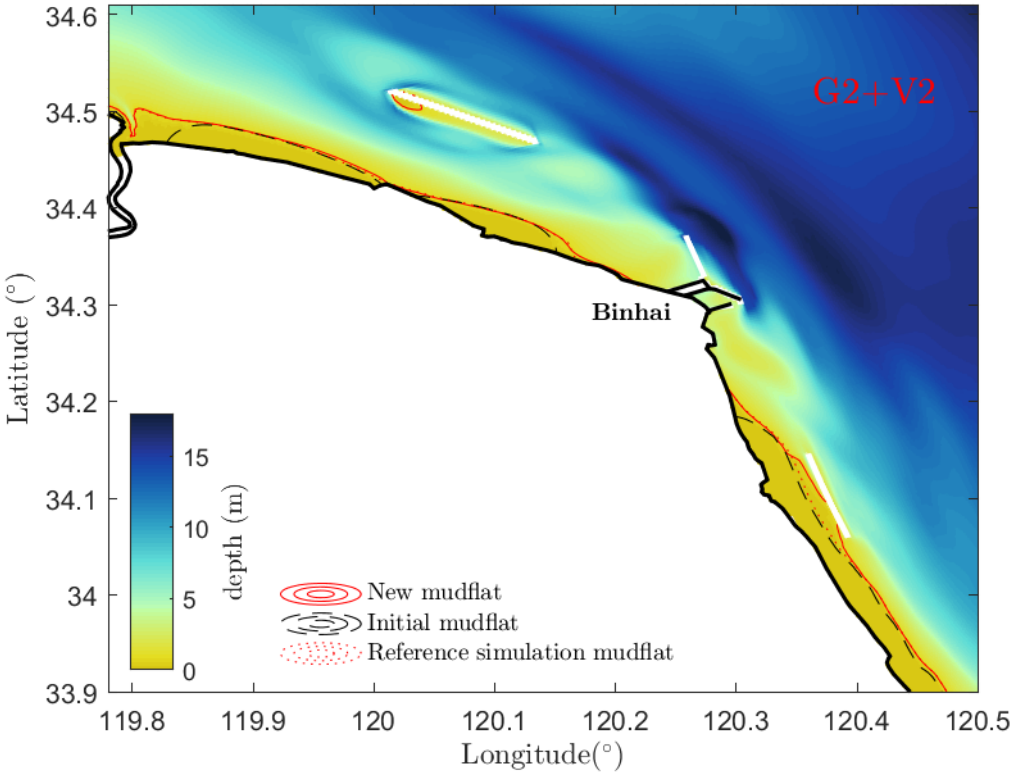

Figure C.11: G2+V2 simulation after ten morphological years: initial- and newly developed mudflat

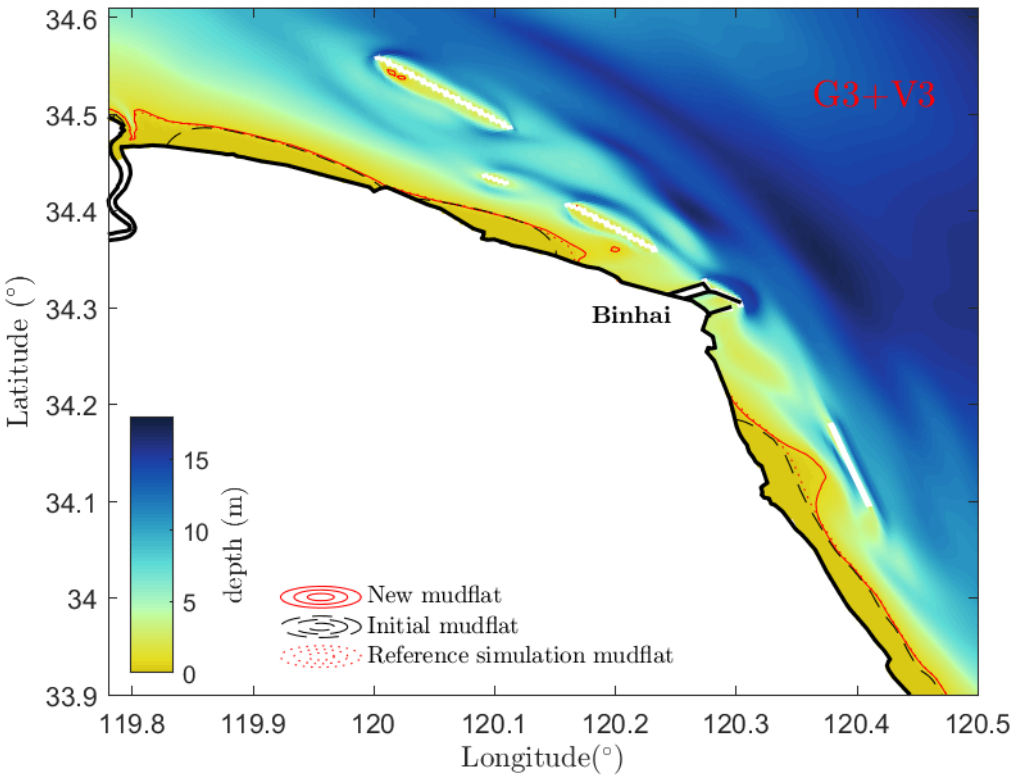

Figure C.12: G3+V3 simulation after ten morphological years: initial- and newly developed mudflat

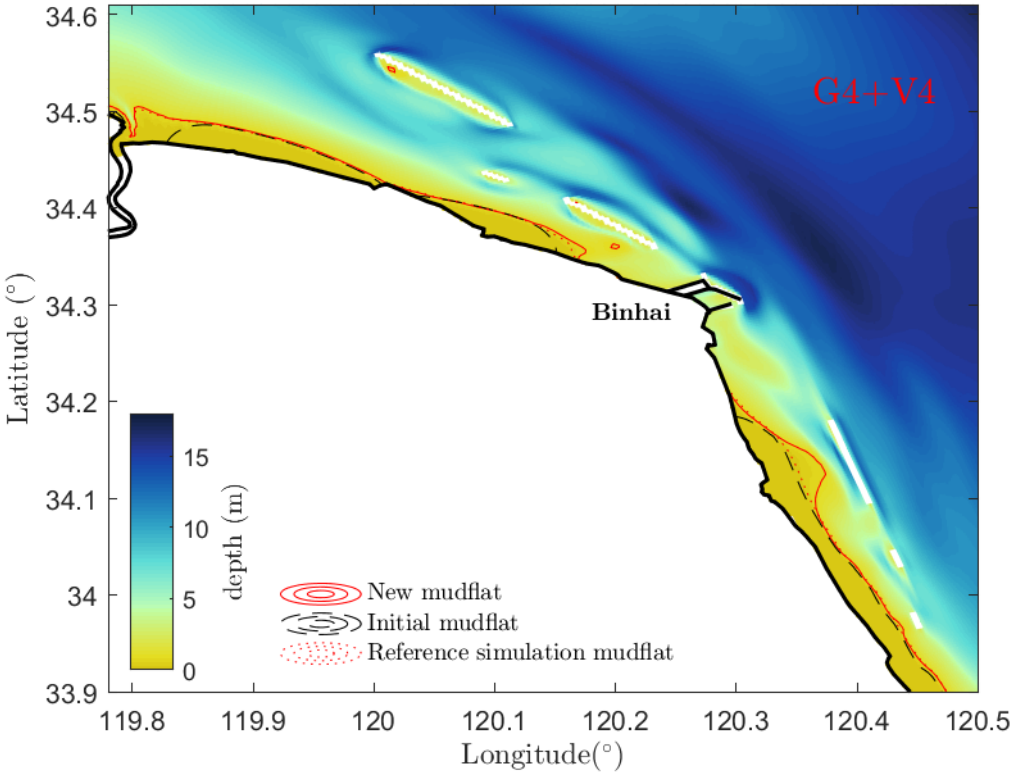

Figure C.13: G4+V4 simulation after ten morphological years: initial- and newly developed mudflat

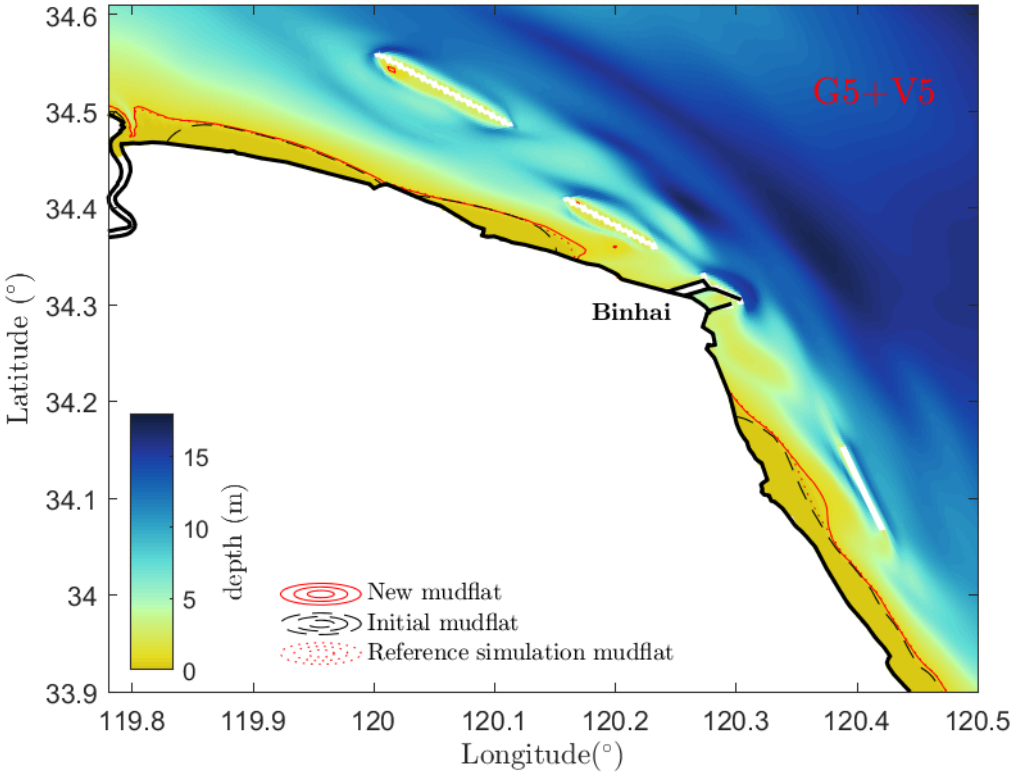

Figure C.14: G5+V5 simulation after ten morphological years: initial- and newly developed mudflat

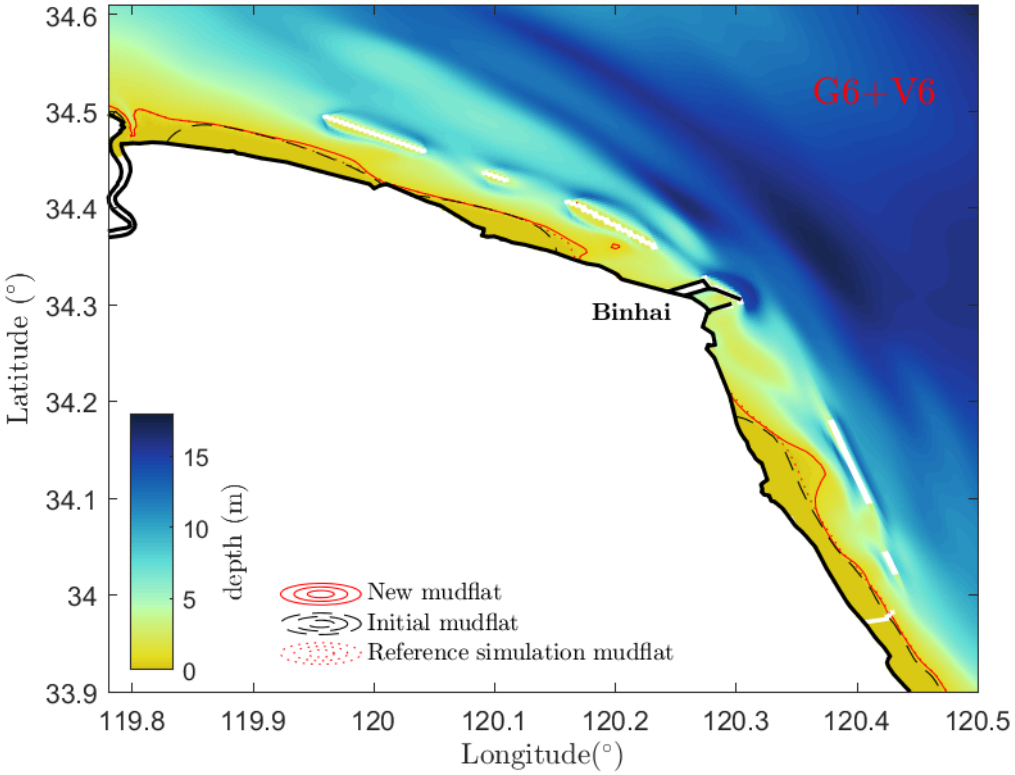

Figure C.15: G6+V6 simulation after ten morphological years: initial- and newly developed mudflat

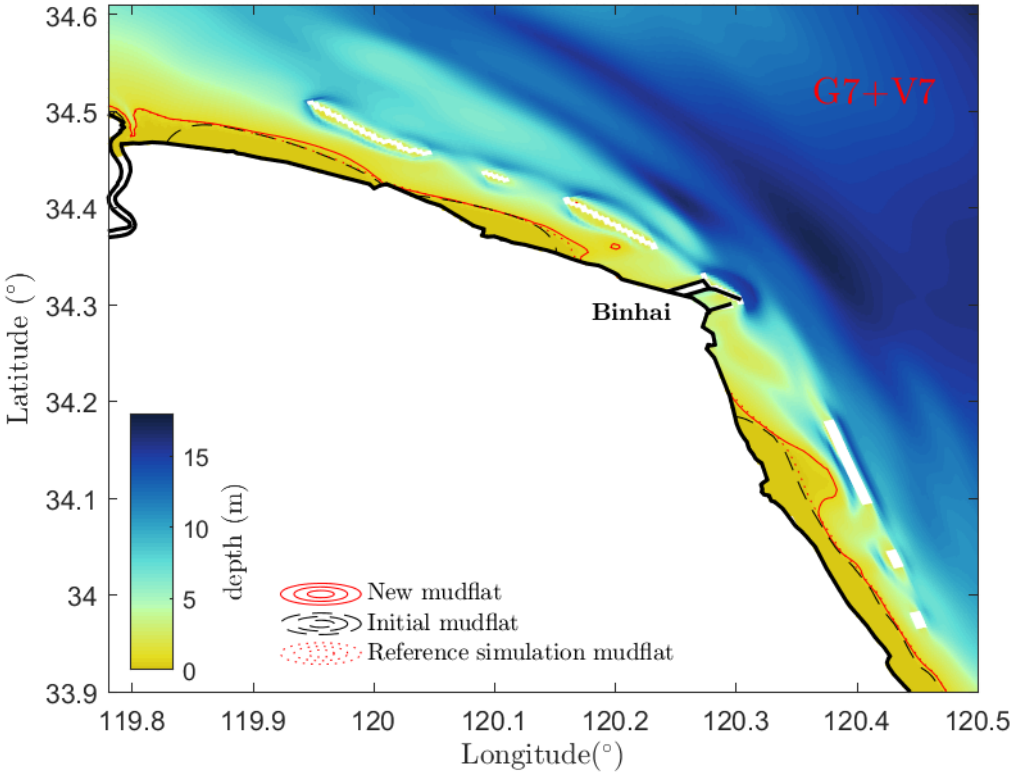

Figure C.16: G7+V7 simulation after ten morphological years: initial- and newly developed mudflat

C.5 Detailed results Exploratory series

Within this section a quantitative analysis is elaborated on the morphological development differences between the Northern- and Southern Abandoned Yellow River Delta (NAYRD, SAYRD). The island configurations were subjected to a ten year morphological development simulation. Within the Exploratory series the NAYRD is denoted as 'G', while the SAYRD is denoted as 'V'. The division between the NAYRD and SAYRD is set at Binhai Port. The results of the NAYRD are shown in Table C.4, whereas the results of the SAYRD are shown in Table C.5.
From the results it can be seen that the SAYRD shows larger MI-ratio's. The island configurations are not equal on both sides of the AYRD. The configuration G7+V7, as depicted as the best of the Exploratory series, has the highest mudflat growth. The V7's MI-ratio is rather small, since the island width was set to 0.6 km. Hence, the MI-ratio can be increased by optimisation iterations.

Design North	Increase (km^2) relative to reference	Increase (km^2) relative to initial	Total mudflat (km^2)	Islands (km^2)	MI - ratio (-)
Reference	-	27.9000	87.4800	0	0
G1	0.2700	28.1700	115.6500	6.4800	0.0417
G2	5.5800	33.4800	120.9600	9.4500	0.5905
G3	3.7800	31.6800	119.1600	8.6400	0.4375
G4	4.1400	32.0400	119.5200	9.9000	0.4182
G5	3.6900	31.5900	119.0700	8.3700	0.4409
G6	5.8500	33.7500	121.2300	8.8200	0.6633
G7	8.2800	36.1800	123.6600	13.3200	0.6216

Table C.4: Exploratory design results after ten morphological years at the Northern Abandoned Yellow River Delta

Design South	Increase (km^2) relative to reference	Increase (km^2) relative to initial	Total mudflat (km^2)	Islands (km^2)	MI - ratio (-)
Reference	-	16.5600	109.9800	0	0
V1	0.5400	17.1000	127.0800	6.4800	0.0833
V2	7.2000	23.7600	133.7400	9.4500	0.7619
V3	6.7500	23.3100	133.2900	8.6400	0.7812
V4	6.3900	22.9500	132.9300	9.9000	0.6455
V5	2.7000	19.2600	129.2400	8.3700	0.3226
V6	6.8400	23.4000	133.3800	8.8200	0.7755
V7	9.7200	26.2800	136.2600	13.3200	0.7297

Table C.5: Exploratory design results after ten morphological years at the Southern Abandoned Yellow River Delta